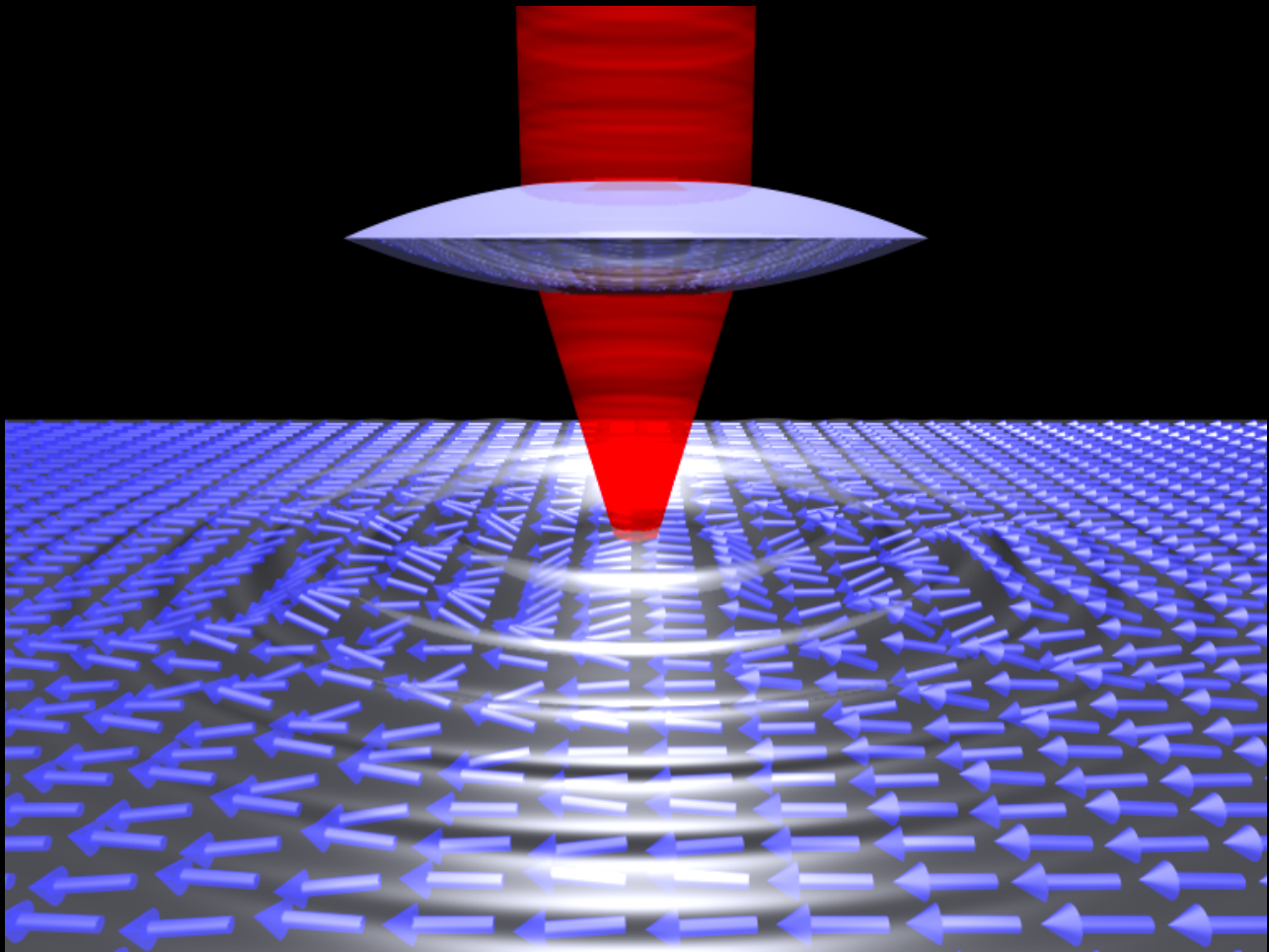


Ultrafast Optical Control of Magnetization in Ferrimagnetic Garnets



Fredrik Hansteen

Printed by PrintPartners Ipskamp, Enschede
ISBN-10: 90-9020626-4
ISBN-13: 978-90-9020626-4
Copyright © 2006, by Fredrik Hansteen
Illustrated with references.
Cover design by Fredrik Hansteen.
A copy of this manuscript can be found at:
<http://www.hansteen.net/thesis.pdf>

Ultrafast Optical Control of Magnetization in Ferrimagnetic Garnets

Een wetenschappelijke proeve op het gebied van
de Natuurwetenschappen, Wiskunde & Informatica

Proefschrift

ter verkrijging van de graad van doctor
aan de Radboud Universiteit Nijmegen
op gezag van de Rector Magnificus prof. dr. C.W.P.M. Blom,
volgens besluit van het College van Decanen
in het openbaar te verdedigen op dinsdag 23 mei 2006
des namiddags om 1.30 uur precies

door

Fredrik Hansteen

geboren op 24 juli 1975
te Bergen, Noorwegen

Promotores : Prof. dr. Th. Rasing
: Prof. dr. O. Hunderi (The Norwegian University
of Science and Technology)

Co-promotores : Dr. A. Kirilyuk
: Dr. A. V. Kimel

Manuscriptcommissie:

Prof. dr. J.-Y. Bigot Institute for Physics and Chemistry of
Materials in Strasbourg (IPCMS),
Louis Pasteur University,
Strasbourg, France.

Prof. dr. S.O. Demokritov Institut für Angewandte Physik,
Westfälische Wilhelms-
Universität Münster,
Münster, Germany.

Prof. dr. W.J. van der Zande Department of Molecular and
Laser Physics,
Radboud University Nijmegen,
Nijmegen, The Netherlands.

The work described in this thesis was financially supported by the Norwegian Research Council and the European RTN Network DYNAMICS.

사랑하는 나의 아내 지혜에게

Preface

This thesis presents the scientific results of my work as a Ph.D. student at The Norwegian University of Science and Technology (NTNU) in Trondheim and at the Institute for Molecules and Materials (IMM), Radboud University in Nijmegen. Although the road leading to the completion of this work has been somewhat long and winding, the final result is in many respects almost exactly what I had hoped for when I decided to embark on this journey.

In the beginning of 2003 when I first came to Nijmegen, I had already been a Ph.D. student at NTNU in Trondheim for about 2 years under the supervision of Johannes Bremer and Ola Hunderi. Using an ellipsometer that I built, I had begun a study of the enhancement of magnetooptical effects by surface plasmons. The plan was to further investigate these effects with time resolved spectroscopy techniques. However, due to the sudden and tragic death of Johannes Bremer, Ola suggested that I go to Theo Rasing's group in Nijmegen to do some experiments and to learn about nonlinear optics and time resolved spectroscopy. The stay was intended to last for about one year, but was later prolonged and eventually made permanent.

During my time in Trondheim and in Nijmegen I truly appreciated all scientific and administrative help, as well as the general support from Johannes Bremer, Ola Hunderi and from Anne Borg who took over as my supervisor. I also appreciate that both Ola and Anne took the time to come and visit me in Nijmegen.

The fact that I started out as a Ph.D. student in Trondheim, but now seem to end up with a degree only from the Radboud University in Nijmegen, is not entirely according plan. However, Norwegian regulations put an effective stop to what could have been a joint degree between the two universities, and left me with the somewhat uncomfortable choice of where to submit my work for a degree. As most of the results presented in this thesis stem from my time in Nijmegen, and represent mainly the interests and expertise of the Nijmegen group, the decision was not too difficult.

Since I came to Nijmegen and the EVSF2 group, I have enjoyed working in labs which are exceptionally well equipped with modern ultrafast laser systems. In addition to the excellent equipment, the group's highly qualified technicians make experimental work a true pleasure. I am especially thankful to Albert van Etteger for sharing with me some of his expertise and long experience with lasers and optics, and to Tonnie Toonen for skillful and rapid assistance with any technical problem. For issues of administrative character I have always been able to rely on the sound advice and assistance of the group's secretaries, Marilou van Breemen and Riki Gommers.

For scientific guidance I have benefited greatly from the supervision of Andrei Kirilyuk, Alexey Kimel, and Theo Rasing. I feel privileged to have been working in the exciting field of ultrafast magnetization dynamics together with this team of scientist. I am particularly grateful to Andrei for his guidance throughout my stay in Nijmegen, for introducing me to nonlinear and time resolved magnetooptics, and

for always being available for discussing ideas, results, problems, and anything else. I am also thankful to Alexey who first introduced me to the field of spin dynamics and taught me how to do pump-probe experiments. This has lead to some of the most exciting and important results of this thesis, and has also given me the most joy. The many discussions with Andrei and Alexey have been stimulating and inspiring. I am grateful to Theo for letting me work in his group and for funding me during the last part of my Ph.D. studies. I also value very highly his encouragements, comments and constructive criticism to my manuscripts and talks.

The magnetic garnet films, which somewhat unexpectedly have become central to this Ph.D. work, were grown at the University of Oslo, in Tom Henning Johansen's group. Lars Egil Helseth, which at that time was a Ph.D. student in Oslo, proposed to collaborate on the characterization of the films, and sent me a series of samples which I gradually have come to appreciate more and more. From the time when I first discovered a huge signal coming from these samples in my pump-probe experiments, they have been known only as "My Precious"¹. Thank you Lars Egil for providing me with these wonderful garnet films!

In Nijmegen, working in a large group of people with different cultural and scientific backgrounds have been both fun and interesting. Daniel and I have had a great time together in the lab doing pump-probe experiments, discussing results and coming up with new ideas. It has also been motivating going to conferences and meetings together with Daniel, Loïc, Jan and Sasha, who are all part of the spin dynamics subgroup. Jan is also to thank for the dutch translation of the summary in the back of this thesis. Peter, with whom I shared an office, and I had fun coming up with several ideas for projects involving gold nano-particles, which have yet to be fully realized. Social events, such as the yearly group uitstapjes, barbecues, and various drink tasting challenges organized by Andrei, were always enjoyable. I have also had much fun playing table tennis with Sergiy, Markus and Jing, and volleyball with Roman, Sergiy and Loïc.

The above mentioned people, as well as many others, both current and previous members of the EVSF2 group, have all contributed to making my stay in Nijmegen a very positive experience.

Finally, I would like to also express my gratitude to my wife Ji Hye for her patience and support during these years.

Fredrik Hansteen
Nijmegen, December 2005.

¹Gollum (Sméagol), in *Lord of the Rings* by J. R. R. Tolkien.

Contents

1	Introduction	1
1.1	Laser heating	2
1.2	Ultrafast demagnetization	3
1.3	Precessional magnetization dynamics	4
1.4	Ultrafast nonthermal control of magnetization	5
1.5	Magnetic dielectric materials	6
1.6	Scope of this thesis	6
	References	7
2	Magnetic Garnets	11
2.1	Introduction	11
2.2	Structural properties	12
2.3	Magnetic properties	13
2.4	Substituted rare-earth iron garnets	14
2.5	Growth	15
2.6	Optical and magneto-optical properties	15
2.7	Garnets studied in this work	16
	References	18
3	Experimental techniques	19
3.1	Ellipsometry	19
3.2	Magnetization-induced Second-Harmonic Generation (MSHG)	28
3.3	The magnetooptical pump-probe technique	32
	References	37

4	Optical and magneto-optical properties of Bi substituted iron garnet films	39
4.1	Introduction	39
4.2	Experimental procedure	40
4.3	Results and discussion	42
4.4	Conclusions	46
	References	46
5	Selective surface/interface characterization of thin garnet films by MSHG	49
5.1	Introduction	50
5.2	Results and discussion	51
5.3	Conclusions	62
	References	62
6	Ultrafast coherent optical control of the magnetization in garnet films	65
6.1	Introduction	66
6.2	Experimental	66
6.3	Results and discussion	69
6.4	Conclusion	92
	References	92
	Summary	95
	Samenvatting	97
	List of Publications	99
	Curriculum Vitae	101

CHAPTER 1

Introduction

Control and switching of magnetization at high speeds is of utmost technological importance. This is most clearly evident in magnetic data storage, however, rapid manipulation of magnetically ordered electron spins is also essential for the evolving technology of spin-electronics, and could form the basis for a future realization of quantum computers. In state of the art magnetic data storage devices, bits are currently being written at GHz rates, implying a switching time of about one nanosecond (10^{-9} s), and thus that an impressive one billion (10^9) magnetic bits can be written per second. Nevertheless, still faster switching is required in order for data storage technology to keep up with the ever increasing amounts of digital information being produced.

The conventional way to switch magnetization is by use of magnetic field pulses generated from electric currents flowing in coils or micro strip-lines. However, when approaching the time scale of a few picoseconds, generation of sufficiently short and strong field pulses becomes extremely difficult. Therefore, in order to achieve spin manipulation on picosecond and eventually sub-picosecond time scales, fundamentally different methods must be found.

Ultrashort laser pulses are currently one of the most promising alternatives to magnetic field pulses for ultrafast control of magnetization. These laser pulses have a typical duration of ten to a hundred femtoseconds ($10^{-14} - 10^{-13}$ s) and represent some of the shortest man made events to date. For this reason they have become an essential tool for the study of ultrafast processes in physics and chemistry. Moreover, the extreme power of the pulses has opened up an entire new regime for laser material

interactions as the peak electric field of a laser pulse can exceed the internal fields of an atom. The challenge in magnetism is to find fast and efficient mechanisms for control of magnetically ordered spins by such ultrashort pulses of light. The technological importance, as well as the many scientifically interesting aspects of this problem have stimulated intense research in the field of ultrafast magnetization dynamics.

1.1 Laser heating

It is well known that the magnetization of a ferromagnetic material decreases when it is heated. At temperatures above the Curie point, all long-range magnetic ordering is lost and the macroscopic magnetization vanishes completely. Absorption of intense laser radiation can cause temperature increase and thus lead to partial or complete demagnetization of a material. The fundamental processes leading to this demagnetization can be analyzed by conceptually separating the material into an electron, spin and lattice system, with corresponding temperatures T_e , T_s , and T_l [1], as is schematically depicted in Figure 1.1. In this model the magnetization $M(T_s)$ is governed by

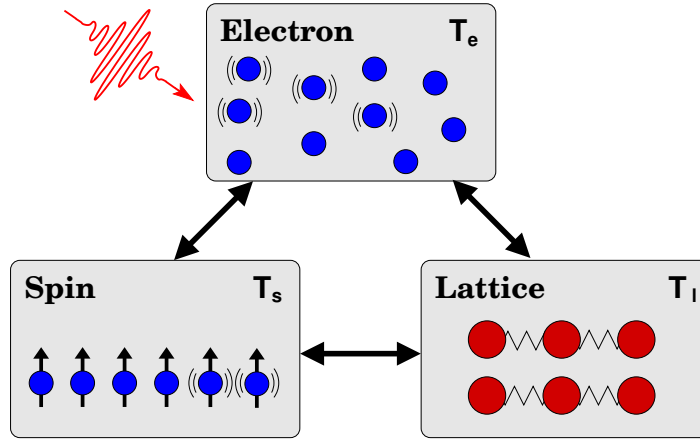


Figure 1.1: Schematic illustration of the interaction between the electron, lattice and spin system following laser excitation.

the spin temperature T_s . The interaction of the material with the electric field of a laser pulse proceeds mainly via the electrons, and since optical transitions (mostly) preserve the spin, only the electron system is initially excited. In metallic systems the highly photoexcited electrons thermalize within a few hundred femtoseconds to a hot Fermi-Dirac distribution that can reach electron temperatures of a 1000K or

more. Subsequent interactions between the electron, lattice and spin system leads to a rise in the lattice- and spin temperatures until thermal equilibrium is reached. The time scale of the electron-lattice interaction is typically about 1 ps, while the characteristic time of the spin-lattice interaction is a few picoseconds in metals, and of the order of a few nanoseconds in dielectric materials. Up to 1996, the spin-lattice interaction was commonly believed to be the dominant channel through which the spin temperature T_s could be affected, while the electron-spin channel was considered less important. However, recent studies of laser-induced magnetization dynamics in ferromagnetic metals have revealed surprisingly rapid demagnetization, much faster than the spin-lattice relaxation time.

1.2 Ultrafast demagnetization

The first ultrafast time resolved studies of the impact of laser pulses on the magnetization were done on Ni and Fe using picosecond laser pulses, but these were not successful in observing any magnetic effects up to the melting point of the samples [2, 3]. Later, using time-resolved spin-polarized photoemission as a probe of the magnetization, Vaterlaus *et al.* succeeded in estimating the spin-lattice relaxation time in Gd films to be 100 ± 80 ps [4]. In 1996 Beaurepaire *et al.* reported the first observation of subpicosecond demagnetization in Ni induced by 60fs laser pulses [1], using time resolved measurements of the Magneto-optical Kerr Effect (MOKE) as a probe of the magnetization. This ultrafast magnetic response was explained by an effective electron-spin interaction mechanism among the strongly nonequilibrium photoexcited electrons, leading to a rapid increase of the spin temperature and destruction of the magnetization. The observation triggered the interest of several groups and similar experiments confirmed the ultrafast demagnetization in Ni, Co, and other metallic systems [5, 6, 7, 8]. It was concluded that the magnetization follows the electron temperature with a delay between the electron excitation and the magnetic breakdown of no more than 50fs. An experimental artifact was revealed by Regensburger *et al.* [9] and Koopmans *et al.* [10] who pointed out that the magneto-optical response does not always directly relate to the magnetization during the first few hundred femtoseconds as a result of hot electron effects. The speed of the true demagnetization was consequently reduced to 0.5-1ps and ascribed to an effective spin-lattice interaction. The significant role of artifacts in time-resolved magneto-optical experiments was also demonstrated in *ab-initio* calculations [11]. Recently, however, it was shown that laser-induced spin dynamics indeed does take place during the initial electron thermalization with a characteristic time of about 50fs [12, 13, 14], thus again raising the question of the underlying mechanism. The complete interpretation of this rapid demagnetization is still not clear, partly because it is difficult to distinguish between different processes in metallic systems due to their complex electronic structure and the continuum of transitions [11, 15, 16].

In addition to laser-induced demagnetization the triggering of spin waves by laser pulses have been studied [17, 18, 19, 20, 21, 22]. In these experiments the equilibrium orientation for the magnetization is believed to be changed through thermal modulation of the magnetic anisotropy, thus causing the magnetization to precess.

1.3 Precessional magnetization dynamics

The equilibrium direction for the magnetization vector \mathbf{M} of a uniformly magnetized sample is along the effective magnetic field

$$\mathbf{H}_{\text{eff}} = \mathbf{H}_{\text{ext}} + \mathbf{H}_{\text{anis}} + \mathbf{H}_{\text{dem}}, \quad (1.1)$$

defined as the vectorial sum of all magnetic fields acting on the sample, i.e. externally applied field \mathbf{H}_{ext} , internal anisotropy field \mathbf{H}_{anis} , and demagnetizing field \mathbf{H}_{dem} . If this equilibrium direction is changed on a time scale much shorter than the response time of the system, for instance by laser excitation of the material, \mathbf{M} will start to precess around the new effective field \mathbf{H}'_{eff} as illustrated in Figure 1.2. Damping

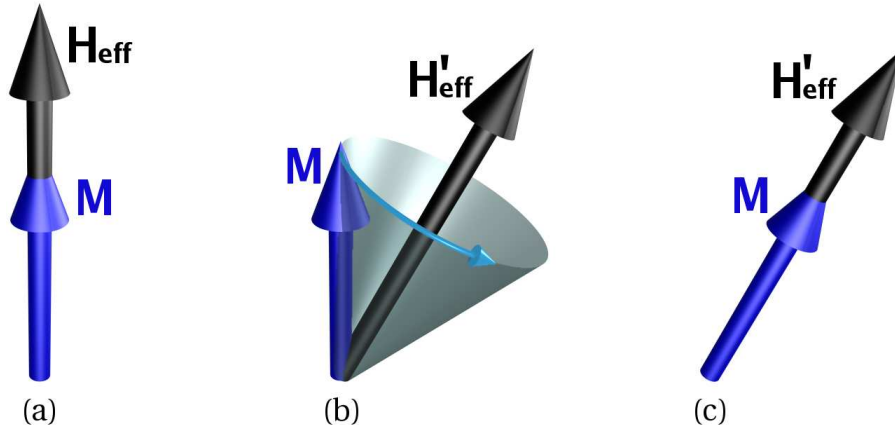


Figure 1.2: An illustration of precessional magnetization dynamics. (a) The initial state with \mathbf{M} oriented along the equilibrium direction \mathbf{H}_{eff} . (b) A sudden change in the direction of the effective magnetic field $\mathbf{H}_{\text{eff}} \rightarrow \mathbf{H}'_{\text{eff}}$ causes the magnetization to precess around \mathbf{H}'_{eff} . (c) Due to damping \mathbf{M} spirals towards \mathbf{H}'_{eff} and eventually comes to rest in this new equilibrium state.

processes cause \mathbf{M} to follow a spiral path towards the new equilibrium state \mathbf{H}'_{eff} . This precessional dynamics can be described by the Landau-Lifshitz equation of motion

[23, 24]

$$\frac{d\mathbf{M}}{dt} = -\gamma(\mathbf{M} \times \mathbf{H}_{\text{eff}}) - \frac{\alpha}{|\mathbf{M}|} \left(\mathbf{M} \times \frac{d\mathbf{M}}{dt} \right), \quad (1.2)$$

where γ is the gyromagnetic ratio, and α is the phenomenological Gilbert damping parameter.

This type of coherent precession is the fastest known way to alter the direction of the macroscopic magnetization of a material. Manipulation of \mathbf{M} on ultrashort time scales should therefore be done through careful control of the precessional magnetization dynamics. This requires means to start a precession, precisely stop it, and to keep the magnetization stable along the desired direction. As will be shown in this Thesis, nonthermal photomagnetic effects in garnets allow for such control of the precessional dynamics by femtosecond laser pulses.

1.4 Ultrafast nonthermal control of magnetization

For all of the above-mentioned previous experimental studies of laser-induced magnetization dynamics in metals, the observed magnetic excitation was the result of optical absorption followed by a rapid temperature increase in the electron system. Far more exciting is the possibility of ultrafast *nonthermal* control of magnetization by light, where a change in the magnetization is not simply the result of a temperature increase.

Such nonthermal control of spins by light provides potentially much greater freedom for the manipulation of \mathbf{M} , and unwanted heating and possible material damage in devices can be avoided. Nonthermal influence of light on magnetization in metals has been predicted by theory [25], but many aspects of this are still subject to debate [11]. A few experimental attempts to observe a nonthermal influence of light on metallic magnetic systems have been reported [21, 26]. However, no impact on the magnetization could be seen in the time after the optical pulse. This is partly due to the dominating thermal effect in metals, and to the unfortunate coincidence of several processes in the same narrow time window which hampers the analysis [27, 28].

Novel ferromagnetic semiconducting alloys, such as (Ga, Mn)As, have recently attracted much attention [29, 30]. In this type of materials the ferromagnetism is mediated by the free carriers, and highly effective nonthermal control of the magnetization by light was reported in static measurements [31]. However, these large values of the photoinduced magnetization have not been reproduced or confirmed by dynamic measurements with subpicosecond time resolution [32, 33], and similar experiments have only shown thermal effects of light on the magnetic system [34, 35]. A number of difficulties are associated with this relatively new class of materials, and the understanding of their electronic, optical, and magnetic properties is currently very limited and controversial.

1.5 Magnetic dielectric materials

When seeking to improve our understanding of ultrafast spin dynamics and searching for nonthermal photomagnetic effects, dielectrics possess some significant advantages over metals and semiconductors. The phonon-magnon interaction responsible for thermal effects is much slower in dielectrics than in metals and therefore does not obscure the interpretation of processes on shorter time scales [36]. Moreover, the electron-spin scattering mechanism proposed in metals cannot exist in dielectrics due to the localized nature of their electronic states. And finally, magnetic dielectrics, in contrast to the novel magnetic semiconductors, are characterized by a well-defined electronic structure and their optical and magnetic properties are well understood.

For about 50 years magnetic garnets have been one of the most popular types of magnetic dielectric materials for both research and applications [37, 38]. Their physical properties are well known and can be tailored over a wide range through chemical substitution and by varying their growth conditions. For decades they have been considered ideal model systems for the experimental and theoretical investigation of magnetic phenomena. Their optical absorption in the infrared spectral region is very low and they exhibit large magneto-optical effects caused by strong spin-orbit coupling. The linewidth of ferrimagnetic resonance in garnets can be extremely narrow, implying a very low damping of magnetic excitations [37]. Additionally, static control of the magnetic anisotropy by light has been known for some time in this class of materials. For these reasons they seem to be ideal materials for the study of ultrafast spin dynamics in general and for the search for nonthermal mechanisms for optical control of magnetization in particular [39].

1.6 Scope of this thesis

This thesis deals with experimental studies of ultrafast laser-induced magnetization dynamics in ferrimagnetic garnet films. The main focus is on novel mechanisms for ultrafast and nonthermal optical spin manipulation in this material. In addition, important background studies of the magnetic, optical and magneto-optical properties of these garnet films are presented.

Chapter 2 gives a general introduction to the magnetic garnets which have been an extremely important class of materials for the study of magnetism and magnetic phenomena during the past 50 years. In Chapter 3 the three main experimental techniques used in this work are described. This includes ellipsometry which was used for characterization of the linear optical and magneto-optical properties of the garnets, magnetization-induced second-harmonic generation (MSHG) which was used to specifically investigate the garnet film surface and interface, and the all-optical pump-and-probe technique employed for the study of laser-induced magnetization dynamics.

The subsequent three chapters present results from studies of magnetic garnet films using the above mentioned techniques. Specifically, Chapter 4 presents the spectral dependence of the diagonal and off-diagonal elements of the dielectric permittivity tensor, obtained from ellipsometry measurements. Magnetic and structural properties of the film surface and interface investigated using the MSHG technique are discussed in Chapter 5. In Chapter 6 the results from time-resolved studies of the laser-induced magnetization dynamics in garnet films are presented, and it is demonstrated that the existence of ultrafast and nonthermal photomagnetic effects allows for coherent optical control of the magnetization on a femtosecond time scale.

References

- [1] E. Beaurepaire, J.-C. Merle, A. Daunois, and J.-Y. Bigot, *Phys. Rev. Lett.* **76**, 4250 (1996).
- [2] M. B. Agranat, S. I. Ashitkov, A. B. Granovskii, and G. I. Rukman, *Zh. Eksp. Teor. Fiz.* **86**, 1376 (1984), [*JETP* **59**, 804 (1984)].
- [3] A. Vaterlaus, T. Beutler, and F. Meier, *J. Appl. Phys.* **67**, 5661 (1990).
- [4] A. Vaterlaus, T. Beutler, and F. Meier, *Phys. Rev. Lett.* **67**, 3314 (1991).
- [5] A. Scholl, L. Baumgarten, R. Jacquemin, and W. Eberhardt, *Phys. Rev. Lett.* **79**, 5146 (1997).
- [6] J. Hohlfeld, E. Matthias, R. Knorren, and K. H. Bennemann, *Phys. Rev. Lett.* **78**, 4861 (1997).
- [7] J. Gdde, U. Conrad, V. Jhnke, J. Hohlfeld, and E. Matthias, *Phys. Rev. B* **59**, R6608 (1999).
- [8] E. Beaurepaire, M. Maret, V. Halt, J.-C. Merle, A. Daunois, and J.-Y. Bigot, *Phys. Rev. B* **58**, 12134 (1998).
- [9] H. Regensburger, R. Vollmer, and J. Kirschner, *Phys. Rev. B* **61**, 14716 (2000).
- [10] B. Koopmans, M. van Kampen, J. T. Kohlhepp, and W. J. M. de Jonge, *Phys. Rev. Lett.* **85**, 844 (2000).
- [11] P. M. Oppeneer and A. Liebsch, *J. Phys.: Condens. Matter* **16**, 5519 (2004).
- [12] L. Guidoni, E. Beaurepaire, and J.-Y. Bigot, *Phys. Rev. Lett.* **89**, 017401 (2002).
- [13] E. Beaurepaire, G. M. Turner, S. M. Harrel, M. C. Beard, J. Y. Bigot, and C. A. Schmuttenmaer, *Appl. Phys. Lett.* **84**, 3465 (2004).

-
- [14] J.-Y. Bigot, L. Guidoni, E. Beaurepaire, and P. N. Saeta, Phys. Rev. Lett. **93**, 077401 (2004).
 - [15] W. Hübner and G. P. Zhang, Phys. Rev. B **58**, R5920 (1998).
 - [16] A. Vernes and P. Weinberger, Phys. Rev. B **71**, 165108 (2005).
 - [17] G. Ju, A. V. Nurmikko, R. F. C. Farrow, R. F. Marks, M. J. Carey, and B. A. Gurney, Phys. Rev. Lett. **82**, 3705 (1999).
 - [18] G. Ju, L. Chen, A. V. Nurmikko, R. F. C. Farrow, R. F. Marks, M. J. Carey, and B. A. Gurney, Phys. Rev. B **62**, 1171 (2000).
 - [19] M. van Kampen, C. Jozsa, J. T. Kohlhepp, P. LeClair, L. Lagae, W. J. M. de Jonge, and B. Koopmans, Phys. Rev. Lett. **88**, 227201 (2002).
 - [20] Q. Zhang, A. V. Nurmikko, A. Anguelouch, G. Xiao, and A. Gupta, Phys. Rev. Lett. **89**, 177402 (2002).
 - [21] R. Wilks, R. J. Kicken, M. Ali, B. J. Hickey, J. D. R. Buchanan, A. T. G. Pym, and B. K. Tanner, J. Appl. Phys. **95**, 7441 (2004).
 - [22] M. Vomir, L. H. F. Andrade, L. Guidoni, E. Beaurepaire, and J.-Y. Bigot, Phys. Rev. Lett. **94**, 237601 (2005).
 - [23] L. Landau and E. Lifshitz, Phys. Z. Union. **8**, 153 (1935).
 - [24] B. Hillebrands and K. Ounadjela, eds., *Spin dynamics in confined magnetic structures I*, Topics in applied physics (Springer, Berlin, 2002).
 - [25] G. P. Zhang and W. Hübner, Phys. Rev. Lett. **85**, 3025 (2000).
 - [26] G. Ju, A. Vertikov, A. V. Nurmikko, C. Canady, G. Xiao, R. F. C. Farrow, and A. Cebollada, Phys. Rev. B **57**, R700 (1998).
 - [27] J.-Y. Bigot, C. R. Acad. Sci. Ser. IV (Paris) **2**, 1483 (2001).
 - [28] Recently we have managed to suppress this dominating thermal effect in GdFeCo and to observe true non-thermal effects. (in preparation).
 - [29] H. Ohno, Science **281**, 951 (1998).
 - [30] H. Ohno, A. Shen, F. Matsukura, A. Oiwa, A. Endo, S. Katsumoto, and Y. Iye, Appl. Phys. Lett. **69**, 363 (1996).
 - [31] A. Oiwa, Y. Mitsumori, R. Moriya, T. Slupinski, and H. Munekata, Phys. Rev. Lett. **88**, 137202 (2002).

- [32] Y. Mitsumori, A. Oiwa, T. Slupinski, H. Maruki, Y. Kashimura, F. Minami, and H. Mune-kata, Phys. Rev. B **69**, 033203 (2004).
- [33] A. V. Kimel, G. V. Astakhov, G. M. Schott, A. Kirilyuk, D. R. Yakovlev, G. Karczewski, W. Ossau, G. Schmidt, L. W. Molenkamp, and Th. Rasing, Phys. Rev. Lett. **92**, 237203 (2004).
- [34] E. Kojima, R. Shimano, Y. Hashimoto, S. Katsumoto, Y. Iye, and M. Kuwata-Gonokami, Phys. Rev. B **68**, 193203 (2003).
- [35] J. Wang, C. Sun, J. Kono, A. Oiwa, H. Mune-kata, L. Cywiński, and L. J. Sham, Phys. Rev. Lett. **95**, 167401 (2005).
- [36] A. V. Kimel, R. V. Pisarev, J. Hohlfeld, and Th. Rasing, Phys. Rev. Lett. **89**, 287401 (2002).
- [37] G. Winkler, *Magnetic Garnets* (Friedr. Vieweg & Sohn, Braunschweig, Germany, 1981).
- [38] A. Paoletti, ed., *Physics of Magnetic Garnets*, Enrico Fermi International School of Physics, Italian Physical Society (North-Holland Publishing Co., 1978), ISBN 0-444-85200-x.
- [39] A. F. Kabychenkov, Zh. Eksp. Teor. Fiz. **100**, 1219 (1991), [JETP **73**, 672 (1991)].

CHAPTER 2

Magnetic Garnets

2.1 Introduction

Garnets belong to a class of minerals with a characteristic crystal structure but with a great diversity in chemical composition. The name is derived from the Latin word "granum" meaning grain, and refers to the typically rounded shape of garnets found in nature. They are well known as beautiful gem stones that exist in various colors depending on the composition. Most famous of these is the deep red pyrope with chemical formula $\text{Mg}_3\text{Al}_2\text{Si}_3\text{O}_{12}$, which in the early middle ages was believed to be a source of magic power and wisdom [1].

In the 1950s a fascinating new class of synthetically made garnets with magnetic properties was discovered. These garnets with ferrimagnetic ordering were found to have a number of interesting properties and to exhibit a wide range of magnetic phenomena. This has caused them to be studied intensively over the past decades [1, 2]. Since their discovery, they have contributed significantly to the present understanding of many aspects of magnetism, and have served as ideal model systems for both experimental and theoretical studies of magnetic phenomena.

Being dielectric transparent magnetic materials with a particularly strong magneto-optical response, the magnetic garnets have found widespread application in optical components such as modulators and isolators, as magnetic field sensors and indicators, and in microwave technology. They were also popular materials for magnetic bubble-domain memories, a technology that was very promising in the 1970s but could not compete commercially with the hard disks developed in the 1980s.

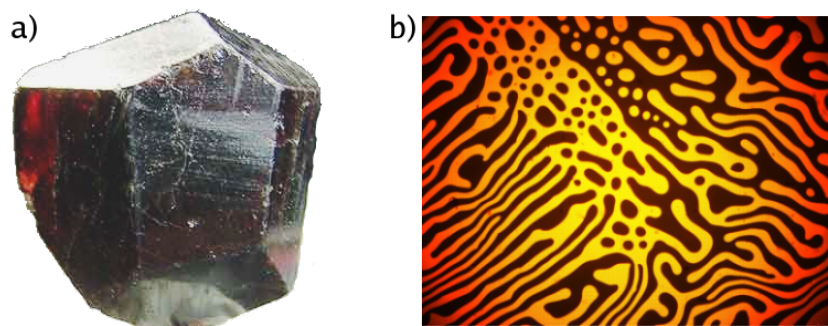


Figure 2.1: (a) Natural garnet crystal. (b) Magnetic domains in a out-of-plane magnetized thin garnet film as seen in a polarizing microscope.

The fascination with garnets, and their extreme usefulness lie in the great diversity of magnetic phenomena that they exhibit. This can be ascribed to their particular crystal structure which allows for a wide range of chemical substitutions, and thus provides great flexibility for tuning of the magnetic properties. The technology for growth of garnets was early taken to such a level of perfection that garnet crystals could be grown with lower acoustic damping than quartz. Also, partly due to the quality with which these crystals can be grown, yttrium iron garnet (YIG), usually considered the prototype magnetic garnet, is the magnetic material with the narrowest known line width of ferromagnetic resonance and the lowest spin-wave damping.

2.2 Structural properties

The magnetic properties of the garnets are a direct consequence of the structure and the particular ions in the crystal. While other magnetic garnets exist, in the following mainly the rare earth iron garnets $R_3Fe_5O_{12}$ will be discussed, where R can be any of the rare earth metals from yttrium to lutetium. Yttrium iron garnet (R=Y) (YIG) will here be considered as the prototype magnetic garnet compound, from which others are derived by chemical substitution.

The chemical composition of YIG is $\{Y_3\}[Fe_2](Fe_3)O_{12}$ and its crystal structure is cubic. In the chemical formula the different brackets are used to indicate the three different coordinations of the cations with respect to oxygen in the crystal. The large yttrium Y^{3+} ions are located in the dodecahedral positions (denoted $\{ \}$) where they are surrounded by the eight O^{2-} ions that form the corners of a dodecahedron. The Fe^{3+} ions with smaller ionic radii are located in octahedral sites (denoted $[]$) with six nearest oxygen ions as neighbors forming an octahedron. Trivalent iron ions are also

found in tetrahedral sites (denoted (t)), surrounded by four oxygen ions which occupy the corners of a stretched cube. In a unit cell there are 24 of the large dodecahedral sites, 16 of the octahedral sites, and 24 of the smallest sites with tetrahedral point group symmetry.

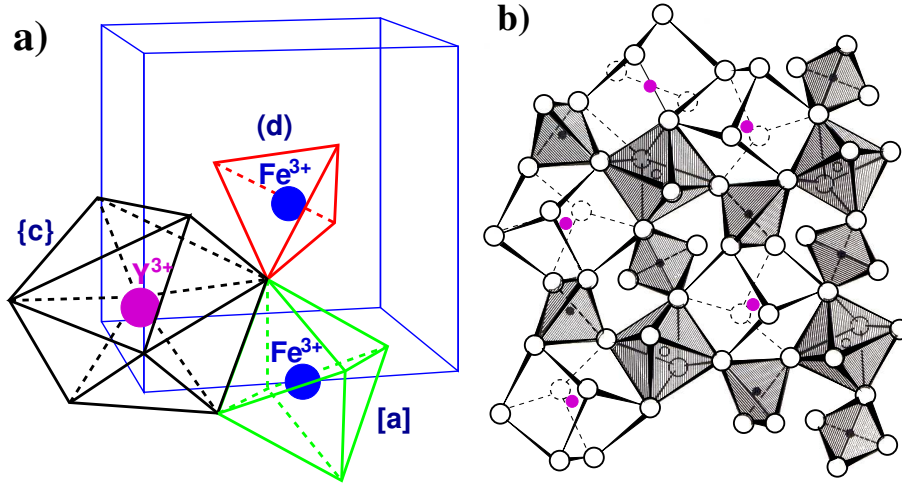


Figure 2.2: The garnet structure, adapted from [3]. Arrangement of the [a], {c}- and (d)-sites at the centers of octahedra, dodecahedra and tetrahedra, respectively. The cube represents one octant of the unit cell. (b) Spatial connection of oxygen polyhedra in YIG, adapted from [4]. The large open circles represent oxygen anions and the small circles represent cations.

A unit cell of YIG contains 8 formula units and has a lattice constant of 12.376\AA . It is a rather loose structure with a volume of 236.9\AA^3 per formula unit, which has the great technical advantage that it is possible to accommodate a very wide variety of cations in the garnet structure. Thus, it is feasible to achieve an enormous range of control of the magnetic properties in the garnet structure system. The largest of the rare-earth iron garnets that can be formed is $\text{Sm}_3\text{Fe}_5\text{O}_{12}$ with a lattice constant of 12.529\AA and the smallest is $\text{Lu}_3\text{Fe}_5\text{O}_{12}$ with a lattice constant of 12.283\AA .

2.3 Magnetic properties

The fundamental magnetic properties of the iron garnets have their origin in the magnetic ions (principally Fe^{3+}) and their relationship to the surrounding oxygen ions. The oxygen ions influence the electronic configuration of the enclosed iron ions and

mediate a superexchange interaction between the iron on octahedral (a) and tetrahedral (d) sites. The magnetic moments of Fe^{3+} ions in different crystallographic sites are antiferromagnetically coupled and therefore opposing one another, as illustrated in Figure 2.3. Each of the iron ions is in a $3d^5$ electronic configuration and has a magnetic moment of $5\mu_B$. Because there are three Fe^{3+} ions in tetrahedral (d) sites and two in octahedral sites, the resultant magnetic moment is $5\mu_B$ per formula unit from the two Fe^{3+} ion sub-lattices.

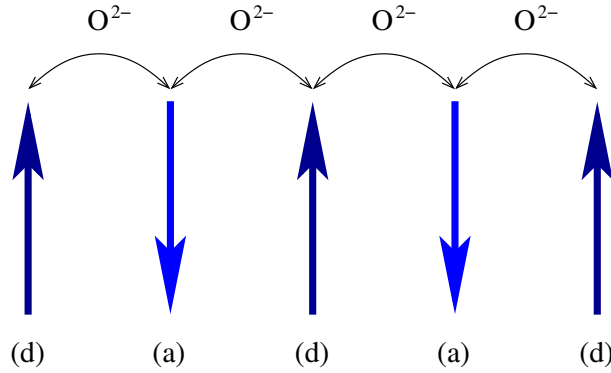


Figure 2.3: Illustration of the antiferromagnetic superexchange coupling of the magnetic moments of Fe^{3+} ions on tetrahedral (d) and octahedral (a) sites mediated by O^{2-} . Of the five iron ions in a formula unit of YIG three are located in (d) sites and two in (a) sites, giving a resulting magnetic moment of $5\mu_B$.

The antiferromagnetic superexchange interaction of the two iron sublattices makes YIG an ideal Néel ferrimagnet [5], however, substitution of a magnetic rare earth ion for the diamagnetic Y^{3+} in YIG causes a third sublattice to enter the picture.

2.4 Substituted rare-earth iron garnets

Substitution of a wide range of ions for Fe^{3+} on the tetrahedral and octahedral sites and for Y^{3+} on the dodecahedral site of YIG is possible, and will alter its properties in various ways. For instance, there are two classical methods for reducing the saturation magnetization M_s . The first method consists in substituting the Fe^{3+} ions with nonmagnetic ions such as Ga^{3+} which will occupy mainly tetrahedral sites. This reduces the magnetic contribution from this sublattice, and thereby leads to a reduction of the net magnetization. The second method consists in substituting the nonmagnetic yttrium ions in dodecahedral sites with rare earth ions with a magnetic

moment that counteracts the resultant magnetization of the iron ions. This tends to reduce M_s at room temperature with respect to that of YIG.

All of the rare earth ions from Gd^{3+} through Yb^{3+} have magnetic moments. When any of these are present in the dodecahedral site, it is found that the magnetization M_s as a function of temperature shows a compensation point, i.e. a temperature T_{comp} at which the spontaneous magnetization reaches zero. The compensation point arises because the sublattice formed by the magnetic rare earth ions typically has a different temperature dependence from that of the two Fe^{3+} sublattices.

2.5 Growth

Garnets for applications are most commonly thin single crystalline films produced by epitaxial growth. Nonmagnetic gadolinium gallium garnet (GGG) has nearly the same lattice constant as yttrium iron garnet, and has for this reason become the prime substrate for epitaxial growth of thin garnet films. To obtain perfect and unstrained epilayers the lattice constants of film and substrate have to be matched by proper substitution to a level of mismatch below about 0.02\AA .

Liquid phase epitaxy (LPE) is the most commonly used growth technique. It is based on dipping of perfectly polished and cleaned substrate wafers into a molten garnet flux system. Homogeneous crystal growth then takes place on the substrate surface. A property of garnet films grown by LPE is that they are no longer cubic [1]. As a consequence of this symmetry breaking, a linear magnetoelectric effect and nonlinear optical effects have been observed in garnet thin films, which are forbidden in media that possess a center of inversion [6, 7].

2.6 Optical and magneto-optical properties

YIG has a band gap of about 2.9eV and is highly transparent ($\alpha \ll 0.03\text{cm}^{-1}$) to light in the infrared wavelength region between 1.5 and $5\text{ }\mu\text{m}$ [1]. At longer wavelengths absorption is caused by lattice vibrations, while at shorter wavelengths electronic transitions within the Fe^{3+} ion (crystal field transitions) and charge transfer transitions are responsible for the optical absorption. See Figure 2.4. Rare-earth substituted iron garnets exhibit absorption peaks in the infrared region of the spectrum characteristic of the particular rare earth elements.

YIG and rare earth iron garnets exhibit strong magneto-optical Faraday and Kerr effects. The microscopic origin of these large effects are not fully understood, but they are believed to originate from the high-energy charge transfer optical transitions, with the effect extending down through the visible and the near infrared spectral regions [1]. In YIG, the contribution of the octahedral iron sublattice to the Faraday rotation is larger than that of the tetrahedral iron sublattice. This has the interesting

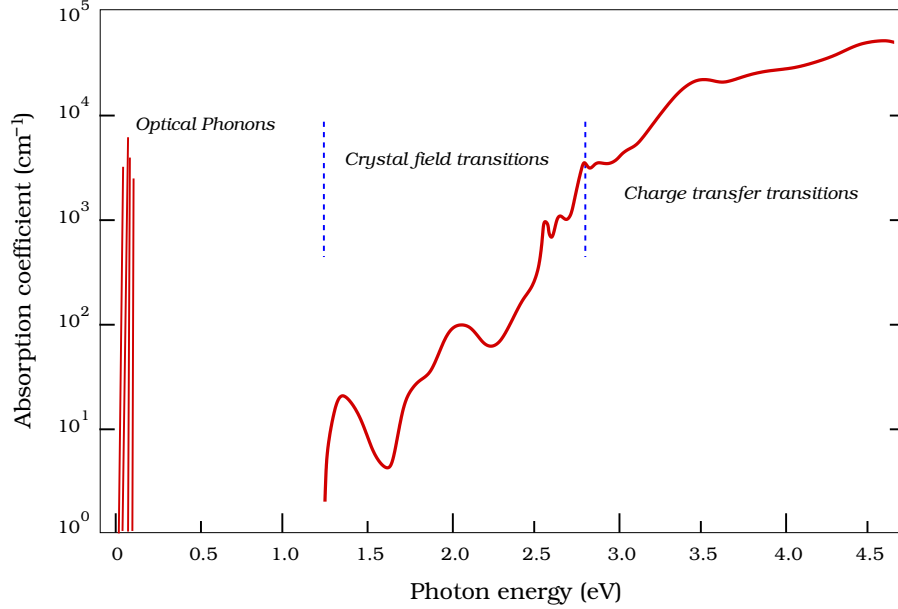


Figure 2.4: Optical absorption spectrum of YIG.

consequence that rare earth substituted garnets with a compensation point T_{comp} where the overall magnetization is zero may still have a Faraday rotation at T_{comp} .

Substitution of part of the Y^{3+} on dodecahedral sites by the diamagnetic Bi^{3+} has been found to increase the Curie temperature. It also has the effect of strongly enhancing the magneto-optical properties of YIG. For this reason bismuth-substituted yttrium iron garnets have had an important impact in the area of magneto-optic materials.

2.7 Garnets studied in this work

In this work, a series of thin single-crystalline garnet films with chemical composition $\text{Lu}_{3-x-y-z}\text{Y}_x\text{Bi}_y\text{Pb}_z\text{Fe}_{5-w}\text{Ga}_w\text{O}_{12}$ have been studied. The films were grown by isothermal liquid phase epitaxy onto (100) oriented Gadolinium Gallium Garnet (GGG) substrates. They contain small amounts of Pb impurities, typically of the order of $z = 0.05$, due to the flux ($\text{Bi}_2\text{O}_3/\text{PbO}/\text{B}_2\text{O}_3$) which they were grown from. During the growth process, various parameters were controlled to create low magnetic coercivity and in-plane magnetization. The film final thickness was measured using

Scanning Electron Microscopy (SEM) and later confirmed by optical techniques [8] (Chapter 4), while the actual composition of the films was determined with an Electron MicroProbe (EMP). The films that have been studied here were all grown at the University of Oslo in the group of Prof. Tom Henning Johansen, to serve as indicators for the visualization of magnetic fields in superconductors [9, 10, 11].

The saturation magnetization of the films are in the range $4\pi M_s = 0.5 - 1\text{kG}$, depending on the composition. The coercivity is very low, and the films exhibit a strong magneto-optical response due to the Bi substitution [8, 12] (Chapter 4). In the absence of an external magnetic field, the magnetization forms very large domains and typically leave the whole sample in a single-domain state. However, with the aid of an applied field, domains can be created and easily observed in a polarizing microscope, see Figure 2.5. From Vibrating Sample Magnetometer (VSM) measurements, a small four-fold symmetric magnetic anisotropy has been identified in the film plane, consistent with the 90° domain formations seen in the figure.

The films are practically ideal for magneto-optical (MO) imaging and visualization of magnetic fields. An example of this is shown in Figure 2.5, where bits on the magnetic strip of a credit card can be clearly seen under a polarizing microscope.

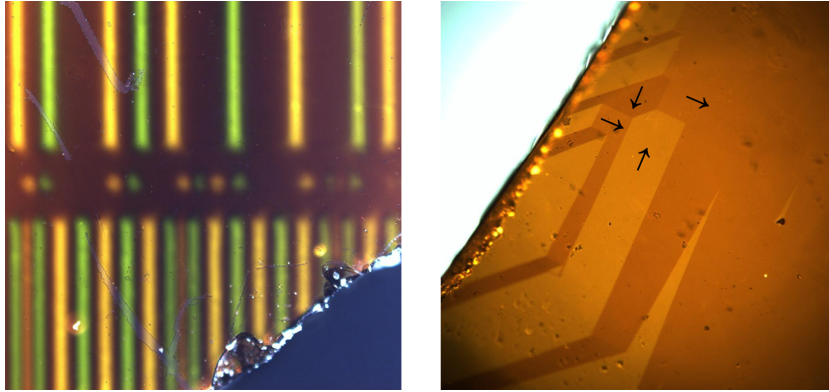


Figure 2.5: MO images of magnetic bits on a credit card (left) and large in-plane domains in a garnet film (right). The arrows are suggested magnetization directions of the domains. The images were obtained using a polarizing optical microscope.

References

- [1] G. Winkler, *Magnetic Garnets* (Friedr. Vieweg & Sohn, Braunschweig, Germany, 1981).
- [2] A. Paoletti, ed., *Physics of Magnetic Garnets*, Enrico Fermi International School of Physics, Italian Physical Society (North-Holland Publishing Co., 1978), ISBN 0-444-85200-x.
- [3] M. A. Gilileo and S. Geller, Phys. Rev. **110**, 73 (1958).
- [4] G. A. Novak and G. V. Gibbs, Amer. Mineralog. **56**, 791 (1971).
- [5] L. Néel, Ann. Phys. (Paris) **3**, 137 (1948).
- [6] B. B. Krichevtsov, V. V. Pavlov, and R. V. Pisarev, Zh. Eksp. Teor. Fiz. **49**, 466 (1989), [JETP Lett. **49**, 535 (1989)].
- [7] R. Pisarev, B. Krichevtsov, V. Gridnev, V. Klin, D. Fröhlich, and C. Pahlke-Lerch, J. Phys.: Condens. Matter **5**, 8621 (1993).
- [8] F. Hansteen, L. E. Helseth, T. H. Johansen, O. Hunderi, A. Kirilyuk, and T. Rasing, Thin Sol. Films **455-456C**, 429 (2004).
- [9] P. Goa, H. Hauglin, M. Baziljevich, E. Il'yashenko, P. Gammel, and T. Johansen, Supercond. Sci.Tech. **14**, 729 (2001).
- [10] L. Helseth, R. Hansen, E. Il'yashenko, M. Baziljevich, and T. Johansen, Phys. Rev. B **64**, 174406 (2001).
- [11] T. Johansen and D. Shantsev, eds., *Magneto-Optical Imaging*, vol. 142 of *NATO Science Series II: Mathematics, Physics and Chemistry* (Kluwer Academic Publishers, 2004), ISBN 1-4020-1997-1.
- [12] L. E. Helseth, Ph.D. thesis, University of Oslo (2002).

CHAPTER 3

Experimental techniques

Linear, nonlinear and time resolved magnetooptical techniques have become indispensable for the study and characterization of magnetic materials. They are non-destructive, and allow one to probe the magnetic ordering in ferromagnets, antiferromagnets and complex magnetic nanostructures with high spatial resolution and extreme temporal resolution.

This chapter introduces the three main experimental techniques used in this Ph.D. work for the characterization of magnetic garnet films, and for the ultrafast optical control of their magnetization. The experimental setups described here, namely, a spectroscopic ellipsometer with software for control and data analysis, a setup for measuring MSHG in a transmission geometry, and an all-optical pump and probe experiment, were all built as part of this thesis work.

3.1 Ellipsometry

Ellipsometry is a very sensitive measurement technique for the characterization of thin films, surfaces and material microstructure. It is based on the careful analysis of the change in polarization experienced by light during reflection from or transmission through a sample (see Fig. 3.1). Some of the information that is routinely extracted from ellipsometry measurements include:

- Optical constants ($N = n + ik$) of thin films or bulk materials

- Thickness of thin films
- Surface and interface roughness
- Optical anisotropy

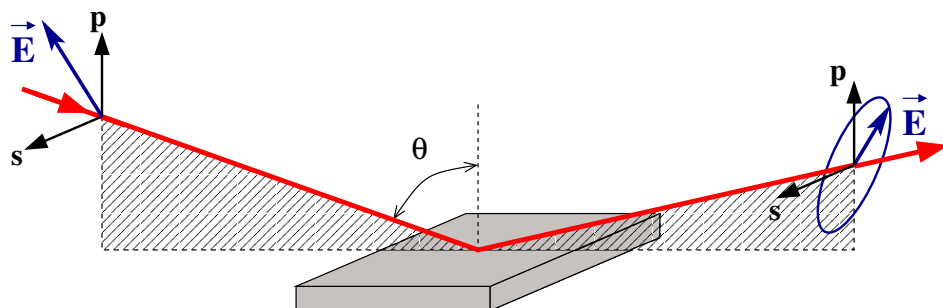


Figure 3.1: The principle of ellipsometry. Light with a known state of polarization, typically linear, is incident on a sample at an angle of incidence θ . After reflection from the sample the generally elliptical state of polarization of the reflected light is carefully analyzed. The orientation of the major axis of the ellipse and its ellipticity (ratio of minor to major axis) depends on the optical properties of the sample. Precise measurements of these parameters can, through fitting of the measurement data to model calculations, give important information about the unknown properties of the sample. The vectors \mathbf{p} and \mathbf{s} are parallel and perpendicular to the plane of incidence, respectively, and form the basis vectors for the description of the polarization.

However, the amount and type of information that can be obtained by ellipsometry relies strongly on a prior knowledge of the sample. The actual measurement probes only the relative change in amplitude and phase of the reflected light, so in order to relate this to the unknown parameters of a sample, a mathematical model of the sample's optical response is needed. The unknown parameters of the model can then be determined by numerical ¹ fitting to the measurement data. The correct model can only be constructed when the physical structure of the sample is known. It is, for instance, crucial to know whether we are dealing with a bulk sample, a single thin film or a multilayer structure. Moreover, for the fitting procedure to yield reliable information, the model should not contain too many unknown parameters. For instance, if seeking to determine the thickness of a thin film grown on top of a substrate,

¹In most cases an analytical solution for the unknowns in terms of the measured polarization change can not be found. Therefore, numerical fitting of model calculations to measurement data is the standard approach to extracting information from ellipsometry measurements.

prior knowledge of the dielectric function of both the substrate material and the film simplifies the task significantly.² As will be discussed in the following sections, an ellipsometry measurement yields two independent parameters Ψ and Δ at a given wavelength and incidence angle, and allows therefore in principle for two unknown parameters to be determined. However, in some cases more than two unknowns can be determined thanks to various techniques [1, 2], while in other cases it can be impossible to determine more than a single unknown quantity due to strong parameter correlation in the model.

Several different instrumental realizations of ellipsometers exist, each with its particular strengths and weaknesses [2, 3, 4, 5, 6]. A detailed discussion of these is not within the scope of this thesis, however, the so-called rotating analyzer (RA) ellipsometer will in the following be described in some detail. An ellipsometer of this type was built in Trondheim as part of this Ph.D. work, and used for the initial studies of magnetic garnet films. Additionally, the commercial ellipsometer from J.A. Woollam Co., Inc. used for the more detailed characterization of garnet films in Nijmegen is of the rotating analyzer type. These two ellipsometers are depicted in Figure 3.2.

3.1.1 Variable Angle Spectroscopic Ellipsometry (VASE)

Ellipsometry is most powerful when the measurements are performed at several angles of incidence and across a wide spectral range. Measurements at different angles produce more data points for the numerical fitting, and can for certain samples be used to fundamentally increase the available information about the sample. Spectral measurements additionally open up for fitting with dispersion models that describe the dielectric function of a material (in a limited spectral range) by only a few free parameters. This can significantly reduce the number of unknowns in a model, and thereby permit more information to be extracted.

Instruments that can vary both the angle of incidence and the wavelength of the incident light are commonly denoted Variable Angle Spectroscopic Ellipsometers (VASE). Computer controlled goniometer arms enable control of the incidence angle, while a broadband light source such as a Xe arc lamp is used in combination with a monochromator in order to achieve the spectral resolution. Polarizers and other optical component operating in transmission should be made from materials with high transmittivity in the spectral region of interest. For good performance also in the UV part of the spectrum MgF_2 , which is transparent to light with wavelengths from about 140nm to $7\mu\text{m}$, is a good material. The problem of UV absorption in glass lenses can be circumvented by using focusing mirror optics instead.

²It should be noted that there can be very significant differences between the optical constants measured from a bulk specimen of a material and the optical constants of a thin film of the same material. Therefore, employing bulk optical constants from literature for the analysis of thin films of the same material may yield incorrect results.

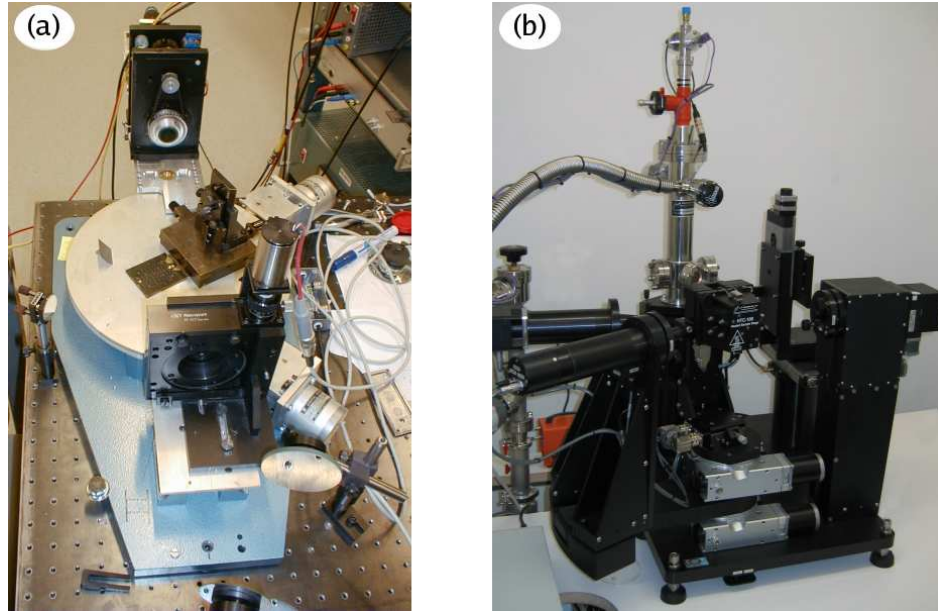


Figure 3.2: The two ellipsometers used for characterization of magnetic garnet films: (a) The home built system in Trondheim and (b) the commercial system from J.A. Woollam Co., Inc. in Nijmegen.

3.1.2 The Rotating Analyzer Ellipsometer

Ellipsometers employ various polarization modulation techniques to improve the sensitivity and speed of measurements. The instruments are often classified as null ellipsometers, rotating element ellipsometers, or phase modulated ellipsometers, according to their employed principle of modulation. In a null ellipsometer the polarization is not modulated, while the rotating element type ellipsometer uses a mechanically rotating polarizer, analyzer or compensator. Phase modulated ellipsometers have a fixed polarizer and analyzer and use a photoelastic (birefringent) modulator to introduce a time-dependent relative phase shift between the s- and p-polarized electric field components of the incident light.

In a rotating analyzer ellipsometer (RAE) the analyzer is constantly rotating at a frequency of about 10-100Hz while a detector records the transmitted intensity as function of the analyzer angle. This is illustrated in the schematic setup shown in Figure 3.3. The incident polarization is set with a polarizer, typically oriented at 45 degrees with respect to the plane of incidence. Other states of polarization,

including elliptical, can be generated using a compensator plate in combination with the polarizer, and may be useful for improving the sensitivity in special cases.

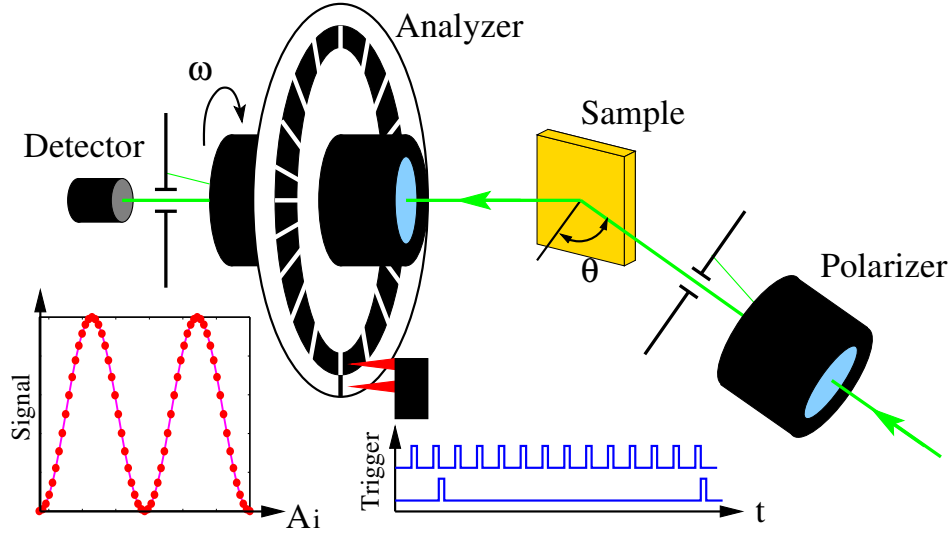


Figure 3.3: The principles of a rotating analyzer ellipsometer. The polarization of light incident on the sample at an angle θ is set using a polarizer. After reflection from the sample the light passes through the analyzer rotating at a constant speed ω . An encoder disk and two photo sensors are used to generate trigger pulses for the data acquisition. This technique ensures that despite small variations in rotation speed, data points are acquired at the same orientation of the analyzer for every rotation. The typically sinusoidal intensity variation (signal) recorded for one full rotation of the analyzer is shown in the inset below the detector.

Polarizers of the Rochon type generally have a high extinction ratio and do not cause any shift of the ordinary beam. Not shifting the beam is particularly important for the polarizer acting as rotating analyzer, since any wobbling of the beam on the detector can significantly affect the sensitivity of the instrument. An iris diaphragm is used immediately after the polarizer to block the unwanted extraordinary beam which emerges at an angle of a few degrees with respect to the ordinary beam.

After reflection from the sample, the light passes through the analyzer which rotates with a constant speed ω . An encoder disk with reflecting and non-reflecting stripes is attached to the analyzer. Two photo diodes monitor these stripes, one producing an electrical trigger pulse for every full rotation of the analyzer, while the other emits trigger pulses during the rotation at a number of equally spaced points.

There are typically 64, 128 or 256 pulses per rotation which are used to trigger the data acquisition. This technique ensures that despite small fluctuations in the rotation speed, intensity readings are acquired at the exact same orientation of the analyzer for every rotation, and can thus be averaged to improve the signal to noise ratio. The typically sinusoidal signal recorded during one full rotation of the analyzer is shown below the detector in Figure 3.3.

A suitable detector must have a linear intensity response, and be insensitive to the polarization of light. Semiconductor photo diodes based on Silicon are well suited for photon energies above the band gap at about 1.12eV ($\lambda = 1100\text{nm}$). For lower energies, down to about 0.56eV ($\lambda = 2200\text{nm}$) Si/InGaAs photodiodes can be used. In order to operate at wavelengths much further into the IR or UV parts of the spectrum not only the detector needs to be replaced, but also the light source, polarizers and other optical components [7, 8].

The data acquisition can be controlled by a computer equipped with an AD-converter board and external trigger inputs. As will be explained in the following section, a Fourier analysis of the acquired signal gives the ellipsometric quantities Ψ and Δ which can be related to the sample's physical properties through mathematical modeling and data fitting.

3.1.3 Jones Matrix Analysis

The polarization of light as it propagates through the ellipsometer shown in Figure 3.3 can be analyzed in the Jones or Muller matrix formalism [6]. In the Jones formalism, the vector \mathbf{J}_D that describes the state of polarization of light reaching the detector can be written as

$$\mathbf{J}_D = \begin{pmatrix} E_p \\ E_s \end{pmatrix} \propto \mathbf{R}(-A) \begin{pmatrix} 1 & 0 \\ 0 & 0 \end{pmatrix} \mathbf{R}(A) \begin{pmatrix} r_{pp} & r_{sp} \\ r_{ps} & r_{ss} \end{pmatrix} \begin{pmatrix} \cos P \\ \sin P \end{pmatrix} \quad (3.1)$$

Here P denotes the angle of the polarizer that sets the polarization of the light incident on the sample, and the s- and p-directions defined in Figure 3.1 are used as orthogonal basis vectors. The sample reflectivity matrix

$$\mathbf{S} = \begin{pmatrix} r_{pp} & r_{ps} \\ r_{sp} & r_{ss} \end{pmatrix}. \quad (3.2)$$

with complex valued elements r_{ij} represents the change in polarization taking place during reflection from the sample. The diagonal elements r_{pp} and r_{ss} are the complex Fresnel amplitude reflection coefficients for p- and s-polarized light, respectively. They describe the change in amplitude and phase experienced by light upon reflection from the sample. They depend on the angle of incidence as well as the optical properties of the sample. Similarly, the off-diagonal elements r_{sp} and r_{ps} represent the transformation of incident p-polarized light into s-polarization and vice versa, upon

reflection of light from the sample. These elements are nonzero only for anisotropic samples, including chiral and magnetooptically active materials. The matrix \mathbf{R} in Eq. 3.2 represents the rotation of the reference coordinate system through an angle ϑ and is given by

$$\mathbf{R}(\vartheta) = \begin{pmatrix} \cos \vartheta & \sin \vartheta \\ -\sin \vartheta & \cos \vartheta \end{pmatrix}. \quad (3.3)$$

The analyzer is represented by the Jones matrix

$$\mathbf{P}_A = \begin{pmatrix} 1 & 0 \\ 0 & 0 \end{pmatrix}. \quad (3.4)$$

A suitable photo detector must exhibit a linear intensity response and not be polarization sensitive. The intensity I_D of light (averaged over several optical cycles) on detector is then

$$I_D \propto \langle \mathbf{J}_D^* \mathbf{J}_D \rangle, \quad (3.5)$$

where $*$ denotes the complex conjugate. After performing the matrix multiplications of Equations 3.1 and 3.5 one finds that the intensity I_D of light on the detector can be expressed as

$$I_D \sim 1 + a_2 \cos 2A + b_2 \sin 2A, \quad (3.6)$$

where A is the analyzer angle. The coefficients a_2 and b_2 denote the so-called second order Fourier coefficients which can be expressed in terms of the sample reflectivity matrix \mathbf{S} (Eq. 3.2) and the polarization angle P of the incoming light:

$$a_2 = \frac{XX^* - YY^*}{XX^* + YY^*} \quad (3.7)$$

$$b_2 = \frac{YX^* + XY^*}{XX^* + YY^*} \quad (3.8)$$

with

$$X = r_{pp} \cos P + r_{ps} \sin P \quad (3.9)$$

$$Y = r_{sp} \cos P + r_{ss} \sin P. \quad (3.10)$$

A digital Fourier transform of the recorded detector signal, normalized to the zero-frequency DC component, directly gives the coefficients a_2 and b_2 . The presence of other (first order or higher order) non-zero Fourier components in the measured signal is not related to the optical response of the sample. However, these can be used for instrument diagnostics as indicators of misalignments or other problems [9, 10].

For an isotropic sample $r_{sp} = r_{ps} = 0$ and Eqs. 3.7 and 3.8 reduce to

$$a_2 = \frac{|r_{pp}|^2 \cos^2 P - |r_{ss}|^2 \sin^2 P}{|r_{pp}|^2 \cos^2 P + |r_{ss}|^2 \sin^2 P} \quad (3.11)$$

$$b_2 = \frac{r_{pp}^* r_{ss} \cos P \sin P + r_{pp} r_{ss}^* \cos P \sin P}{|r_{pp}|^2 \cos^2 P + |r_{ss}|^2 \sin^2 P} \quad (3.12)$$

The complex ratio of r_{pp} to r_{ss} , can be written in the exponential form

$$\rho = \frac{r_{pp}}{r_{ss}} = \frac{|r_{pp}|}{|r_{ss}|} e^{i(\delta_{r_{pp}} - \delta_{r_{ss}})} = \tan(\Psi) e^{i\Delta}, \quad (3.13)$$

which is known as the fundamental equation of ellipsometry. Ψ is the magnitude of the ratio r_{pp}/r_{ss} , while Δ is the phase difference between the s- and p-polarized components of the light, caused by reflection from the sample. Combining this with Eqs. 3.11 and 3.12, the quantities Ψ and Δ can be expressed as functions of the Fourier coefficients a_2 and b_2 and the incident polarization P .

$$\tan \Psi = \sqrt{\frac{1+a_2}{1-a_2}} |\tan P| \quad (3.14)$$

$$\cos \Delta = \frac{b_2}{\sqrt{1-a_2^2}} \frac{\tan P}{|\tan P|} \quad (3.15)$$

3.1.4 Modeling and fitting

The greatest challenge in ellipsometry lies in extracting the desired information about a sample from the measurements of Ψ and Δ . With the exception of a few special cases, this can only be done by numerically fitting the unknown parameters of a mathematical model to the measurement data. The output from a model calculation are the elements of the sample reflectivity matrix \mathbf{S} of Eq. 3.2, from which Ψ and Δ can easily be determined when θ and P are known. For the simplest case of an isotropic bulk sample the off-diagonal elements $r_{ps} = r_{sp} = 0$, and the diagonal elements r_{pp} and r_{ss} are simply the Fresnel amplitude reflection coefficients for the single interface.

$$r_{pp} = \frac{\sqrt{\epsilon_1} \cos \theta_0 - \sqrt{\epsilon_0} \cos \theta_1}{\sqrt{\epsilon_1} \cos \theta_0 + \sqrt{\epsilon_0} \cos \theta_1} \quad (3.16)$$

$$r_{ss} = \frac{\sqrt{\epsilon_0} \cos \theta_0 - \sqrt{\epsilon_1} \cos \theta_1}{\sqrt{\epsilon_0} \cos \theta_0 + \sqrt{\epsilon_1} \cos \theta_1}, \quad (3.17)$$

where

$$\sqrt{\epsilon_0} \sin \theta_0 = \sqrt{\epsilon_1} \sin \theta_1. \quad (3.18)$$

For more complex sample structures such as thin film multilayers, the model for \mathbf{S} must take into account the Fresnel coefficients of each interface as well as the thickness of every layer. The calculations are commonly done using various optical

matrix formalisms [5, 6, 11, 12], which can also incorporate the effects of anisotropic and magnetooptically active materials [13]. Surface roughness and interfacial mixing can have a profound influence on the optical response of a sample. Well established techniques exist for also including these effects into the model [14].

In the relatively simple case of a single isotropic and transparent thin film on top of an absorbing substrate, the model contains only 4 parameters at a given wavelength and incidence angle; the complex permittivity of the substrate $\epsilon^s = \epsilon_r^s + i\epsilon_i^s$, the thickness of the film d , and its real permittivity ϵ_r^f . If the substrate optical properties are known, then both the unknown parameters d and ϵ_r^f can in principle be determined from the measurements of the two quantities Ψ and Δ . The number of parameters needed in the model increases rapidly with the number of layers, especially if they are absorptive, anisotropic or form imperfect interfaces. Measurements of Ψ and Δ at multiple wavelengths can often be used to determine more than two unknown parameters. A common technique is to simultaneously consider a range of wavelengths and to reduce the total number of unknowns in this range by employing a dispersion model for the unknown permittivity. Dispersion models can be either empirically or theoretically based, and describe the spectral variation of the permittivity as function of only a few parameters. One example is the Cauchy model

$$n(\lambda) = \sqrt{\epsilon_r} = A + B\lambda^{-2} + C\lambda^{-4} \quad (3.19)$$

which is well suited to describe the real part of the permittivity for many dielectrics and semiconductors at photon energies below the band gap. Some other examples are the Lorentz oscillator model, the Drude model and the Tauc-Lorentz model [1].

In order to determine the best fit value of the unknown model parameters a numerical algorithm is needed to effectively explore the potentially large parameter space in search of the global minimum of the cost function

$$f = \sum_{i=1}^N \left[\left(\Psi_i^{\text{calc}} - \Psi_i^{\text{measured}} \right)^2 + \left(\Delta_i^{\text{calc}} - \Delta_i^{\text{measured}} \right)^2 \right]. \quad (3.20)$$

Here Ψ_i^{measured} and $\Delta_i^{\text{measured}}$ represent measurements at wavelengths λ_i , while Ψ_i^{calc} and Δ_i^{calc} are the corresponding model calculations. Various algorithms, such as the Levenberg-Marquardt, simulated annealing, energy landscape paving, and genetic algorithms, can be used to tackle this minimization problem [15]. A seemingly good fit can sometimes be obtained with an insufficient or completely wrong model. In such cases, the obtained values of the fit parameters are of course useless. Because ellipsometry is a model based technique, it is critical to use the right model in order to get reliable results.

3.2 Magnetization-induced Second-Harmonic Generation (MSHG)

The generation of laser pulses with ever shorter duration has made it possible to obtain extreme peak intensities and tremendous corresponding electromagnetic field strengths [16]. The electric fields of picosecond and femtosecond laser pulses can easily be made comparable in strength to the internal fields of atoms in a material. Consequently, the laser light can no longer be considered simply as a small perturbation of the atom, and several new phenomena arise in this high-intensity regime.

Generation of light at the double frequency, or second-harmonic generation (SHG) is just one of the numerous nonlinear optical processes that can occur as a consequence of the interaction between intense laser-light and matter. SHG has found important applications in frequency conversion of light, and has become a valuable tool for the study of the surfaces and interfaces of materials [17]. The interface sensitivity stems from the fact that SHG is forbidden in media with space inversion symmetry, including many isotropic media such as glasses, liquids and gasses, but allowed at surfaces and interfaces where the space inversion symmetry is broken [18]. Furthermore, at the surfaces and interfaces of magnetic materials, additional magnetization dependent contributions to the SHG appear due to the simultaneous breaking of time-reversal symmetry by the magnetic ordering. These contributions allow for probing of the magnetic structure of ferromagnets as well as antiferromagnets. During the past two decades (MSHG) has been developed into a powerful and well-established technique for the study of surfaces and interfaces of buried magnetic multilayers [19, 20, 21, 22, 23].

3.2.1 Phenomenology of MSHG

A light wave consists of electric and magnetic fields which vary sinusoidally at high frequencies. When light propagates through matter it will therefore induce a motion of the charged particles that constitute the material, and they form oscillating electric dipoles. The contribution from the magnetic field part of the light and from electric quadrupoles is much weaker and is usually neglected. This is called the electric-dipole approximation. The oscillating dipoles add up to a macroscopic polarization \mathbf{P} which is used to describe the response of the material. For low light intensities, i.e. small amplitudes of the electric field \mathbf{E} , the charges can follow the field almost exactly and the relationship between \mathbf{E} and \mathbf{P} is essentially linear. For larger amplitudes the motion of the particles will be distorted and nonlinear terms will be important. Provided that these new terms are still small compared to the linear one the induced polarization \mathbf{P} can be expanded in powers of the electric field \mathbf{E} of the incident wave [18]:

$$\mathbf{P} = \chi^{(1)}\mathbf{E} + \chi^{(2)}\mathbf{E}\mathbf{E} + \chi^{(3)}\mathbf{E}\mathbf{E}\mathbf{E} \dots \quad (3.21)$$

The coefficients $\chi^{(n)}$ are the frequency dependent electric susceptibilities of order n . The first order susceptibility gives rise to the linear optical response, while the higher order terms give rise to non-linear optical effects that become significant for strong incident fields \mathbf{E} . The term quadratic in the electric field in Eq. (3.21) gives rise to important effects such as second-harmonic generation (SHG), sum- and difference-frequency generation, optical rectification and many more. In a material with inversion symmetry, there can be no even powers of the field in the expansion of the polarization, and the lowest-order nonlinearity is then the cubic term in Eq. (3.21).

In the presence of a magnetization \mathbf{M} , each of the susceptibilities $\chi^{(n)}$ should be further expanded in powers of \mathbf{M} :

$$\chi^{(n)} = \chi_0^{(n)} + \frac{\delta\chi^{(n)}}{\delta\mathbf{M}}\mathbf{M} + \dots \quad (3.22)$$

The first term, independent of \mathbf{M} , can be thought of as the purely crystallographic contribution, while the higher order terms may only exist in the presence of a magnetization. These give rise to an additional magnetic contribution (to the SHG). In the following we consider only contributions up to first order in \mathbf{M} .

The second order non-linear polarization at frequency 2ω induced by an incident field $\mathbf{E} = (E_x, E_y, E_z)$ of frequency ω in a medium with static magnetization $\mathbf{M} = (M_x, M_y, M_z)$ can be written as a sum of crystallographic and magnetization induced contributions:

$$\begin{aligned} P_i(2\omega) &= P_i^{(cr)}(2\omega) + P_i^{(m)}(2\omega) \\ &= \chi_{ijk}^{(cr)} E_j(\omega) E_k(\omega) + \chi_{ijkl}^{(m)} E_j(\omega) E_k(\omega) M_l(0), \end{aligned} \quad (3.23)$$

where $\{i, j, k, l\} = \{x, y, z\}$. Here $\chi_{ijk}^{(cr)}$ is a third rank polar tensor representing the crystallographic contribution, and $\chi_{ijkl}^{(m)}$ is a fourth rank axial tensor representing the magnetization induced contribution. The symmetry of the medium imposes restrictions on the susceptibility tensor according to Neumann's principle, thereby reducing the number of independent tensor components [24].

The observable intensity of radiated light at the second harmonic frequency is proportional to the square of the induced polarization at 2ω [25]:

$$\begin{aligned} I(2\omega) &\propto |\mathbf{P}(2\omega)|^2 \\ &\propto |\mathbf{P}^{(cr)}(2\omega) + \mathbf{P}^{(m)}(2\omega)|^2 \\ &\propto |\mathbf{P}^{(cr)}|^2 + |\mathbf{P}^{(m)}|^2 + 2|\mathbf{P}^{(cr)}||\mathbf{P}^{(m)}|\cos\Phi. \end{aligned} \quad (3.24)$$

Generally, if both crystallographic and magnetic contributions exist, they will interfere. An exception is when $\mathbf{P}^{(cr)}$ and $\mathbf{P}^{(m)}$ are induced along orthogonal directions so that the angle Φ between $\mathbf{P}^{(cr)}$ and $\mathbf{P}^{(m)}$ is $\pi/2$ and thus $\cos\Phi = 0$.

Note that the magnetization induced contribution $P_i^{(m)} = \chi_{ijkl} E_j E_k M_l$ is proportional to \mathbf{M} (Eq. 3.23). It therefore changes sign if the direction of the magnetization is reversed, while the crystallographic part $P_i^{(cr)}$ remains unchanged. For the interference term in Equation 3.24 this means that the angle Φ between $\mathbf{P}^{(cr)}$ and $\mathbf{P}^{(m)}$ is changed by π , so that $\Phi' = \Phi \pm \pi$ and $\cos \Phi' = -\cos \Phi$. Thus, if $\mathbf{P}^{(cr)}$ and $\mathbf{P}^{(m)}$ are not orthogonal, one can observe a magnetic contrast, i.e. a difference in the measured intensity $I(2\omega)$ for $\pm \mathbf{M}$.

The time dependence of the vector components of the induced polarization (both crystallographic and magnetic) can be written on the form

$$P_i(2\omega) = P_i^0 e^{i(2\omega t + \delta_i)} \quad (3.25)$$

where the amplitude P_i^0 is real. The measurable intensity of the second harmonic wave polarized along one of the coordinate axes $i = \{x, y, z\}$ is therefore

$$\begin{aligned} I_i(2\omega) &= |P_i^{(cr)} e^{i(2\omega t + \delta_i^{(cr)})} + P_i^{(m)} e^{i(2\omega t + \delta_i^{(m)})}|^2 \\ &= P_i^{(cr)2} + P_i^{(m)2} + 2P_i^{(cr)} P_i^{(m)} \cos \Delta_i, \end{aligned} \quad (3.26)$$

with $\Delta_i = \delta_i^{(cr)} - \delta_i^{(m)}$ being the phase difference between the crystallographic and magnetic contributions. Analogously to Equation (3.24), the interference term will vanish also if the phase difference $\Delta = \pi/2$. In an ideal non-absorptive medium $\chi^{(cr)}$ is purely real valued while $\chi^{(m)}$ is purely imaginary, leading to $\Delta = \pi/2$ and thus no magnetic contrast in the SHG signal.

Information about the relative phase Δ between crystallographic and magnetic contributions to the SHG is generally lost when measuring intensities. However, it may be recovered using a technique based on interference with an external reference sample [26].

3.2.2 Experimental setup for MSHG rotational anisotropy

This section describes the experimental setup used to study MSHG from transparent magnetic garnet films. The experiments were performed in a transmission geometry at normal incidence. A magnetic field was applied either parallel or perpendicular to the garnet film, and the the MSHG signal was measured as function of both the applied field strength and the sample azimuthal angle ϕ .

The 160fs laser pulses at $\lambda = 840\text{nm}$ from a Coherent Mira 900 Ti:Sapphire laser was used to induce a nonlinear optical response in the garnet films. In order to reduce the average power incident on the sample, the 76MHz laser pulse train was passed through a chopper operating at a few hundred Hertz. The polarization of the pulses was set using a $\lambda/2$ -plate followed by a Glan Laser polarizer. By use of a lens, the laser pulses were focused to a spot size of about $200\mu\text{m}$ on the sample. To ensure

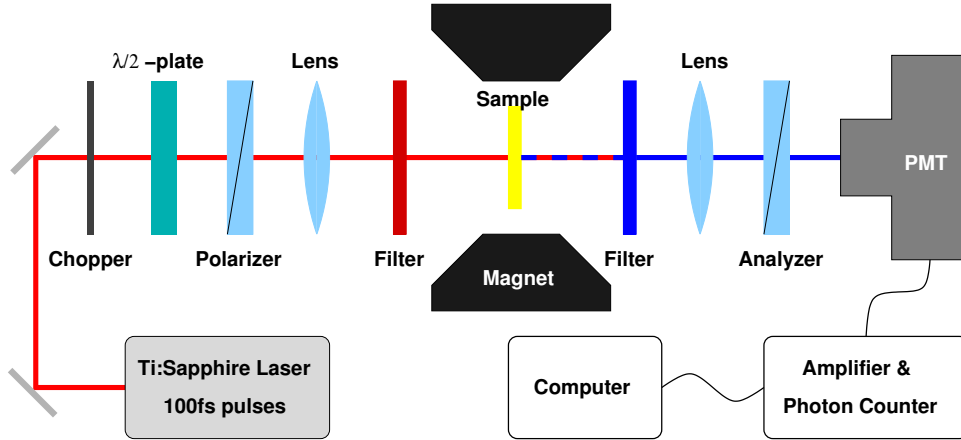


Figure 3.4: Experimental setup for measurement of the MSHG rotational anisotropy in a normal incidence transmission geometry. The magnetic field is applied in the plane of the sample, perpendicular to the incident optical beam.

that only light at the fundamental laser wavelength could reach the sample, an optical filter (RG640) was used to remove any SH light possibly generated in the preceding optical components. The sample was placed on a motorized rotational stage, allowing it to be revolved around an axis normal to the sample plane. For the study of MSHG rotational anisotropy, a magnetic field was applied in the plane of the sample, as shown in Figure 3.4. Immediately after the sample another optical filter (BG39) was used to absorb the fundamental laser wavelength while letting through any SH light generated in the garnet film. This SH light was then focused into a cooled photo multiplier tube (PMT) capable of detecting very low intensities of light. A second polarizer was placed in front of the PMT in order to analyze the polarization of the SHG. Amplifiers and photon counting electronics were used in combination with the PMT to measure the weak SHG signal.

Exposed to an in-plane applied saturating magnetic field \mathbf{H}_{ext} , the sample was rotated in small steps of about $\Delta\phi = 3^\circ$, and the generated SH photons counted for about 5 seconds at each step. This was done for both polarities $\pm\mathbf{H}_{\text{ext}}$ of the applied field. At specific orientations of the sample, also the magnetic field dependence of the SHG signal was recorded. The results of this study and the analysis in terms of the garnet film crystal symmetry are presented in Chapter 5.

3.3 The magneto-optical pump-probe technique

Modern ultrafast laser sources have opened up for experimental access to the picosecond and femtosecond timescales. While most electronic devices cannot measure transients much faster than a nanosecond, techniques that employ ultrashort laser pulses can routinely achieve a time resolution of femtoseconds. Several fundamental processes such as the interaction between electrons, phonons, and magnons in solids take place on the timescale ranging from a few femtoseconds to several nanoseconds, and can conveniently be studied and even controlled using femtosecond pulsed lasers in a pump-probe experimental configuration [27, 28]. Typically, an intense laser pulse (pump) is used to initiate some process of interest, while a time delayed weak pulse (probe) is used to probe the system at some later instant. Repetitive pump-probe cycles with different time delay between the pump and the probe allow for the temporal evolution of the system to be studied directly in the time domain. It is important when using this technique that the repetition rate is slower than the relaxation time of the studied process, so that the same initial condition is restored before every new pump event.

In this section the femtosecond laser system and the pump-probe technique used in Nijmegen for the study of ultrafast magnetization dynamics (Chapter 6) will be described in more detail.

3.3.1 The femtosecond laser and amplifier system

The femtosecond laser system in Nijmegen consists of the following units which are also shown schematically in Figure 3.5:

- Tsunami mode-locked Ti:sapphire laser
- Millennia diode-pumped continuous wave Nd:YVO₄ laser
- Spitfire pulsed Ti:sapphire regenerative amplifier
- Merlin Q-switched intra cavity frequency doubled Nd:YLF laser

The system is capable of delivering a 1-kHz train of ~ 100 fs, $500\mu\text{J}$ pulses, reaching peak powers of approximately 5GW.

The Tsunami mode-locked Ti:sapphire laser from SpectraPhysics was operated at a wavelength of $\lambda = 802\text{nm}$, but is in principle tunable in the range from $\lambda = 710\text{nm}$ to $\lambda = 1050\text{nm}$. Its output pulses have a Gaussian intensity profile and a pulse width (FWHM) of about 60fs. The Tsunami uses an acousto-optic modulator to ensure an 82MHz mode-locked operation. It is pumped by the 5 Watt continuous (CW) output from a Millennia solid state diode-pumped Nd:YVO₄ laser at $\lambda = 532\text{nm}$.

The output from the Tsunami is directed into a SpectraPhysics Spitfire regenerative amplifier which is pumped by the Merlin Q-switched inter-cavity frequency

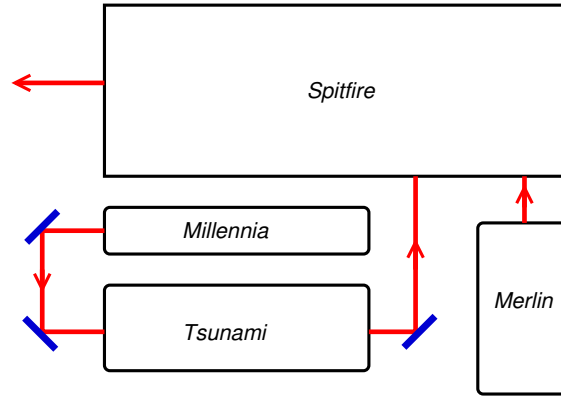


Figure 3.5: The femtosecond laser system composed of a Tsunami Ti:Sapphire laser pumped by a Millennium diode-pumped Nd:YAG laser, and a Spitfire regenerative amplifier pumped by a Merlin Nd:YLF laser and seeded by the 40fs pulses from the Tsunami.

doubled Nd:YLF laser at $\lambda = 527\text{nm}$. The average output power of the pump laser is 10W at a repetition rate of 1kHz, and it delivers 250ns wide pulses. The seeding pulses from the Tsunami are stretched temporally in the Spitfire by a grating-mirror system to avoid damage to the amplifier oscillator by the high peak power in the ultrashort laser pulses. High voltage is applied to a Pockels cell timed to allow the injection of the Tsunami pulse at the same time as a pulse from the Merlin pumps the Ti:Sapphire rod of the amplifier. The lifetime of the Ti:Sapphire excited state is long and the gain induced by the pump is depleted by several round trips of the cavity by the injected pulse. Upon each round trip the pulse is amplified giving an increase in the pulse energy until the majority of the gain is depleted. Additional round trips result in lower pulse energy due to the losses in the cavity being greater than the gain. At the time of maximum depletion of gain from the rod, and thus close to maximum pulse energy, a second Pockels cell is activated and the amplified stretched pulse is ejected from the cavity. This pulse passes through a pulse compressor to regain a pulse width of about 100fs. The energy of the pulses leaving the amplifier is about $500\mu\text{J}$ per pulse and the repetition rate is 1kHz.

3.3.2 Pump-probe experimental setup

The pump-probe experimental setup that was built as part of this Ph.D. work, for the study of laser-induced magnetization dynamics, is shown by the illustration in Figure 3.6. Amplified 100fs laser pulses output from the laser system at a repetition rate of

1kHz are split into two using a beam splitter. The most intense part (about 90% of the intensity), is modulated by a synchronized chopper set to half the frequency of the Spitfire repetition rate. In this way the chopper blocks every second laser pulse and provides alternating pump-on and pump-off conditions in the sample, ideal for a lock-in based detection technique. The polarization of the pump pulses is set by use of a polarizer and a Babinet-Soleil compensator. To avoid damage to the sample, the pump intensity is reduced using neutral density optical filters. When focused to a spot size of about $200\mu\text{m}$, the 100fs laser pulses of energy $20\mu\text{J}$ produce energy flux densities of nearly $2 \cdot 10^{11}\text{W}/\text{cm}^2$, which is about 10^{12} more than the solar irradiance on Earth.

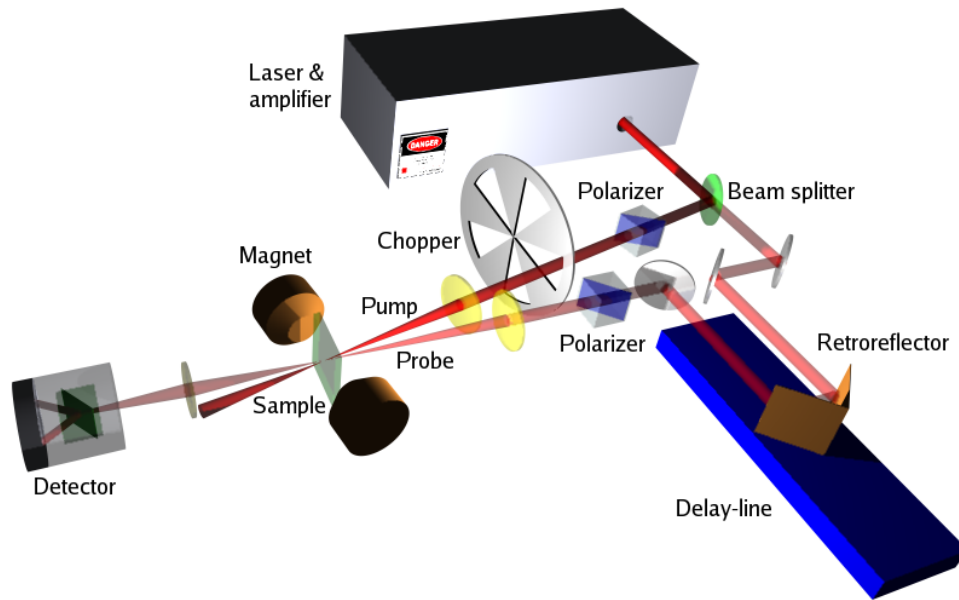


Figure 3.6: Pump-probe experimental setup ⁴. Amplified femtosecond laser pulses are split in two using a beam splitter. A mechanical delay-line is used to vary the distance traveled by the weak probe pulses before reaching the sample. The intense pump pulses are modulated by a synchronized chopper and used to excite a magnetic sample located between the poles of a magnet. The temporal response of the magnetization to the laser excitation can be recorded by scanning the delay line. The magnetization is probed by measuring the Faraday rotation of the probe pulses.

⁴Graphics by C. D. Stanciu

The weaker part of the split laser pulse (10% of the intensity) is further attenuated (so that $I_{\text{pump}}/I_{\text{probe}} > 1000$) using neutral density optical filters and used to probe the state of the sample at a later instant in time. It is important that the probe is weak enough to not influence the processes of interest in the sample. Accurate time-delay of the probe pulse is achieved using a motorized mechanical delay-line, by which the length of the propagation path of the probe pulse can be varied. The current setup has a one meter long delay-line which gives a temporal delay range for the probe beam of about 6ns. The precision with which the delay line retro-reflector can be positioned is $0.1\mu\text{m}$, corresponding to a time resolution of 0.67fs. The probe pulses are focused onto the sample to a slightly smaller spot than the pump and carefully aligned to ensure spatial overlap between the focused pump and probe pulses.

The laser induced changes in the sample magnetization is detected via the magnetooptical Faraday effect. Upon transmission through the sample, the linear polarization of a time-delayed probe pulse rotates an amount proportional to the projection of the local magnetization along the laser pulse k -vector. As the pump-probe time delay is swept, the Faraday angle oscillates and maps out the temporal profile of the spin precession. A balanced photo diode detection scheme is used to measure the probe pulse polarization state. By means of a Wollaston prism the incident light is split into two orthogonally polarized beams I_{\parallel} and I_{\perp} , the intensities of which are monitored by two different photo diodes. The system is carefully balanced so that the intensity initially is equal in the two beams $I_{\parallel} = I_{\perp}$, and small changes in the polarization of the incident light can be detected as a difference in intensity on the two photo-diodes by use of sensitive amplifier electronics.

The intensity I' of linearly polarized light passing through a polarizer with its transmission axis forming an angle ϕ with the incident polarization is

$$I'(\phi) = I_0 \cos^2 \phi, \quad (3.27)$$

where I_0 is the intensity of the incident light. Hence, the intensity on the two photo diodes of the detector is

$$I_{\parallel} = I'(\phi) = I_0 \cos^2 \phi \quad (3.28)$$

$$I_{\perp} = I'(\phi + \frac{\pi}{2}) = I_0 \sin^2 \phi. \quad (3.29)$$

At $\phi = \pi/4$ the detector is balanced ($I_{\parallel} = I_{\perp}$) and the output signal S is proportional to both the probe intensity and the small Faraday rotation δ of the probe pulse:

$$\begin{aligned} S &\propto I_{\parallel}(\frac{\pi}{4} + \delta) - I_{\perp}(\frac{\pi}{4} + \delta) \\ &\propto I_0 \left[\cos^2(\frac{\pi}{4} + \delta) - \sin^2(\frac{\pi}{4} + \delta) \right] \\ &\propto I_0 \cos(\frac{\pi}{2} + 2\delta) \\ &\propto 2I_0\delta. \end{aligned} \quad (3.30)$$

The response of the detector to a femtosecond laser pulse is significantly broadened (to about $25\mu\text{s}$) due to the limited bandwidth of the photo-diode and amplifier electronics. However, the detector output still constitutes only a tiny fraction of the 1ms time between two probe pulses. In cases like this, boxcar integration can be used to improve the signal-to-noise ratio by recording the voltage only when the signal is present, and ignoring time periods when there is no signal and only noise. In the present setup, the $\sim 25\mu\text{s}$ output from the differential photo detector is integrated by a SR250 gated integrator and boxcar averager from Stanford Research, triggered by the 1kHz frequency of the Spitfire and set to integrate over a window of $15\mu\text{s}$. By use of a sample-and-hold circuit, the integration result is output for a duration of 1ms until the next trigger pulse. Due to the synchronized chopper which blocks every second pump pulse, only every second probe pulse is preceded by a pump event that excites the magnetic sample. Consequently, the amplitude of the 500Hz output signal from the boxcar integration is a direct measure of the pump-induced change to the sample magnetization. The signal is fed to a Lock-in amplifier referenced by the 500Hz frequency from the chopper and averaged over several excitation events.

Not only the magnetic properties of the sample are influenced by the intense laser pump pulses, but also its optical properties $\epsilon = \epsilon_r + i\epsilon_i$ (see Section 3.1 and Chapter 4) may be temporarily modified. This can cause a change in the sample reflectivity and transmittivity which also affects the transmitted probe intensity I_0 . Note that the signal S from the balanced diode detector is directly proportional to the intensity I_0 of the probe pulses (Eq. 3.30), and that S therefore will be sensitive to pump-induced optical effects. In order to eliminate this artifact and to separate optical effects from the true magnetooptical signal, the response I_{\parallel} and I_{\perp} of the individual photo diodes was recorded in addition to the differential signal S . A simultaneous decrease or increase in I_{\parallel} and I_{\perp} can be ascribed to purely optical pump-induced effects. Additional boxcar integrators and lock-in amplifiers were used for the detection of the single diode response.

In the above described experimental setup the linear magnetooptical Faraday effect was used to probe the temporal behavior of the magnetization. However, this approach is not applicable to all magnetic materials. For opaque samples the MO Kerr effect can be used in a similar way to probe the magnetization, and in order to achieve interface sensitivity nonlinear magnetooptical effects such as MSHG can be employed (see Section 3.2). With this latter technique, also the dynamics of the magnetic order-parameter in antiferromagnets can be probed.

References

- [1] G. E. Jellison, Thin Sol. Films **234**, 416 (1993).
- [2] H. Tompkins and E. Irene, eds., *Handbook of Ellipsometry* (William Andrew Publishing, 2005).
- [3] D. E. Aspnes and A. A. Studna, **14**, 220 (1975).
- [4] J. Opsal, J. Fanton, J. Chen, J. Leng, L. Wei, C. Uhrich, M. Senko, C. Zaiser, and D. E. Aspnes, Thin Sol. Films **313**, 58 (1998).
- [5] M. Schubert, Thin Sol. Films **313-314**, 323 (1998).
- [6] R. M. A. Azzam and N. M. Bashara, *Ellipsometry and polarized light*, North-Holland personal library (North-Holland Publishing Company, Amsterdam, 1987), 2nd ed.
- [7] B. Drevillon, Thin Sol. Films **313**, 625 (1998).
- [8] E. Garcia-Caurel, J. L. Moncel, F. Bos, and B. Drevillon, Rev. Sci. Instr. **73**, 4307 (2002).
- [9] D. E. Aspnes, J. Opt. Soc. Am. **64**, 639 (1975).
- [10] D. E. Aspnes, J. Opt. Soc. Am. **64**, 812 (1973).
- [11] M. Schubert, Phys. Rev. B **53**, 4265 (1996).
- [12] M. Mansuripur, *The Physical Principles of Magneto-optical Recording* (Cambridge University Press, Cambridge, 1995).
- [13] M. Schubert, T. E. Tiwald, and J. A. Woollam, **38**, 177 (1999).
- [14] D. E. Aspnes and A. A. Studna, Phys. Rev. B **20**, 3292 (1979).
- [15] O. Polgár, M. Fried, T. Lohner, and I. Bársony, Surf. Sci. **457**, 157 (2000).
- [16] T. Brabec and F. Krausz, Rev. Mod. Phys. **72**, 545 (2000).
- [17] Y. R. Shen, Surf. Sci. **299**, 551 (1994).
- [18] Y. R. Shen, *The Principles of Nonlinear Optics* (Wiley, New York, 1984).
- [19] K. H. Bennemann, *Nonlinear Optics in Metals*, International series of monographs on physics (Oxford Clarendon Press, 1998).
- [20] H. Wierenga, Ph.D. thesis, University of Nijmegen (1995).

- [21] A. Kirilyuk, J. Phys. D **35**, R189 (2002).
- [22] A. Kirilyuk and Th. Rasing, J. Opt. Soc. Am. B **22**, 148 (2005).
- [23] M. Fiebig, V. V. Pavlov, and R. V. Pisarev, J. Opt. Soc. Am. B **22**, 96 (2005).
- [24] R. R. Birss, *Symmetry and Magnetism*, Series of monographs on selected topics in solid state physics (North-Holland Publishing Company, Amsterdam, 1966), 2nd ed.
- [25] M. Born and E. Wolf, *Principles of Optics* (Cambridge University Press, 1998), 6th ed.
- [26] R. Stolle, K. J. Veenstra, F. Manders, Th. Rasing, H. van den Berg, and N. Persat, Phys. Rev. B **55**, R4925 (1997).
- [27] K. H. Bennemann, J. Phys.: Condens. Matter **16**, R995 (2004).
- [28] J. Shah, *Ultrafast Spectroscopy of Semiconductors and Semiconductor Nanostructures*, Springer Series in Solid-State Sciences (Springer, 1999), 2nd ed., ISBN 3-540-64226-9.

CHAPTER 4

Ellipsometry studies of the linear optical and magneto-optical properties of Bi substituted iron garnet films ¹

Abstract

A series of iron garnet films of composition $\text{Lu}_{3-x}\text{Bi}_x\text{Fe}_{5-y}\text{Ga}_y\text{O}_{12}$ grown on (001) oriented GGG substrates have been studied using variable angle spectroscopic ellipsometry and polar Kerr spectroscopy (spectroscopic MOKE). The diagonal and off-diagonal components of the permittivity tensor have been determined in the range 1-5eV. Our results are in accordance with previously reported measurements on similar systems. We find that the optical absorption is reduced as the gallium content is increased. With increased Ga doping we also see an increase in the real part of ϵ_0 above 3.7eV, but a decrease for lower energies. In the spectra of the off-diagonal permittivity tensor components we observe bismuth enhancement and gallium dilution effects.

4.1 Introduction

Garnets have been studied extensively for about 50 years, but still not all aspects of these materials are fully understood. In particular the transitions responsible for

¹Adapted from F. Hansteen, L.E. Helseth, T.H. Johansen, O. Hunderi, A. Kirilyuk, and Th. Rasing *Thin Sol. Films* **455-456C**, 429-432 (2004).

their optical and strong magneto-optical response are still a matter of debate [1, 2, 3]. A detailed theoretical understanding and accurate experimental results are needed in order to gain further insight into the microscopic physics of these materials.

Previous experimental studies of the optical spectra of garnets have mainly been based on reflectivity measurements and Kramers-Kronig analysis to obtain the diagonal components of the permittivity tensor [4, 5]. Ellipsometry is a more reliable and very sensitive technique which can accurately measure the optical properties of materials, however, it also relies on careful modeling of the system under study and fitting of experimental data in order to obtain optical constants (see Section 3.1).

We have studied a series of 2.5-4 μ m thick garnet films of composition

$$\text{Lu}_{3-x}\text{Bi}_x\text{Fe}_{5-y}\text{Ga}_y\text{O}_{12}$$

using variable angle spectroscopic ellipsometry and spectroscopic MOKE. For three selected samples the diagonal and off-diagonal permittivity tensor components in the energy range 1-5eV have been determined.

The permittivity tensor is commonly used as the link between experimental results and microscopic theory of materials. The linear optical response of our garnet films can be described by a permittivity tensor of the form

$$\epsilon = \begin{pmatrix} \epsilon_0 & i\epsilon_1 & 0 \\ -i\epsilon_1 & \epsilon_0 & 0 \\ 0 & 0 & \epsilon_0 \end{pmatrix} \quad (4.1)$$

when the magnetization is in the z -direction (polar configuration). For an absorbing medium the tensor components are complex and given by $\epsilon_j = \epsilon'_j + i\epsilon''_j$. To the first order in the magnetization the diagonal component ϵ_0 is independent of \mathbf{M} . The off-diagonal component ϵ_1 is linear in \mathbf{M} and gives rise to magneto-optical effects. At normal incidence the Kerr rotation θ_K and ellipticity η_K of a semi-infinite medium are related to the components of the permittivity tensor through the relation [6]

$$\Phi_K = \theta_K + i\eta_K = \frac{-i\epsilon_1}{\sqrt{\epsilon_0}(\epsilon_0 - 1)}. \quad (4.2)$$

For more complex systems such as thin films or multilayer structures, no simple relation exists, and numerical fitting of measurements to model calculations should be employed in order to determine off-diagonal tensor elements from Kerr measurements and knowledge of ϵ_0 .

4.2 Experimental procedure

The series of garnet films under study have in-plane magnetization and were grown by LPE on (001) oriented gadolinium gallium garnet (GGG) substrates for the purpose

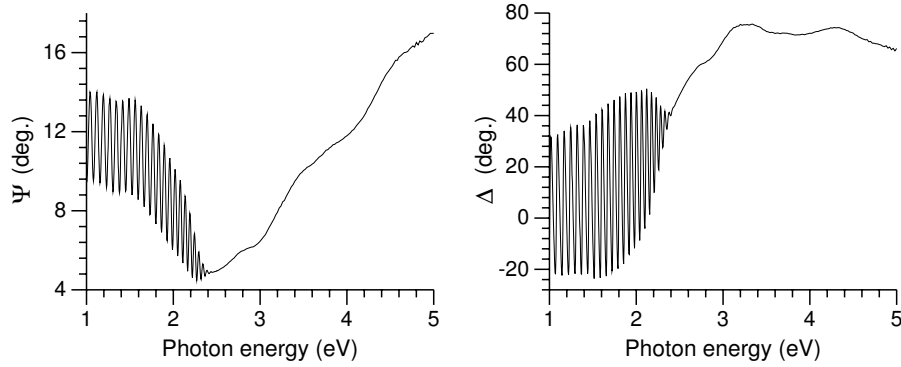


Figure 4.1: Measured ellipsometric quantities Ψ and Δ at 70° incidence for an approximately $4 \mu\text{m}$ thick garnet film of composition $\text{Lu}_{2.3}\text{Bi}_{0.7}\text{Fe}_{4.4}\text{Ga}_{0.6}\text{O}_{12}$. Strong interference oscillations can be seen in the low energy part of the spectrum where the film is transparent.

of magneto-optical imaging. They are transparent in the near infrared and visible spectral region up to about 2.3eV.

The samples were measured at three angles of incidence, 67° , 70° , and 73° , at photon energies ranging from 1 to 5eV. The measured ellipsometric quantities Ψ and Δ were then fitted to a model (see Fig. 4.2) consisting of a GGG substrate, a film layer of unknown thickness and unknown optical constants, and a surface roughness layer (effective medium [7] layer consisting of a 50% mixture of the previous layer and empty space). The garnet film thicknesses had previously been measured using scanning electron microscopy (SEM), and these values were taken as the starting point for the fitting procedure.

Below approximately 2.3eV the absorption of the garnet films drops markedly and they become transparent, leading to strong interference oscillations in the measurements as shown in Figure 4.1. In this low energy range of the spectrum a Cauchy dispersion model ($n = A + B\lambda^{-2}$) with exponential (Urbach) absorption was used to represent the optical constants of the film [8]. After obtaining a good fit for the film thickness, surface roughness, and the parameters of the Cauchy model in this spectral region, the thickness of the garnet film and the surface roughness layer were held fixed, and ϵ'_0 and ϵ''_0 fit for every measurement point. Some results of the fitting procedure are summarized in Table 4.1.

Kerr rotation and ellipticity were also measured using the ellipsometer at 15° incidence. The samples were mounted on top of a permanent magnet giving a field of 250kA/m at the film surface, enough to saturate their magnetization in the out-of-

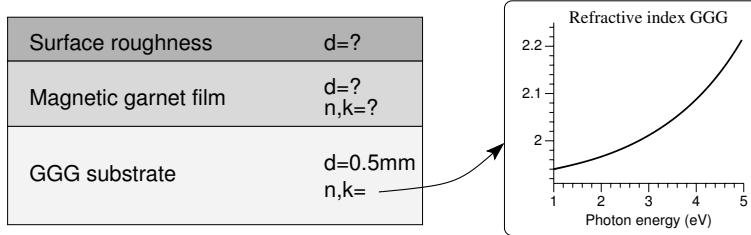


Figure 4.2: Model used for fitting of ellipsometry measurements. Reference data is used for the dielectric function of the GGG substrate, while the thickness, optical properties and surface roughness of the magnetic garnet film are unknown parameters.

Table 4.1: Composition and properties of the garnet samples; film thickness d_{SEM} determined by SEM, film thickness d_{elli} and surface roughness layer thicknesses d_{rough} found by fitting ellipsometry data.

Composition	d_{SEM} (μm)	d_{elli} (nm)	d_{rough} (nm)
$\text{Lu}_{2.5}\text{Bi}_{0.5}\text{Fe}_5\text{O}_{12}$	3.0	2798	6.6
$\text{Lu}_{2.3}\text{Bi}_{0.7}\text{Fe}_{4.7}\text{Ga}_{0.3}\text{O}_{12}$	3.5	3460	4.6
$\text{Lu}_{2.3}\text{Bi}_{0.7}\text{Fe}_{4.4}\text{Ga}_{0.6}\text{O}_{12}$	4.0	3915	7.3

plane direction. Measurements were made with the magnetic field in both directions, and the average results used in order to eliminate any offset. The acquired data was again fit to a model to obtain the off-diagonal tensor components. The model was essentially the same as previously described, only modified to include the magneto-optical response of the film.

In addition to the ellipsometric Kerr measurements, a home built photoelastic modulator based setup (also spectroscopic), similar to that described by Sato [9], was used to verify the results. The sensitivity of this system is greater than that of the ellipsometer, but for our films the ellipsometer proved sufficient. In the absorbing region of the spectrum Eq. (4.2) can be used to directly estimate the off-diagonal elements, neglecting the small angle of incidence and surface roughness effects.

4.3 Results and discussion

Bismuth substitution is known to increase the refractive index of garnets in the low energy region of the spectrum and to increase the absorption [5, 10]. Gallium, on

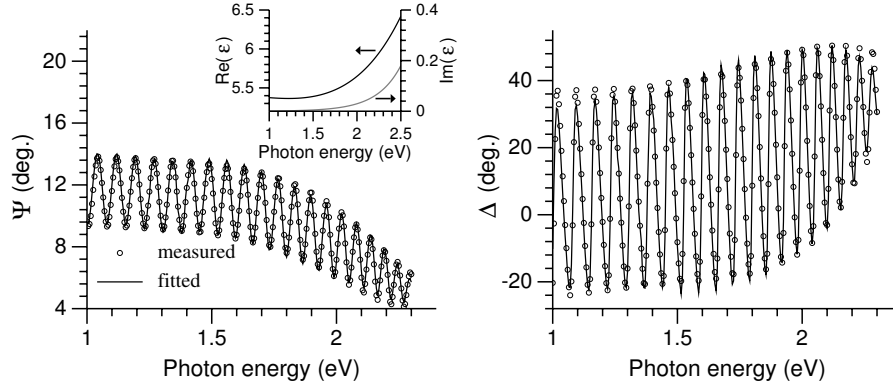


Figure 4.3: Measured and fitted Ψ and Δ at 70° incidence in the low energy part of the spectrum for one of the samples. The inset shows the dielectric function obtained by fitting to a Cauchy type dispersion model. A very good simultaneous fit for the measurements at 67° , 70° and 73° incidence is achieved. Shown here is only the fit for 70° .

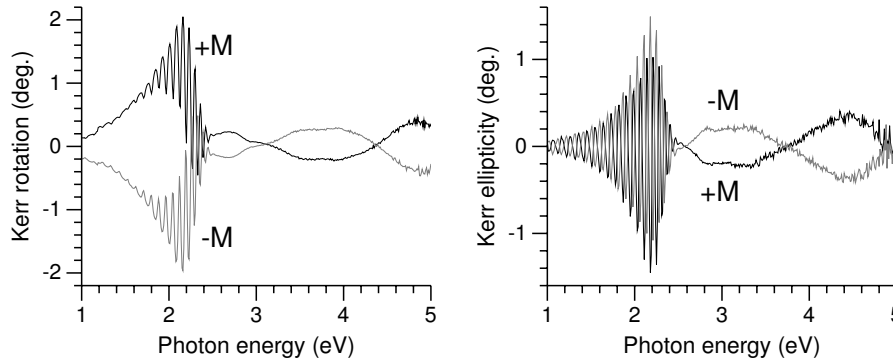


Figure 4.4: Measured Kerr rotation and ellipticity using the ellipsometer at 15° incidence, for the sample with composition $\text{Lu}_{2.3}\text{Bi}_{0.7}\text{Fe}_{4.4}\text{Ga}_{0.6}\text{O}_{12}$. Strong interference oscillations can be seen in the transparent low energy part of the spectrum. The increased signal noise at about 5eV is due to the lower intensity of UV light from the ellipsometer's broadband Xe arc lamp.

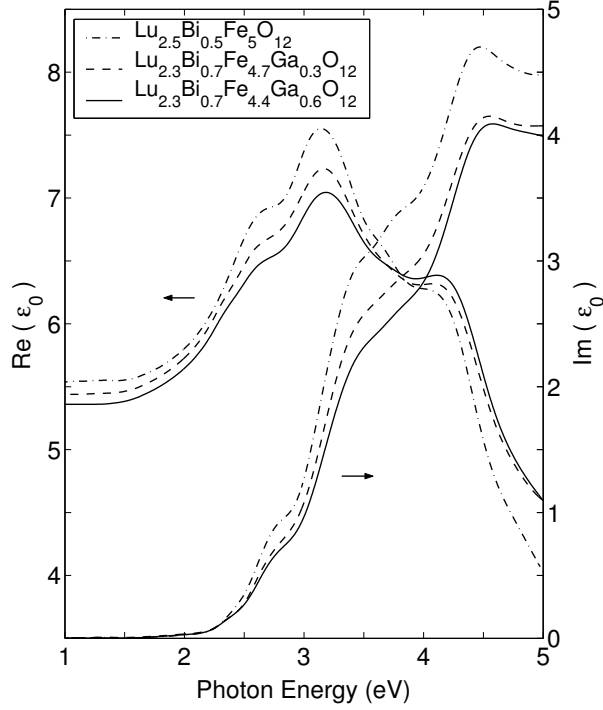


Figure 4.5: Diagonal components ϵ_0 of the permittivity tensor for three garnet films of different composition. Gallium substitution significantly reduces the optical absorption. The real part of ϵ_0 shows a decrease at low energies but an increase above 3.7eV for the samples with higher Bi and Ga concentrations.

the other hand, substitutes the active iron ions at tetrahedral and octahedral sites, and is expected to reduce optical absorption as well as magneto-optical effects. Ga^{3+} substitutes preferentially for tetrahedrally coordinated Fe^{3+} (approximately 90%) and permits thereby in principle for discrimination between the spectral contribution of octahedral and tetrahedral Fe^{3+} [4, 11].

The real and imaginary parts of the diagonal permittivity tensor components for our three samples are shown in Fig. 4.5. Absorption, essentially due to ϵ''_0 , can be seen to decrease noticeably for the two samples with higher bismuth ($x = 0.7$) and gallium ($y = 0.3, y = 0.6$) concentration. Furthermore, increased gallium substitution seems to reduce ϵ'_0 in the low energy part of the spectrum but leading to an increase above 3.7eV. These observations must mainly be attributed to the increase in gallium

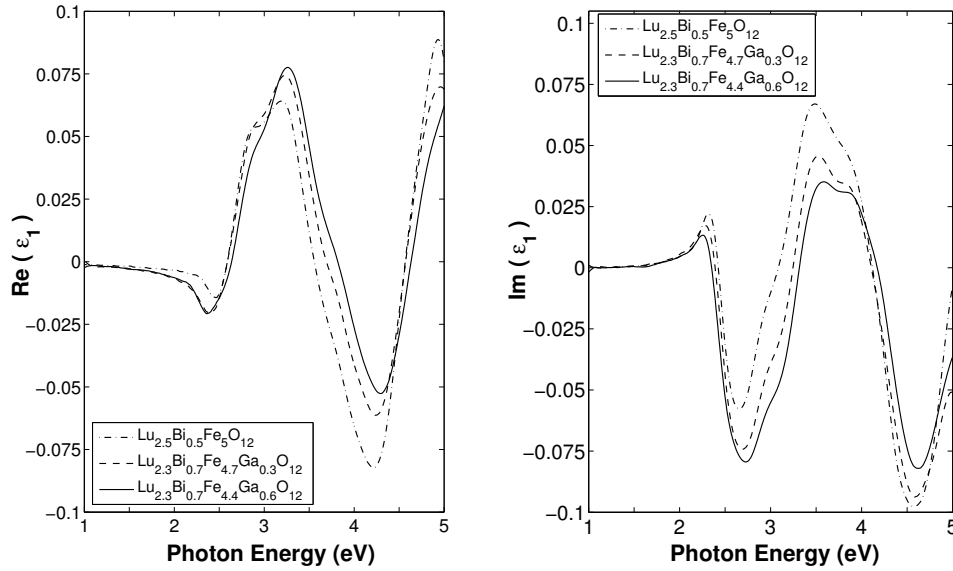


Figure 4.6: Real and imaginary parts of the off-diagonal tensor element ϵ_1 . Enhancement due to bismuth substitution can be seen in $\text{Re}\{\epsilon_1\}$ below 2.5eV and for the peak at 3.2eV, and in $\text{Im}\{\epsilon_1\}$ for the peak at 2.7eV. Dilution effects of gallium are observed in $\text{Re}\{\epsilon_1\}$ at the 4.2eV peak, and in $\text{Im}\{\epsilon_1\}$ for the peaks at 2.3eV, 3.5eV and 4.6eV.

concentration, and indicate that the effect of diluting the Fe^{3+} lattice is greater than the effect of added bismuth.

Bismuth substitution of garnets is well known to enhance magneto-optical effects, while gallium is known to reduce the effects for reasons just mentioned. The real and imaginary parts of ϵ_1 found from our measurements are shown in Fig. 4.6. Some peaks clearly show the expected dilutive effect of gallium, such as the peaks in ϵ_1'' at 2.3eV, 3.5eV and 4.6eV and in ϵ_1' at 4.2eV. Enhancement due to increased bismuth concentration can be observed in the low energy region of ϵ_1' , for the peak at 3.2eV, and for the peak in ϵ_1'' at 2.7eV. Here gallium dilution seems to have no effect, or in fact the opposite of the expected effect. There also appears to be a pronounced red-shift of the 2.4eV peak in ϵ_1' and a blue-shift at 4.2eV for $y = 0.3$ and $y = 0.6$. Fitting ϵ_1' and ϵ_1'' in terms of electric-dipole transitions, like several authors have attempted [2, 5, 12, 13, 14], might provide a better understanding of these spectra and the effect of Bi and Ga on the transitions involved. Such a fitting should, however, be based on reliable knowledge of the positions and character of the relevant transitions. Without this information the fitting is not unique, and does not further contribute to

the understanding of these materials.

The model used to invert the ellipsometry data assumes that the garnet film is homogeneous and that ϵ_0 does not vary through the film. This assumption may not hold completely true, as indicated by magnetization induced second harmonic generation (MSHG) studies of the same samples. This technique, that has a particular sensitivity to symmetry breaking surfaces and interfaces [15], shows a difference in crystal symmetry for the signal originating from the film surface and interface. To what extent this has an influence on the linear optical and magneto-optical properties is not known.

4.4 Conclusions

We have experimentally determined the spectra of the permittivity tensor components ϵ_0 and ϵ_1 in the range 1-5eV for three lutetium iron garnet films doped with gallium and bismuth. There is clearly an influence of the film composition on both ϵ_0 and ϵ_1 , however, this is not always simply an enhancement (in the case of bismuth) or reduction (in the case of gallium) of the spectral features throughout the whole spectrum. Theoretical fitting of these spectra is necessary to gain further insight into the microscopic physics of these materials.

References

- [1] A. Zenkov and A. Moskvina, J. Phys.: Condens. Matter **14**, 6957 (2002).
- [2] G. A. Allen and G. F. Dionne, J. Appl. Phys. **93**, 6951 (2003).
- [3] G. F. Dionne and G. A. Allen, J. Appl. Phys. **95**, 7333 (2004).
- [4] F. J. Kahn, P. Pershan, and J. Remeika, Phys. Rev. **186**, 891 (1969).
- [5] S. Wittekoek, T. J. A. Popma, J. M. Robertson, and P. F. Bongers, Phys. Rev. B **12**, 2777 (1975).
- [6] A. Zvezdin and V. Kotov, *Modern Magneto-optics and Magneto-optical Materials* (IOP Publishing Ltd., 1997).
- [7] D. E. Aspnes, Thin Sol. Films **89**, 249 (1982).
- [8] M. Born and E. Wolf, *Principles of optics* (Cambridge University Press, 1998), 6th ed.
- [9] K. Sato, Jpn. J. Appl. Phys. **20**, 2403 (1981).
- [10] P. Hansen, C.-P. Klages, J. Schuldt, and K. Witter, Phys. Rev. B **31**, 5858 (1985).

-
- [11] G. Scott, D. Lacklison, and J. Page, J. Phys. C **8**, 519 (1975).
 - [12] Z. Šimša, H. Le Gall, J. Šimšová, J. Koláček, and A. L. Paillier-Malécot, IEEE Trans. Magn. **20**, 1001 (1984).
 - [13] G. F. Dionne and G. A. Allen, J. Appl. Phys. **73**, 6127 (1993).
 - [14] L. Helseth, R. Hansen, E. Il'yashenko, M. Baziljevich, and T. Johansen, Phys. Rev. B **64**, 174406 (2001).
 - [15] Th. Rasing, *Nonlinear Optics in Metals* (Clarendon Press, Oxford, 1998, K.H. Bennemann, ed.), chap. 3, International series of monographs on physics.

CHAPTER 5

Selective surface/interface characterization of thin garnet films by Magnetization-induced Second-Harmonic Generation ¹

Abstract

Magnetization-induced second-harmonic generation (MSHG) has been used for the study of thin garnet films. The strong optical absorption of these films at the second harmonic frequency provides a unique possibility to study magnetic and structural properties of the film surface and film/substrate interface separately. When studied in transmission at normal incidence all relevant elements of the crystallographic part of the nonlinear optical susceptibility tensor vanish identically, while a magnetization-induced contribution remains. The purely magnetic origin of SHG from the interface is unambiguously demonstrated. From measurements of the SHG rotational anisotropy and magnetic field dependence, the surface is found to have inclusions which act as nonmagnetic sources of SHG, while the anisotropy causing easy in-plane magnetization is found to be stronger at the interface with the substrate than at the surface of the film.

¹Adapted from F. Hansteen, O. Hunderi, T.H. Johansen, A. Kirilyuk, and Th. Rasing *Phys. Rev. B* **70**, 094408 (2004), and F. Hansteen, O. Hunderi, T.H. Johansen, A. Kirilyuk, and Th. Rasing *Trans. Magn. Soc. Jpn.* **4**, 318-321 (2004).

5.1 Introduction

Recently there has been significant interest in thin garnet films as sensors and indicators for magnetic fields. Garnet films with in-plane magnetization have been found to be exceptionally well suited for magnetic field visualization and imaging. Very little domain activity and a continuous rotation of the magnetization vector in response to an increasing external field are some of their favorable properties. Films of this type have successfully been used for imaging magnetic domains, recorded patterns in magnetic storage media, currents in microelectronic circuits, and for the study of defects, currents, and vortices in superconductors [1, 2, 3].

For imaging applications it is particularly important to have high quality, uniform, single-domain films with high sensitivity and little defects. These are properties which can be tailored to a large degree by substitution and by tuning of the growth conditions. It is, for instance, well known that Bismuth-substitution on dodecahedral sites of the garnet crystal strongly enhances the linear magnetooptical response. Furthermore, the film and substrate compositions influence the lattice matching at the interface. A small mismatch will cause strain in the grown film, while larger values of the lattice mismatch may, in addition, cause growth of differently oriented crystallites, defects in the crystal structure, or even cracking of the film or substrate. Moderate mismatch is sometimes deliberately introduced in order to obtain the desired magnetic anisotropy and easy direction of magnetization. For garnet films grown on (001) oriented gadolinium gallium garnet (GGG) substrates the strain is uniaxial, and will, depending on the sign of the anisotropy constant, strive to align the spontaneous magnetization either along the anisotropy axis (easy-axis) or normal to this axis (easy-plane). The dominant factor in deciding the easy direction of magnetization will, however, often be the shape anisotropy.

The sensitivity of the MO response of garnet films to an external field is one of the main properties of interest for imaging applications. It is commonly investigated by measuring the external field dependence of the Faraday rotation in the spectral region of interest. This, however, reflects only averaged bulk properties of the film without addressing the possibility that there could be a significant inhomogeneity across the thickness of the film. Relaxation of interfacial strain due to lattice mismatch may cause different anisotropy fields and thus different MO sensitivity for the film surface and interface regions. A technique that is sensitive to magnetization and capable of distinguishing between the surface and the interface is needed in order to study these effects.

As discussed in Section 3.2, magnetization induced second harmonic generation is a nonlinear optical technique which has the desired sensitivity to magnetic surfaces and interfaces [4, 5, 6, 7, 8, 9, 10, 11]. This chapter describes an experimental study of SHG in garnet films with in-plane magnetization, grown for the purpose of MO imaging by liquid phase epitaxy on (001) oriented substrates. The experimental geometry was

chosen so that crystallographic contributions to the SHG vanish completely, leaving only magnetization-induced SHG. Despite the broken space inversion symmetry in these films, the surface and interface regions may be studied independently. This is made possible by a strong optical absorption in the films at the second harmonic frequency, leading to a escape depth of about $0.2 \mu\text{m}$ for light at 2ω ($\lambda = 400\text{nm}$), and provides a very powerful tool for the characterization of the interfaces of these materials.

5.2 Results and discussion

As discussed in Section 3.2, the induced polarization \mathbf{P} in a medium due to an incident electromagnetic wave \mathbf{E} can be written in the electric dipole approximation as an expansion in powers of the electric field of the incident wave (see Eq. 3.21). In a local frame of reference (see Fig. 5.1), the polarization at frequency 2ω induced by the incident field e at frequency ω in a medium with static magnetization m can be written as:

$$p_i^{2\omega} = \chi_{ijk}^{(cr)} e_j^\omega e_k^\omega + \chi_{ijkl}^{(m)} e_j^\omega e_k^\omega m_l, \quad (5.1)$$

where $\{i, j, k, l\} = \{x, y, z\}$. The third rank polar tensor $\chi_{ijk}^{(cr)}$ represents the crystallographic contribution, and the fourth rank axial tensor $\chi_{ijkl}^{(m)}$ represents the magnetization induced contribution. The observable intensity of radiated light at the second harmonic frequency is given by the square of the induced polarization at 2ω [12]

$$\begin{aligned} I(2\omega) &\propto |\mathbf{P}(2\omega)|^2 \propto |\chi^{(cr)} + \chi^{(m)}|^2 \\ &\propto |\chi^{(cr)}|^2 + |\chi^{(m)}|^2 + 2|\chi^{(cr)}||\chi^{(m)}| \cos \Delta\Phi. \end{aligned} \quad (5.2)$$

Bulk garnet crystals have cubic symmetry and are centrosymmetric, thereby limiting any SHG to a very thin region near the surface or interface where the space inversion symmetry is broken. In thin garnet films, however, the inversion symmetry appears to be broken [13, 14, 15] due to what might be a growth induced distortion of the symmetry along the direction of growth. This reduces the symmetry of our thin (001) oriented film to the tetragonal $4mm$ point group, and allows for crystallographic bulk contributions to the SHG. In the presence of a magnetization that causes breaking of the time-inversion symmetry, also magnetization-induced contributions from the bulk will be allowed.

Now, consider a crystalline magnetic thin film of point group symmetry $4mm$ illuminated at normal incidence along the z -direction, and exposed to an in-plane magnetic field, as shown in Fig. 5.1. In this geometry, all elements of $\chi^{(cr)}$, the crystallographic part of the second order susceptibility tensor in Eq. (5.1), vanish

identically, while the nonzero components of $\chi_{ijkl}^{(m)}$ are [13, 16]

$$\begin{aligned} A &= \chi_{xxxy} = -\chi_{yyyx}, \\ B &= \chi_{xxyx} = \chi_{xyxx} = -\chi_{xyyy} = -\chi_{yyxy}, \\ C &= \chi_{yxxx} = -\chi_{yyyy}. \end{aligned} \quad (5.3)$$

Both crystal symmetry and experimental geometry determine which tensor components contribute to the observable SHG signal. At non-normal incidence also crystallographic contributions would be present for media belonging to the $4mm$ point group.

When the crystalline film is rotated an angle ϕ about the Z -axis and exposed to a stationary magnetic field along the Y -axis, the induced polarization at frequency 2ω in the stationary XYZ frame of reference can readily be deduced.

$$P_{XX} = ME_X^2 \frac{\epsilon_0}{4} [(3A - 2B - C) + (A + 2B + C) \cos 4\phi] \quad (5.4)$$

$$P_{XY} = ME_X^2 \frac{\epsilon_0}{4} [(A + 2B + C) \sin 4\phi] \quad (5.5)$$

$$P_{YX} = ME_Y^2 \frac{\epsilon_0}{4} [(A + 2B - 3C) - (A + 2B + C) \cos 4\phi] \quad (5.6)$$

$$P_{YY} = -ME_Y^2 \frac{\epsilon_0}{4} [(A + 2B + C) \sin 4\phi]. \quad (5.7)$$

P_{IJ} denotes the induced polarization along the J direction due to an incident wave polarized along the I direction.

For the case of $4mm$ symmetry, as can be seen from Eqs. (5.4)-(5.7) and (5.2), the radiated intensity $I(2\omega)$ is quadratic in \mathbf{M} , and is therefore not expected to change upon reversal of the direction of the magnetization, $\mathbf{M} \rightarrow -\mathbf{M}$.

If the aforementioned experimental geometry is modified to magnetize the films in the out-of-plane Z -direction, then also $\chi^{(m)} \equiv 0$ for symmetry reasons and no SHG will take place.

An approximately $3 \mu\text{m}$ thick garnet film of composition $\text{Lu}_{2.5}\text{Bi}_{0.5}\text{Fe}_5\text{O}_{12}$, grown on a (001) oriented gadolinium gallium garnet (GGG) substrate was illuminated at normal incidence by femtosecond laser pulses of $\lambda = 840 \text{ nm}$ generated by a Ti:Sapphire laser system. The incident beam was focused to a spot size of approximately $200 \mu\text{m}$ on the sample, which was exposed to a magnetic field in the Y -direction, as shown in Fig. 5.1. The transmitted second harmonic intensity was detected using a standard photon counting technique involving a cooled photomultiplier tube (PMT), an amplifier, and counting electronics. The spontaneously in-plane magnetized garnet film was exposed to a stationary magnetic field to keep the magnetization fixed along the Y -axis as the sample was rotated.

The polarization of the incident wave was set using a Babinet-Soleil compensator followed by a Glan-Taylor polarizer. An edge filter (RG640) was used to exclude the

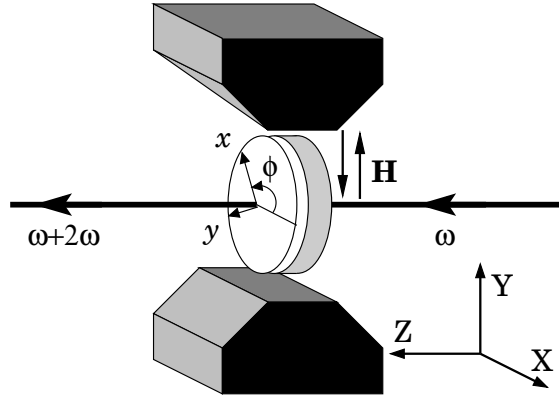


Figure 5.1: Experimental setup. The sample, a thin garnet film on a GGG substrate, is illuminated by femtosecond laser pulses and rotated about an axis normal to the film plane in a magnetic field along the $\pm Y$ -direction. The angle ϕ denotes the rotation of the sample's x -axis with respect to the X -axis of the laboratory system of reference.

possibility of SH light generated in any of the optical components reaching the sample and influencing the measurements. Similarly, a band-pass filter (BG39) was placed immediately after the sample to filter out the strong fundamental beam. An additional filter was used to absorb the strong two-photon luminescence at $\lambda = 520 - 560$ nm exhibited by the samples under study. An analyzer, also of the Glan-Taylor type, was placed before the photomultiplier and used to determine the polarization of the SH light.

Rotational anisotropy measurements of the SHG were made by recording the intensity of light at 2ω as a function of the sample angle of rotation ϕ about an axis normal to the film plane. This was done for light incident both from the film and substrate side of the sample and for different combinations of polarizer and analyzer settings.

The GGG material used as a substrate is essentially transparent both to the fundamental beam at $\lambda = 840$ nm and to the second harmonic [17]. The magnetic garnet film also exhibits low linear optical absorption at the fundamental wavelength, but has a very strong absorption at the second harmonic frequency of about $\alpha = 5 \times 10^4 \text{ cm}^{-1}$ ($\epsilon \approx 7 + i$). The linear optical properties of a series of garnet films, the ones studied here included, have previously been obtained from ellipsometric measurements [18]. The strong absorption of the second harmonic wave makes it possible to study the film surface and interface separately by illuminating it from either the substrate or surface side, respectively. Since the escape depth of light at

2ω is approximately $0.2 \mu\text{m}$, only a layer of this thickness contributes to the signal observed in transmission.

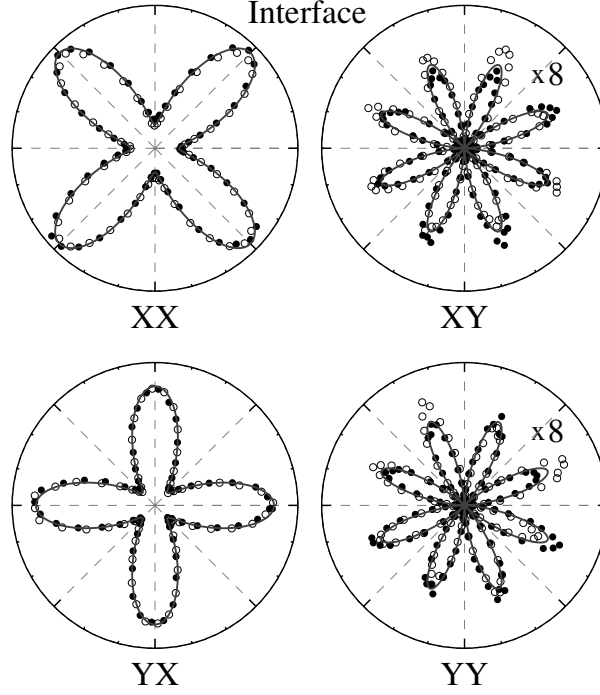


Figure 5.2: Polar plots of the measured SHG rotational anisotropy $I(\phi)$ originating from the film-substrate interface for a full 360° azimuthal rotation of the sample in an in-plane magnetic field. The symbols $\{X, Y\}$ below each plot denote the settings of polarizer and analyzer transmission axis, respectively. Open and filled circles represent measurements with the magnetic field in the $+Y$ and $-Y$ direction. The solid lines represent best fits to the data points.

The observed SH intensity from the film-substrate interface as a function of the azimuthal angle of the sample is shown in Fig. 5.2 for a full 360° rotation, and for four different combinations of polarizer and analyzer settings. The filled and empty points correspond to measurements at $\pm \mathbf{M}$. The solid lines represent best fits to the data points using Eqs. (5.4)-(5.7). The obtained best fit parameters, normalized to $A(\text{interface}) = 1$, are listed in Table 5.1. A very good fit is obtained, and no dependence on the direction of magnetization is observed, in agreement with the expected quadratic \mathbf{M} dependence of $I(2\omega)$. The XX and YX curves show a

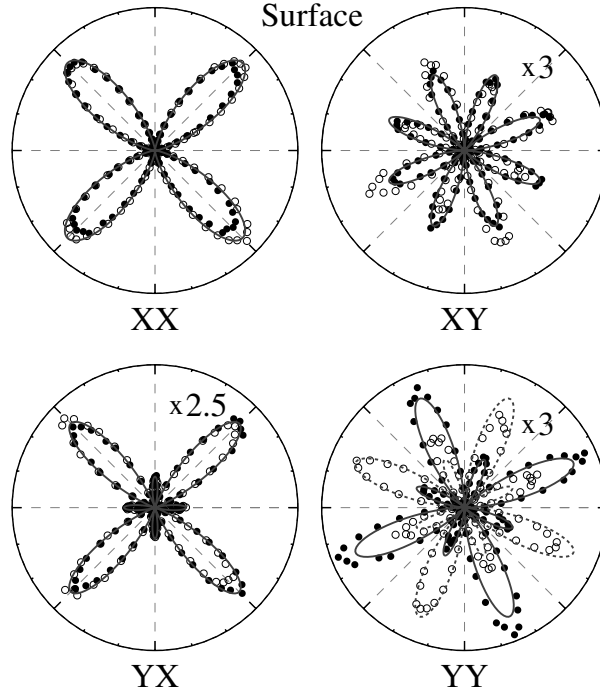


Figure 5.3: Measured SHG rotational anisotropy $I(\phi)$ originating from the garnet film surface. The symbols below each plot denote the settings of polarizer and analyzer transmission axis, respectively. Open and filled circles represent measurements with the magnetic field in the $+Y$ and $-Y$ direction. The solid and dashed lines represent best fits to the data points. Only for the YY configuration a dependence on the direction of the magnetic field is clearly seen.

fourfold symmetry with only four lobes because the values of the constant terms of Eqs. (5.4) and (5.6) are larger than the amplitude of the corresponding $\cos(4\phi)$ terms. The XY and YY curves show eightfold symmetry as expected in the absence of such constant terms.

Figure 5.3 shows the measured SH intensity originating from the film surface, obtained by illuminating the sample from the substrate side. For the configurations XX , YX , and XY there is essentially no observable magnetic field dependence. The fourfold and eightfold symmetry of these curves is in accordance with Eqs. (5.4) and (5.6). The small lobes occurring in the YX configuration arise because the constant term in Eq. (5.6) now is smaller than the amplitude of the $\cos(4\phi)$ term. In contrast,

Table 5.1: Parameters of Eqs. (5.4)-(5.8) giving a best fit to the measured SHG rotational anisotropy. All values are normalized to $A(\text{interface}) = -1$.

Tensor comp.	Interface	Surface	Reference	
			XX	XY
A	-1.00	-0.11	-0.06	0.09
B	0.76	1.42	0.78	1.12
C	2.22	0.56	0.31	0.44
D^2		0.67 ³	1.29	0.64

the YY curve shows a pronounced and unexpected dependence on the field direction. This must be attributed to interference between different sources of SHG which respond differently to the change in direction of the magnetic field. These could either be magnetic domains or clusters differently magnetized from the surrounding single crystalline film, or nonmagnetic sources such as inclusions or structural irregularities. Note that any dependence on the direction of \mathbf{M} was never seen for the signal from the film-substrate interface.

The data in Fig. 5.3 (YY) can be described by Eq. (5.6) if a constant isotropic term D , independent of both \mathbf{M} and ϕ is added

$$P'_{YY} = E_Y^2 \frac{\epsilon_0}{4} [D - M(A + 2B + C) \sin 4\phi]. \quad (5.8)$$

The curves then split for $\pm\mathbf{M}$ due to interference between the magnetization induced and the nonmagnetic contribution, as shown by the solid and dashed lines.

A distortion of the crystal symmetry could lead to crystallographic contributions to the SHG, but it would be expected to have some angular dependence. Surface roughness or clusters could produce magnetic or nonmagnetic domains or grains with different properties from the rest of the material, and these might give an isotropic contribution to the SHG.

By studying the garnet film surface in an optical microscope we have found that, in fact, it has small inclusions scattered across the whole surface. The size of the dots in Figure 5.4 appears to be approximately $0.5 \mu\text{m}$, but their real size could be much smaller due to the diffraction limited resolution.

Ideally, the fit parameters for both surface and interface SHG should be the same. The fact that they are not may be explained by the different local environment. At the interface there is some strain due to lattice mismatch between film and substrate,

²Equations (5.4)-(5.7) are modified with a constant (isotropic and nonmagnetic) term D to account for the observed nonmagnetic contribution to the signal. See Eq. (5.8).

³This nonmagnetic contribution is only used to fit the data for the YY configuration.

which may have relaxed at the surface. In addition there could be gradients in the composition of the film, i.e., growth induced anisotropy.

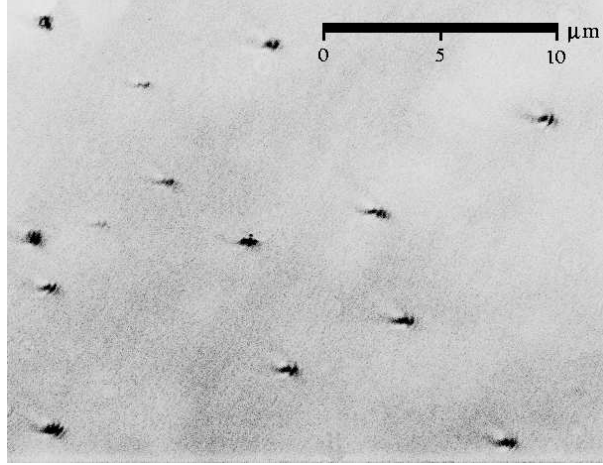


Figure 5.4: Optical microscope image of the approximately $0.5 \mu\text{m}$ inclusions observed on the garnet film surface. Their real size could be much smaller due to the diffraction limited resolution.

The effects of the surface inclusions were further studied by measuring the dependence of the SH intensity on the in-plane field strength. With polarizer and analyzer axis oriented along the Y -direction the sample was rotated to an angle $\phi = \phi'$ giving a minimum in the SH signal. For this YY -configuration there are eight equally spaced minima, as shown by the SHG rotational anisotropy in Figs. 5.2 and 5.3. The SH intensity was recorded as a function of the strength of the applied magnetic field, and the results are shown in Fig. 5.5 for both the surface and the interface signal. The empty points represent measurements at $\phi = \phi'$, which is also the same orientation at which the XX -configuration gives a minimum signal, while the filled points were measured at a neighboring minimum, $\phi = \phi' + 45^\circ$. For these two orientations of the sample, the behavior of the SH intensity near zero applied field is very different. At $\phi = \phi'$ the interface signal does not show any dependence on the strength of the applied field. The constant SHG signal even near zero applied field indicates that the magnetization simply flips 180° as the field changes polarity. In contrast, the SH intensity increases strongly near zero applied field for the $\phi = \phi' + 45^\circ$ orientation of the sample. In addition to the fact that the easy direction of magnetization of this film is of the in-plane type, there also exists a small fourfold magnetocrystalline anisotropy in the film plane. Because of this magnetocrystalline anisotropy the magnetization

does not simply flip 180° , but appears to first rotate 90° to an equivalent and preferred in-plane orientation. This conclusion is supported by the fact that the peak intensity at zero field is equal to the maximum intensity measured for the rotational anisotropy in the XX configuration (Figs. 5.2 and 5.3).

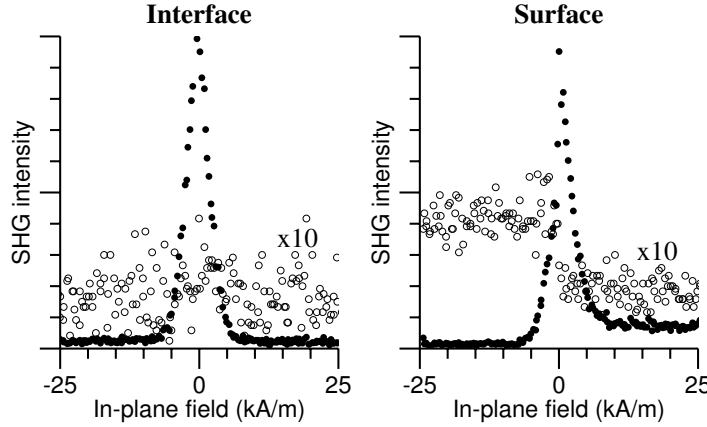


Figure 5.5: Dependence of the SH intensity on the strength of the applied in-plane magnetic field. Empty and filled points correspond to measurements at two neighboring minima in the YY configuration, i.e., at ϕ' and $\phi' + 45^\circ$, respectively. The very different behavior near zero applied field is due to a small in-plane magnetocrystalline anisotropy which causes different switching behavior of the magnetization depending on its orientation with respect to the crystal axes. Interference between magnetic and nonmagnetic sources of SHG can be seen as steps in the SH intensity originating from the film surface, while the interface signal is of purely magnetic origin.

It is also evident from Fig. 5.5 that the surface SHG signal is composed of a magnetic and a nonmagnetic source. The interference between these gives rise to the different signal levels for $\pm \mathbf{M}$ as described by Eq. (5.2). Also for the surface signal the influence of the in-plane magnetocrystalline anisotropy on the switching mechanism is evident. When oriented at $\phi = \phi'$ there is simply a step in the SHG intensity due to the phase change of π in the magnetization-induced contribution as \mathbf{M} changes sign. At $\phi = \phi' + 45^\circ$ the same mechanism of switching as described for the interface can be seen. Interference between non-magnetic and magnetic sources of SHG is also clearly seen as a difference in signal levels for $\pm \mathbf{M}$.

The experimental data in Fig. 5.5 show no evidence of domain pinning by the surface inclusions. The dependence of the SH intensity on the field was measured at in-plane fields up to 300 kA/m, but remained constant at the levels shown in the

figure. It is not clear what the inclusions are but apparently they cause a nonmagnetic contribution to the SHG from the film surface, most clearly seen in the YY configuration. Note that a similar effect, though much weaker is observed in the XY polarization combination.

5.2.1 Phase-sensitive measurements of SHG

In accordance with the experimental results of Fig. 5.3, configurations XX , XY and YX , the radiated intensity [Eq. (5.2)] appears not to be sensitive to the phase change of π in the induced polarization at 2ω [Eqs. (5.4)-(5.7)] that occurs when the magnetization is reversed, $\mathbf{M} \rightarrow -\mathbf{M}$. To confirm the existence of this phase shift the SH wave from the magnetic garnet sample was made to interfere with a SH wave generated in a nonmagnetic "reference" sample [19, 20]. By placing a glass substrate coated with a polymer film having large second-order optical nonlinear coefficients just after the garnet film we achieve spatial overlap of the SH waves from the two sources. As long as no strongly dispersive elements are inserted between the garnet film and the reference sample, the fundamental pulse and the SH pulse will also overlap temporally as they reach the reference. SH radiation generated in the polymer film will then interfere with the SH light from the garnet film. This can be observed as a change in detected intensity upon reversal of the direction of magnetization, because the interference term in Eq. (5.2) changes sign.

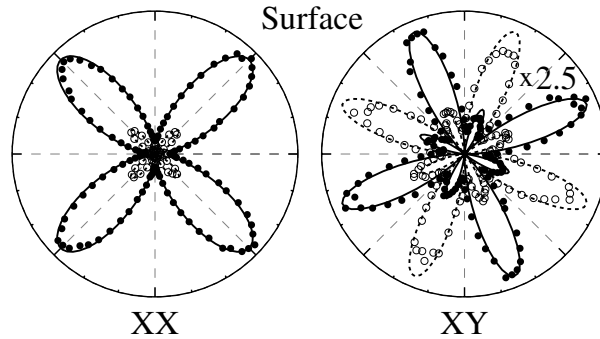


Figure 5.6: SHG rotational anisotropy measurement of the surface of the garnet film with a stationary external polymer reference. The signal for $\pm\mathbf{M}$ can be seen to split due to interference between the magnetization induced SHG in the garnet film and the SHG in the polymer film.

This can be modeled by Eqs. (5.4)-(5.7) by adding a constant isotropic term D , as was done in Eq. (5.8). The rotational anisotropy of the total SH-intensity is shown

in Fig. 5.6 for $\pm \mathbf{M}$. As the direction of the magnetic field is reversed, the SHG from the garnet film experiences a phase shift of π and the interference term of Eq. (5.2) changes sign. For the XX configuration the intensity is reduced significantly while the XY curve splits. The fitting parameters are listed in Table 5.1. Note that the value of the coefficients A , B , and C are the same as those found by fitting the surface signal in Fig. 5.3, only scaled by a factor 0.55 and 0.79 for the XX and YX configurations, respectively. The reason for this scaling is that the polymer film absorbs some of the SH light. The different magnitude of the constant contribution D for the XX and XY configurations is due to the strongly anisotropic second order susceptibility of the stationary polymer film, i.e., $\chi_{xxx} \neq \chi_{yxx}$.

Dispersion in the substrate prevents the same experiment to be conducted with the SHG from the interface, however, the problem may be overcome by analyzing the spectrum of the signal [21].

5.2.2 Polar magnetic field dependence of the SHG

In order to further investigate the surface and interface magnetic properties in comparison to those of the bulk, the magnetization-induced SHG signal, and the (bulk) linear Faraday rotation were studied as function of an out-of-plane magnetic field. The sample was placed in a strong polar magnetic field, i.e., along the Z -direction, and rotated to an azimuthal angle giving a peak in the observed SH intensity. The intensity of the SH light and the linear Faraday rotation of the fundamental beam were then measured simultaneously as a function of the polar field strength up to 600 kA/m. This was done for light incident from both the substrate and the film side of the sample.

In both cases the strongest SHG signal was observed close to zero polar magnetic field. The spontaneous magnetization of the garnet film is then in-plane. As the magnetization is gradually forced out-of-plane by the polar field, the SHG signal decreases and eventually vanishes (reaches level of PMT background noise) as the magnetization is saturated in the out-of-plane direction. This is shown in Fig. 5.7. The figure also shows the simultaneously measured Faraday rotation of the fundamental beam, corrected for the contribution of the paramagnetic GGG substrate. The Faraday rotation appears to saturate at a clearly lower value of the magnetic field than the SH signal from both surface and interface, indicating that the bulk magnetization saturates in the out-of-plane direction before the surface and interface magnetizations. Furthermore, it is very interesting to note the different saturation magnetic fields of the SH signal from the surface and interface. A significantly stronger field is required to saturate the interface magnetization in the out-of-plane direction, again demonstrating that the anisotropy at the interface, leading to an easy magnetization of the in-plane type, is relaxed at the surface.

The noise and sudden drop in the SH intensity near zero field can be explained

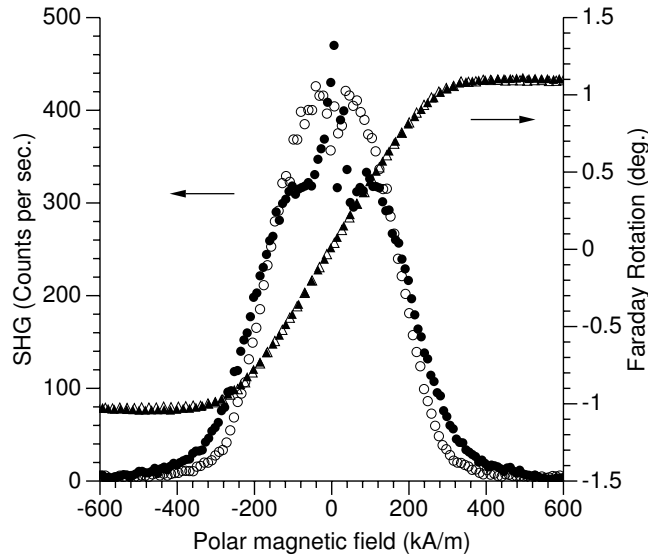


Figure 5.7: Simultaneously measured SHG intensity and Faraday rotation of the fundamental beam as a function of the applied polar magnetic field. Results obtained with the garnet sample illuminated from the substrate side are shown by empty symbols, while the filled symbols represent measurements with light incident from the film surface side. The data have been averaged over measurements taken at increasing and decreasing magnetic field.

by the random in-plane orientation of the magnetization. As demonstrated by the rotational anisotropy measurements, the orientation of the in-plane magnetization with respect to the crystal lattice has a large influence on the SHG response.

This experiment demonstrates the applicability of SHG to probe surface and interface magnetic properties. In addition, the results again confirm the dominantly magnetic origin of the observed SHG, and also demonstrate that the SHG effectively can be switched off using a polar magnetic field. This could find technological applications, for instance as a switchable element in lasers. The field strength required to completely switch off the SHG, that is to orient the magnetization in the out-of-plane direction, depends strongly on the chemical composition of the garnet film [22]. We have verified for other garnet films grown on the same substrate orientation, but with higher concentrations of gallium, that the Faraday rotation saturates and the SHG signal vanishes at lower magnetic fields. The sensitivity can thus be tuned by altering the composition of the films. Modulation or switching of the SHG can also be

achieved by varying the direction of the in-plane magnetization which requires much smaller magnetic fields.

5.3 Conclusions

We have shown, for thin garnet films grown on (001) oriented GGG substrates, that magnetization-induced SHG can serve as a powerful interface selective probe of the local magnetic structure. Since the space inversion symmetry in this case is broken throughout the whole film, the interface sensitivity is not due to symmetry breaking by the interfaces, but stems from the fact that the onset of strong optical absorption in the garnet films is conveniently located at about 2.3 eV, in-between the fundamental and second harmonic frequencies.

We have experimentally confirmed that the observed SHG from our film-substrate interface is of purely magnetic origin, as predicted by electromagnetic theory in the electric dipole approximation. The surface signal is dominantly of magnetic origin but also has a small nonmagnetic component. We have found that this is due to small grain-like inclusions in the surface of these LPE grown garnet films which act as nonmagnetic sources of SHG. No direct evidence of domain pinning by these inclusions have been observed.

It was found that the magnetization at the film surface and interface saturates in the out-of-plane direction at different strengths of the applied field, and both higher than the field necessary to saturate the bulk. We conclude that the anisotropy leading to easy magnetization of the in-plane type is stronger at the interface than at the surface. A small fourfold in-plane magnetocrystalline anisotropy was also identified.

References

- [1] L. Dorosinskii, M. Indenbom, I. Nikitenko, Y. Ossipyan, A. Polyanskii, and V. Vlasko-Vlasov, *Physica C* **203**, 149 (1992).
- [2] M. Koblishka and R. Wijngaarden, *Supercond. Sci. Technol.* **8**, 199 (1995).
- [3] P. Goa, H. Hauglin, M. Baziljevich, E. Il'yashenko, P. Gammel, and T. Johansen, *Supercond. Sci. Technol.* **14**, 729 (2001).
- [4] J. Reif, J. Zink, C. Schneider, and J. Kirschner, *Phys. Rev. Lett.* **67**, 2878 (1991).
- [5] H. Wierenga, W. de Jong, M. Prins, T. Rasing, R. Vollmer, A. Kirilyuk, H. Schwabe, and J. Kirschner, *Phys. Rev. Lett.* **74**, 1462 (1995).
- [6] M. Straub, R. Vollmer, and J. Kirschner, *Phys. Rev. Lett.* **77**, 743 (1996).

- [7] T. Crawford, C. Rogers, T. Silva, and Y. Kim, Appl. Phys. Lett. **68**, 1573 (1996).
- [8] K. Bennemann, *Nonlinear Optics in Metals*, International series of monographs on physics (Clarendon Press, Oxford, 1998).
- [9] V. Pavlov, R. Pisarev, M. Fiebig, and D. Fröhlich, Phys. Solid State **45**, 662 (2003).
- [10] M. Fiebig, D. Fröhlich, K. Kohn, S. Leute, T. Lottermoser, V. Pavlov, and R. Pisarev, Phys. Rev. Lett. **84**, 5620 (2000).
- [11] M. Fiebig, D. Fröhlich, B. Krichevstov, and R. Pisarev, Phys. Rev. Lett. **73**, 2127 (1994).
- [12] M. Born and E. Wolf, *Principles of Optics* (Cambridge University Press, 1998), 6th ed.
- [13] V. Gridnev, V. Pavlov, R. Pisarev, A. Kirilyuk, and T. Rasing, Phys. Rev. B **63**, 184407 (2001).
- [14] V. Pavlov, R. Pisarev, A. Kirilyuk, and T. Rasing, Phys. Rev. Lett. **78**, 2004 (1997).
- [15] R. Pisarev, B. Krichevstov, V. Gridnev, V. Klin, D. Fröhlich, and C. Pahlke-Lerch, J. Phys.: Condens. Matter **5**, 8621 (1993).
- [16] R. R. Birss, *Symmetry and Magnetism*, Series of monographs on selected topics in solid state physics (North-Holland, Amsterdam, 1966), 2nd ed.
- [17] D. L. Wood and K. Nassau, Appl. Opt. **29**, 3704 (1990).
- [18] F. Hansteen, L. E. Helseth, T. H. Johansen, O. Hunderi, A. Kirilyuk, and T. Rasing, Thin Solid Films **455-456C**, 429 (2004).
- [19] R. Stolle, K. Veenstra, F. Manders, T. Rasing, H. van den Berg, and N. Persat, Phys. Rev. B **55**, R4925 (1997).
- [20] R. Chang, J. Ducuing, and N. Bloembergen, Phys. Rev. Lett. **15**, 6 (1965).
- [21] K. Veenstra, A. Petukhov, A. de Boer, and T. Rasing, Phys. Rev. B **58**, R16020 (1998).
- [22] L. Helseth, R. Hansen, E. Il'yashenko, M. Baziljevich, and T. Johansen, Phys. Rev. B **64**, 174406 (2001).

CHAPTER 6

Ultrafast coherent optical control of the magnetization in garnet films ¹

Abstract

We demonstrate coherent optical control of the magnetization in ferrimagnetic garnet films on the femtosecond time scale through a combination of two different ultrafast and nonthermal photomagnetic effects and by employing multiple pump pulses. Linearly polarized laser pulses are shown to create a long-lived modification of the magnetocrystalline anisotropy via optically induced electron transfer between nonequivalent ion sites while circularly polarized pulses additionally act as strong transient magnetic field pulses originating from the nonabsorptive inverse Faraday effect. Due to the slow phonon-magnon interaction in these dielectrics, thermal effects of the laser excitation are clearly distinguished from the ultrafast nonthermal effects and can be seen only on the time scale of nanoseconds for sample temperatures near the Curie point. The reported effects open new and exciting possibilities for ultrafast manipulation of spins by light, and provide new insight into the physics of magnetism on ultrafast time scales.

¹Adapted from: F. Hansteen, A.V. Kimel, A. Kirilyuk, and Th. Rasing *Phys. Rev. Lett.* **95**, 047402 (2005), and F. Hansteen, A.V. Kimel, A. Kirilyuk, and Th. Rasing *Phys. Rev. B* **73**, 014421 (2006).

6.1 Introduction

As discussed in Chapter 1, coherent precession is the fastest known way to alter the direction of the macroscopic magnetization in a material. Phenomenologically the process can be described by the Landau-Lifshitz equation of motion [1]

$$\frac{d\mathbf{M}}{dt} = -\gamma (\mathbf{M} \times \mathbf{H}_{\text{eff}}), \quad (6.1)$$

where the Gilbert damping term has been neglected (see Eq. 1.2). It follows from this that the equilibrium orientation ($d\mathbf{M}/dt = 0$) for the magnetization \mathbf{M} is along the direction of the effective magnetic field \mathbf{H}_{eff} which is composed of the externally applied field \mathbf{H}_{ext} , the anisotropy field \mathbf{H}_{a} , and the demagnetizing field \mathbf{H}_{dem} .

$$\mathbf{H}_{\text{eff}} = \mathbf{H}_{\text{ext}} + \mathbf{H}_{\text{a}} + \mathbf{H}_{\text{dem}}. \quad (6.2)$$

Therefore, the key to optical manipulation of the magnetization lies in the control of these fields by light. It has been demonstrated that ultrafast laser excitation can lead to rapid demagnetization and to thermal modulation of the anisotropy field in metallic magnetic systems (see Chapter 1) [2, 3]. This allows in principle for some control of the magnetization, but with very limited degrees of freedom. Moreover, the time needed for the system to cool down and recover from this excitation will severely limit the repetition rate of such a thermal approach.

This Chapter presents the results from an extensive study of ultrafast optical magnetization control in dielectric ferrimagnetic garnet films. Laser pulses of center wavelength $\lambda = 805\text{nm}$ and pulse width 100 fs were used to both excite and probe the magnetic response of the films. We demonstrate the existence of two different *nonthermal* photomagnetic effects that allow for ultrafast control of both the magnetocrystalline anisotropy and the magnetization. Thermal effects are clearly distinguished from the nonthermal effects and can be observed on the time scale of several nanoseconds in the vicinity of the Curie temperature.

Experimental details, including sample characteristics and experimental setup, are given in Section 6.2. In Section 6.3 the experimental results obtained from studies of laser-induced magnetization dynamics in garnets are presented and discussed. This section is divided into four subsections describing respectively nonthermal optical control of magnetic anisotropy, nonthermal optical control of magnetization, ultrafast photomagnetic switching, and slow thermal effects that can be seen on longer time scales near the Curie point.

6.2 Experimental

The samples studied in this work are 4 – 8 μm thick ferrimagnetic garnet films of composition $\text{Lu}_{3-x-y}\text{Y}_x\text{Bi}_y\text{Fe}_{5-z}\text{Ga}_z\text{O}_{12}$ grown on (001) oriented gallium gadolinium

garnet (GGG) substrates by liquid phase epitaxy. All the results presented here are from samples with $x = 0.65$, $y = 0.66$, and $z = 1.15$, but the observed effects are also present in a whole series of samples with similar composition. Small amounts of Pb impurities are known to exist in these types of films due to the flux from which they are grown. The films have in-plane magnetization, $4\pi M_s = 550$ G, Curie temperature $T_C = 400$ K, and show almost no domain activity. While bulk garnet crystals have cubic symmetry and possess a center of inversion, epitaxially grown thin garnet films seem to lack this center of symmetry, as has been demonstrated by the existence of a linear magnetoelectric effect [4] and by strong optical second-harmonic generation [5, 6].

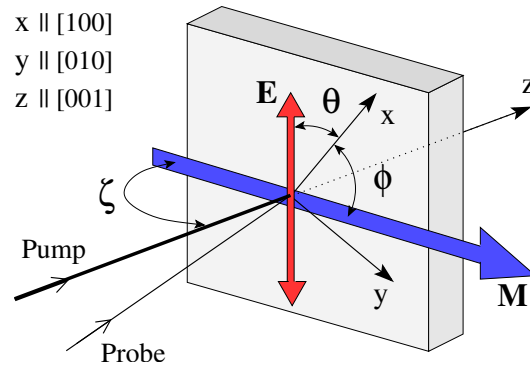


Figure 6.1: Experimental geometry. Pump and probe pulses are incident on the garnet film at near normal incidence. The magnetization \mathbf{M} of the sample forms an angle ζ with the sample normal $[001]$ and an angle ϕ with the crystallographic $[100]$ x -axis of the film. For linearly polarized pump pulses the angle of the light's electric field \mathbf{E} with respect to the sample x -axis is denoted θ .

The garnet films were studied in transmission using an all-optical pump and probe technique. Regeneratively amplified 100 fs pulses of wavelength $\lambda = 805$ nm emitted from a Ti:Sapphire laser system at a repetition rate of 1 kHz were split into two parts using a beam splitter. The most intense part (pump) was incident on the sample at near normal incidence. The magnetization dynamics induced by these pump pulses was followed in time by measuring the Faraday rotation θ_F of the time delayed and much weaker probe pulses ($I_{\text{pump}}/I_{\text{probe}} > 1000$) as function of the variable pump-probe separation Δt . The Faraday angle θ_F is proportional to the projection of the magnetization vector \mathbf{M} along the wave vector \mathbf{k} of the probe light:

$$\theta_F \propto \mathbf{M} \cdot \mathbf{k}. \quad (6.3)$$

In our geometry (see Fig. 6.1) the measured Faraday rotation is therefore essentially a

probe of the out-of-plane M_z component of the magnetization. For sensitive detection of the magneto-optical Faraday rotation a balanced photodiode detector was used in combination with a box-car integrator [7]. A synchronized optical chopper operating at 500 Hz was placed in the pump beam path, thereby blocking every second pump pulse and creating alternating pump-on and pump-off conditions in the sample. For every pump-probe delay Δt the pump-induced Faraday rotation was averaged over several excitation events by use of a lock-in amplifier. Pump-induced changes of the optical transmittivity of the sample was recorded simultaneously with the Faraday rotation by measuring the intensity of the probe pulses in addition to their polarization rotation.

The linear optical absorption of these garnet films in the spectral region around $\lambda = 805$ nm (1.54 eV) is small ($\alpha \approx 20$ cm⁻¹) and mainly due to spin- and parity-”forbidden” $d-d$ transitions in the Fe³⁺ ions and a tail from higher energy charge transfer transitions at 2.8 and 3.4 eV [8, 9]. The magneto-optical properties of the material in the infrared part of the spectrum are dictated mainly by the tails of these high energy transitions. It is also well known that bismuth substitution strongly enhances the magneto-optical response [8, 9].

The Faraday rotation θ_F measured with a saturating external field normal to the film plane is shown as function of the sample temperature in Fig. 6.2 for a 7.5 μ m thick garnet film. $M(T)$ exhibits a second order phase transition with a critical exponent $\beta = 0.414$ and a Curie temperature of $T_C = 400$ K, both in agreement with previous studies of similar materials [8, 9]. From the hysteresis loop in Fig. 6.2(b) it can be seen that the sample exhibits no coercivity and has a large Faraday rotation of about 2.5° at room temperature when saturated in the out-of-plane direction. The Faraday rotation measured at a small angle of incidence with the applied magnetic field parallel to the sample plane is shown by the hysteresis loop in Fig. 6.2(c). It gives an estimate of the film in-plane anisotropy H_a of about 50 Oe. Vibrating sample magnetometer (VSM) measurements reveal that this anisotropy has a fourfold symmetry in the plane.

Pump pulses of energy up to 20 μ J were focused to a spot diameter of about 200 μ m on the sample, corresponding to a photon density of approximately one photon per unit cell in the irradiated sample volume. The laser peak power density of about 10¹¹ W/cm² is still well below the threshold for continuum generation in the garnet films. While the probe pulses always were linearly polarized, the polarization of the pump pulses could be varied using a Babinet-Soleil compensator. A magnetic field was applied either in the xy -plane of the sample, see Fig. 6.1, or at an angle with respect to the sample normal, thereby pulling the magnetization \mathbf{M} out of the film plane ($\zeta < 90^\circ$). Additionally, the sample temperature could be controlled from room temperature up to well above the Curie point using a sample holder with a built-in heater and an electronic temperature regulator.

Unless otherwise explicitly stated, the results presented in the following section

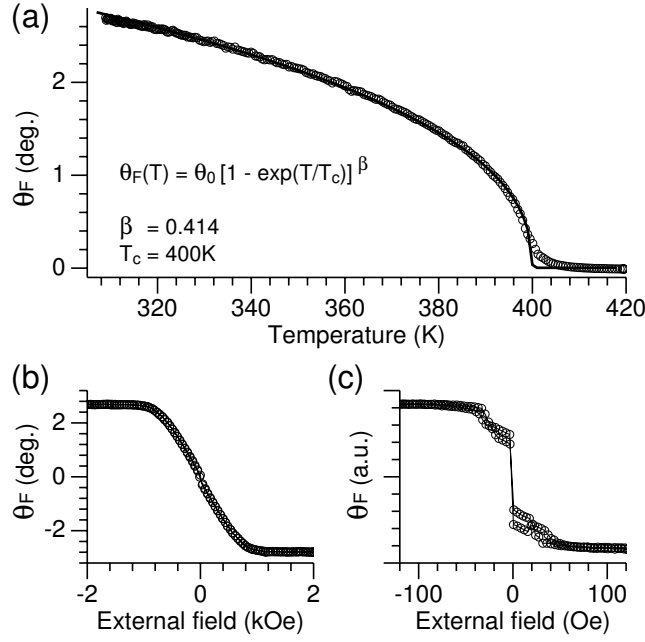


Figure 6.2: Sample characteristics. (a) Measured Faraday rotation θ_F at $\lambda = 800\text{ nm}$ as a function of temperature with a saturating applied field \mathbf{H}_{ext} normal to the film plane. (b) Hysteresis loop at $T = 300\text{ K}$ measured with \mathbf{H}_{ext} normal to the film. (c) Hysteresis loop measured at a small angle of incidence with \mathbf{H}_{ext} in the sample plane, indicating the presence of anisotropy fields of about 50 Oe.

were all obtained at room temperature and with pump pulse energies near $20\text{ }\mu\text{J}$.

6.3 Results and discussion

In this section, which is divided into four main parts, we present and interpret our experimental results from extensive studies of optically induced magnetization dynamics in garnet films. A remarkable amount of information about the underlying photomagnetic mechanisms can be obtained simply by analyzing time-traces of the precessional dynamics.

Two different photomagnetic effects have been found to trigger coherent precession of the magnetization. In Section 6.3.1 we present results showing that linearly polarized laser pulses create a long-lived modification of the magnetocrystalline anisotropy

in garnet films. The effect is ultrafast and not of thermal origin, and it causes the magnetization to start precessing immediately after the photoexcitation. In Sect. 6.3.2 an additional effect of circularly polarized laser pulses on the magnetization is discussed along with the experimental results. It is found that these pulses act as strong axial magnetic field pulses during their presence in the sample. Also this effect is of nonthermal origin. These two photomagnetic effects can be combined as demonstrated in Sect. 6.3.3 to achieve switching of the magnetization on a femtosecond time scale. Slow thermal effects of the laser pulses are also present and can be seen when the sample is held at temperatures close to the Curie point. These effects are discussed in Sect. 6.3.4.

6.3.1 Photoinduced magnetic anisotropy

Experimental observations

Applying an external magnetic field \mathbf{H}_{ext} in the plane of the sample (so that \mathbf{M} is in-plane, $\zeta = 90^\circ$) and pumping with linearly polarized laser pulses, optically triggered precession of the magnetization \mathbf{M} was observed, see Fig. 6.3(a). In the optical transmittivity of the sample Fig. 6.3(b), a sudden drop is seen which does not relax significantly within 3 ns. Intriguingly, the amplitude and phase of the precession in Fig. 6.3(a) was found to depend on the plane of polarization θ of the pump pulses as shown in Fig. 6.3(c). Negative values of the amplitude indicate precession of \mathbf{M} with the opposite phase. Maxima of the precessional amplitude (of the opposite phase) were observed for every 90° rotation of the polarization, and at some polarizations no precessional dynamics was triggered. From this dependence on pump polarization it is evident that the underlying effect must be nonthermal. An ultrafast heating effect would only reduce the magnitude of the magnetization and the anisotropy field independently of the pump polarization. Heating effects thus can not be responsible for triggering magnetization dynamics that exhibit polarization dependence of the type that we observe in Fig. 6.3.

It is also interesting to note that \mathbf{M} always starts its precessional motion by moving normal to the film plane along the $\pm\hat{z}$ -direction. This follows from the initial phase of the measured signal in Fig. 6.3(a) which always starts from the inflection point where M_z is changing most rapidly. From the Landau-Lifshitz equation [Eq. (6.1)] it can be inferred that immediately after the photo excitation both \mathbf{M} and \mathbf{H}_{eff} are in the film plane but not parallel to each other. Consequently, the observed magnetization dynamics must be due to an ultrafast change of the magnetization $\delta\mathbf{M}$, the anisotropy field $\delta\mathbf{H}^a$, or a combination of the two, that effectively creates an in-plane angular displacement $\Lambda = \angle(\mathbf{M}, \mathbf{H}_{\text{eff}})$ between \mathbf{M} and \mathbf{H}_{eff} . It is possible to distinguish between these possibilities by analyzing the precession amplitude Λ as function of the applied field. The result is shown in Figs. 6.3(d) and 6.4(a). If triggered by an ultrafast rotation of the magnetization $\mathbf{M} \rightarrow \mathbf{M} + \delta\mathbf{M}$, the amplitude

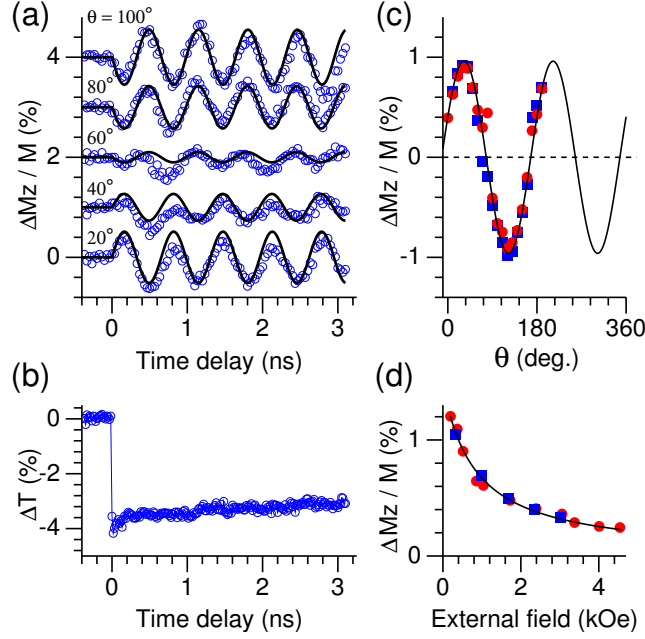


Figure 6.3: Coherent precession of the magnetization triggered by linearly polarized laser pulses. (a) Time dependence of the precession for different planes of pump polarization θ , with an applied field of $|\mathbf{H}_{\text{ext}}| = 350$ Oe in the plane of the sample. Circles represent measurements and solid lines simulations based on the Landau-Lifshitz equation. (b) Pump-induced change of the sample transmittivity ΔT . (c) Precessional amplitude as a function of the plane of pump polarization. Round (red) and square (blue) symbols represent amplitudes extracted from measurements at $\pm \mathbf{H}_{\text{ext}}$. The solid line is a best fit. (d) Dependence of the precessional amplitude on the applied magnetic field \mathbf{H}_{ext} .

Λ of the subsequent precession should be independent of the strength of the applied magnetic field as $\angle(\mathbf{M}, \mathbf{H}_{\text{eff}})$ does not depend on \mathbf{H}_{ext} . However, if precession is caused by a change in the effective field through a photoinduced anisotropy field $\delta \mathbf{H}^a$, the precession amplitude Λ is expected to decrease with increasing applied magnetic field as

$$\Lambda = \angle(\mathbf{H}_{\text{eff}}, \mathbf{H}_{\text{eff}} + \delta \mathbf{H}^a) \propto \frac{1}{|\mathbf{H}_{\text{ext}} + \mathbf{H}_a|} \quad (6.4)$$

which is valid for small amplitude precessions. As shown by the fitted curve in Fig. 6.3(d) (solid line) the measurements exhibit the exact behavior that one expects for a

photoinduced anisotropy field $\delta\mathbf{H}^a$. Based on the precession amplitude, the magnitude of the photoinduced field can be estimated to $\delta H^a = 0.5$ Oe for the present geometry ($\zeta = 90^\circ$). A graphical illustration of the excitation process and the subsequent precession is shown in Fig. 6.5.

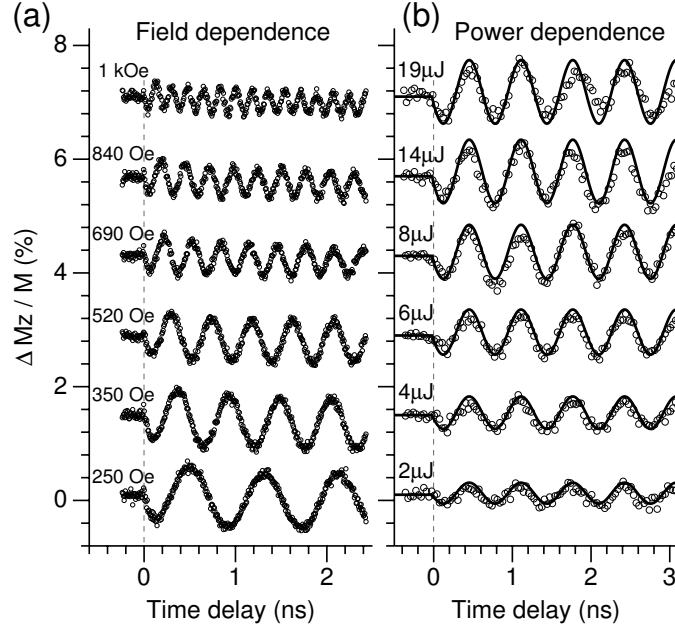


Figure 6.4: Time traces of the precession excited by linearly polarized laser pulses (a) for different values of the in-plane applied magnetic field \mathbf{H}_{ext} at a pump power of $20 \mu\text{J}/\text{pulse}$, and (b) for different pump powers with $H_{\text{ext}} = 300$ Oe.

For the present geometry, with the applied field in the plane of the film, changing the polarity of the magnetic field \mathbf{H}_{ext} does not affect the measured signal for any given polarization of the pump. The fact that the precession phase and amplitude are both unaffected by reversing the polarity of the external field [see Fig. 6.3(c)] shows that $\delta\mathbf{H}^a$ must be odd with respect to \mathbf{M} : when changing the polarity of the external field both \mathbf{M} and the anisotropy field \mathbf{H}_a in Eq. (6.2) change sign. It then follows from Eq. (6.1) that the photoinduced $\delta\mathbf{H}^a$ also must change sign, i.e. $\delta\mathbf{H}^a \rightarrow -\delta\mathbf{H}^a$ in order to give rise to the same signal.

By applying the external field at an angle the magnetization can be tilted out of the film plane ($\zeta < 90^\circ$). The actual angle ζ that the magnetization makes with the film normal is determined by the balance between the applied field, the anisotropy

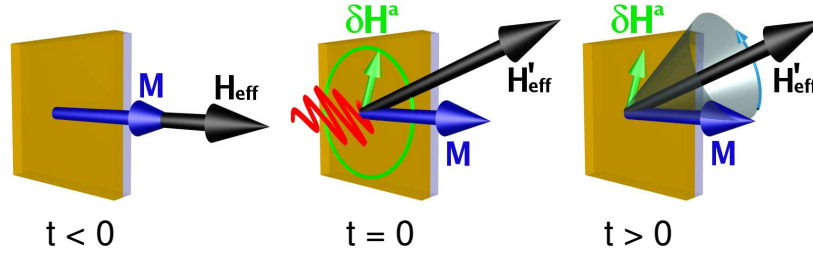


Figure 6.5: Graphical illustration of the process of photoinduced magnetic anisotropy caused by linearly polarized laser excitation and the subsequent precessional dynamics.

field, and the demagnetizing field. When pumping with linearly polarized laser pulses in this configuration, a larger amplitude precession was observed, see Fig. 6.6(a). This precession is superimposed on a slowly decaying exponential background caused by the relaxation of the photoinduced anisotropy. In contrast to the in-plane applied field geometry (where $\zeta = 90^\circ$), the initial phase of the precession in Fig. 6.6(a) reveals that for \mathbf{M} tilted out of the film plane ($\zeta < 90^\circ$) the initial motion of \mathbf{M} is nearly parallel to the film plane. This implies that the laser-induced $\delta\mathbf{H}^a$ is directed essentially along the z -direction. The dependence of the precession amplitude and phase on the polarization of the pump pulses becomes gradually smaller as \mathbf{M} is tilted further out of the film plane. At about $\zeta = 60^\circ$ all polarization dependence is practically gone and changing the polarity of the external field gives a near 180° phase shift in the measured signal. The diminishing influence of the pump polarization is caused by the dominating z component of $\delta\mathbf{H}^a$, and will be discussed further in Sect. 6.3.1. From the precession amplitude in Fig. 6.6 the strength of the photoinduced anisotropy field is estimated to $\delta H^a = 1.5$ Oe.

Laser heating effects in the sample, if present, are likely to be more pronounced in this geometry than in the in-plane field geometry as a thermal reduction of \mathbf{M} also changes the equilibrium \mathbf{H}_{eff} and leads to a reorientation of \mathbf{M} along the z direction. However, in our experiments the optical excitation of coherent spin waves is ultrafast [see Fig. 6.6(b)], much faster than the phonon-magnon interaction time which is about 1 ns in this material [9], and therefore can not be of thermal origin. As will be discussed in Sect. 6.3.4, thermal effects can be seen on the time scale of a few nanoseconds when the sample is heated to temperatures near the Curie point.

Based on the results in Fig. 6.6(a) one can argue that the lifetime τ of $\delta\mathbf{H}^a$ is longer than the time $t_{\text{exp}} = 3$ ns accessible in this experiment. As the precession of \mathbf{M} is always around the effective magnetic field $\mathbf{H}'_{\text{eff}} = \mathbf{H}_{\text{eff}} + \delta\mathbf{H}^a$, any relaxation of

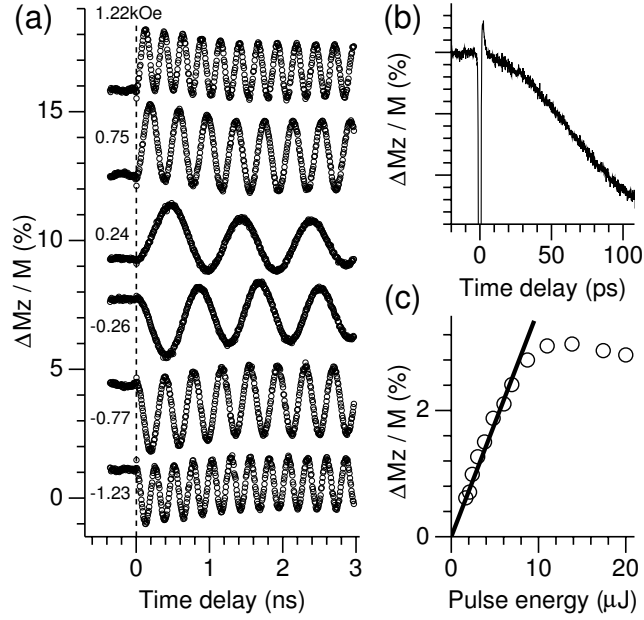


Figure 6.6: (a) Precession of the magnetization following excitation with linearly polarized light for different values of the magnetic field applied at an angle of about 45° with the sample normal. (b) The excitation shown on a finer time scale. (c) Dependence of precession amplitude on the excitation pulse energy.

$\delta \mathbf{H}^a$ should be visible in the time trace of the precession. Note in Fig. 6.6(a) how \mathbf{M} precesses around an equilibrium \mathbf{H}'_{eff} that is different from the initial $t < 0$ state. Some relaxation of \mathbf{H}'_{eff} can be seen (the slow overall change of the fast oscillating signal) but is not sufficient to restore the original equilibrium on the time scale of the experiment. This indicates that after $t_{\text{exp}} = 3$ ns $\delta \mathbf{H}^a$ has still not decayed completely. Another observation that supports this conclusion is the photoinduced change in the sample transmittivity ΔT shown in Fig. 6.3(d), which also does not relax significantly during 3 ns.

There appears to be a linear relation between the precession amplitude and the pump power [Fig. 6.6(c) and 6.4(b)] up to pulse energies of almost 10 μJ . At higher pulse energies the effect saturates completely. Based on the absorption coefficient the estimated density of absorbed photons is about one per hundred unit cells in the illuminated crystal volume. Saturation effects are therefore not expected unless they are caused by the presence of low concentration impurities. This will be discussed

in more detail in the following section on the microscopic basis of the photomagnetic effect.

Double-pump control of magnetocrystalline anisotropy

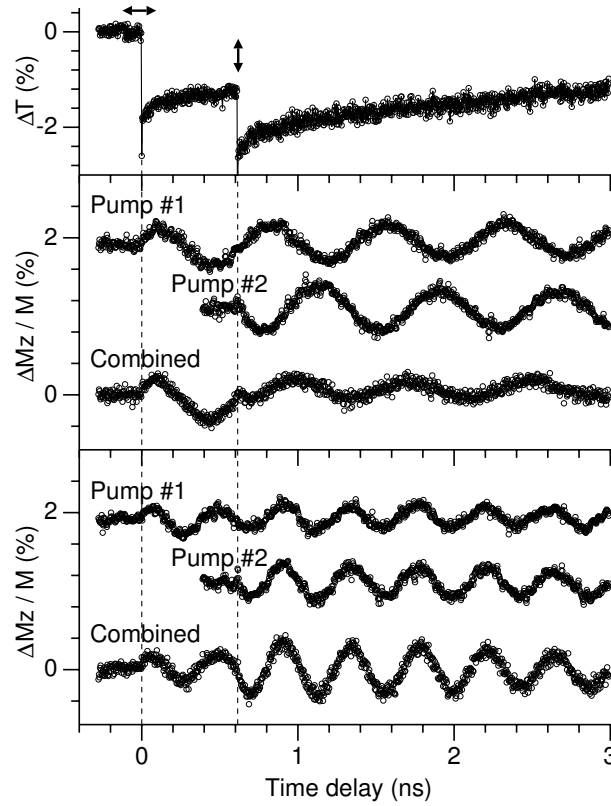


Figure 6.7: A double pump experiment with two $6 \mu\text{J}$ orthogonal linearly polarized pump pulses separated in time by approximately 600 ps. Timing with respect to the spin precession is done by varying the in-plane applied magnetic field and thereby the precession frequency. The top panel shows the photoinduced change of sample transmittivity. Partial quenching (middle panel) and amplification (lower panel) of the precession was achieved.

In order to investigate the possibility of repeatedly modifying the anisotropy field on a time scale shorter than its relaxation time a double pump experiment was con-

ducted. Using a Michelson interferometer-like configuration, the pump pulses were split into two with a beam splitter cube, and one part was delayed with respect to the other. A fixed time delay was used and the timing of the arrival of the second pump pulse with respect to the precessional dynamics was controlled by varying the precession frequency (applied field). By use of a quarter wave plate the linear polarization of the second pump pulse was set to be orthogonal with respect to the first one. A magnetic field was applied in the plane of the sample, and the dynamics triggered by the individual pump pulses was first recorded by blocking one of the pump pulses at a time. The results are shown in Fig. 6.7. The two orthogonally polarized pump pulses (denoted by pumps 1 and 2) trigger precession with the same amplitude and opposite phase, a result which was also known from Fig. 6.3(c). When allowing both pump pulses to reach the sample the resulting dynamics (denoted combined) in the time after the second pump pulse ($t > 0.6$ ns) is almost identical to the sum of the response of the two individual pump pulses. If the second pump pulse arrives after approximately one full precessional period, as shown in the middle panel, it causes quenching of the subsequent dynamics. However, the timing was not accurate enough to completely quench the precession in the present case. If the second pump pulse arrives after one and a half periods it causes subsequent precession with twice the amplitude, as shown in the lower panel. The two pump pulses appear to act completely independently, indicating that we are operating in the regime of linear response (see Fig. 6.6). However, the experiment does not provide an answer to whether the long lived anisotropy $\delta\mathbf{H}^a$ created by the first pump pulse is destroyed by the second pulse, or if the second pulse just creates additional anisotropy in the opposite direction.

In order to better understand our experimental results we describe in the following sections both a macroscopic phenomenological model and a microscopic one that accounts for the observed effects.

Phenomenological model of photoinduced magnetic anisotropy

In this section we give a macroscopic phenomenological description of the observed photoinduced magnetic anisotropy. The model is not concerned with the microscopic mechanism of the effect, but gives some insight into its symmetry properties.

The creation of a static magnetic field $\delta\mathbf{H}^a(0)$ in the sample can be described as a combination of the nonlinear process of optical rectification [10] and a linear magnetoelectric effect [11]

$$\delta H_i^a(0) = \chi_{ijkl} E_j(\omega) E_k(\omega) M_l(0). \quad (6.5)$$

Here E is the electric field component of light and M is the magnetization of the garnet film. The fourth rank polar tensor χ_{ijkl} has nonzero components for crystals of any symmetry [12].

When taking the experimental geometry (Fig. 6.1) and the symmetry of χ_{ijkl} for the 4mm point group of our samples into account, only four independent nonzero

components of the tensor χ_{ijkl} remain;

$$\begin{aligned}
 A &= \chi_{xxxx} = \chi_{yyyy}, \\
 B &= \chi_{xyxy} = \chi_{xxyy} = \chi_{yxyx} = \chi_{yyxx}, \\
 C &= \chi_{xyyx} = \chi_{yxxy}, \\
 D &= \chi_{zxzx} = \chi_{zyyz},
 \end{aligned} \tag{6.6}$$

and the vector components of the photoinduced anisotropy field are given by

$$\delta H_x^a \propto E_0^2 M_s \sin \zeta [(A + C) \cos \phi + (A - C) \cos 2\theta \cos \phi + 2B \sin 2\theta \sin \phi], \tag{6.7}$$

$$\delta H_y^a \propto E_0^2 M_s \sin \zeta [(A + C) \sin \phi - (A - C) \cos 2\theta \sin \phi + 2B \sin 2\theta \cos \phi], \tag{6.8}$$

$$\delta H_z^a \propto E_0^2 M_s D \cos \zeta. \tag{6.9}$$

Here δH_i^a is the photoinduced field along the i direction, $i = \{x, y, z\}$ refers to the crystal axes of the sample, ϕ denotes the azimuthal angle between the sample x axis and the projection of the magnetization vector on the film plane and ζ is the angle between the film normal and the magnetization, as shown in Fig. 6.1.

From these equations one can see that if the magnetization \mathbf{M} is in the film plane, the out-of-plane component δH_z of the photoinduced anisotropy field does not contribute as $\cos \zeta = 0$. This is in accordance with our experimental results from Fig. 6.3 which show an in-plane $\delta \mathbf{H}^a$. However, in order for the above equations to describe a field $\delta \mathbf{H}^a$ consistent with the polarization dependence of the precession amplitude, shown in Fig. 6.3(c), the number of independent tensor components must be further reduced. The fact that there is no amplitude offset in the curve shown in Fig. 6.3(c) requires that $A = -C$ so that the first term in Eqs. (6.7) and (6.8) vanishes. Furthermore, the sinusoidal shape of the curve implies that $A = B$ and leaves us with only two independent components of the tensor χ_{ijkl} ,

$$\begin{aligned}
 A &= \chi_{xxxx} = \chi_{yyyy} = -\chi_{xyyx} = -\chi_{yxxy} \\
 &= \chi_{xyxy} = \chi_{xxyy} = \chi_{yxyx} = \chi_{yyxx}, \\
 D &= \chi_{zxzx} = \chi_{zyyz}.
 \end{aligned} \tag{6.10}$$

These additional equalities indicate that the χ_{ijkl} tensor has a higher symmetry than the garnet crystal. However, this does not violate Neumann's principle which states that the symmetry elements of any physical property of a crystal must include all the symmetry elements of the point group of the crystal. This does not prevent that property from having a higher symmetry than the crystal. The optically induced anisotropy field can now be written as

$$\delta H_x^a \propto AE_0^2 M_s \sin \zeta [\sin 2\theta \sin \phi + \cos 2\theta \cos \phi], \tag{6.11}$$

$$\delta H_y^a \propto AE_0^2 M_s \sin \zeta [\sin 2\theta \cos \phi - \cos 2\theta \sin \phi], \tag{6.12}$$

$$\delta H_z^a \propto DE_0^2 M_s \cos \zeta. \tag{6.13}$$

For the in-plane field geometry ($\cos \zeta = 0$) this describes a vector of constant length and with a direction depending on the angle ϕ of the magnetization with respect to the x -axis and the plane of polarization θ of the pump pulses. The δH_z^a component accounts for the observed behavior in Fig. 6.6 with the applied field at an angle so that $\zeta < 90^\circ$.

Computer simulations based on this simple model and the numerical integration of Eq. (6.1) exhibit good agreement with our experimental results both for the in-plane \mathbf{H}_{ext} geometry shown in Fig. 6.3(a), and for the out-of-plane \mathbf{H}_{ext} geometry in Fig. 6.6 (simulations are not shown). The latter indicate that the tensor component D is larger than A by a factor of 3. This is not surprising in view of the symmetry distortion along the z -axis known to exist in films of this type [4, 5, 13].

Microscopic justification

Photomagnetic effects are known to exist in garnets containing certain dopants [14, 15], in particular Si and Co [16, 17]. Optically induced electron transfer between ions on nonequivalent sites in the crystal is believed to cause a change in the magnetocrystalline anisotropy due to a redistribution of ions [18]. This effect is strong in crystals doped with elements that can assume different valence states, and where their contribution to the anisotropy is different. However, it has also been observed in undoped garnet samples containing Pb impurities [19], which we believe is the case in our experiments.

The linear dependence of $\delta \mathbf{H}^a$ on the pump power shown in Fig. 6.6 suggests that linear optical absorption is the dominating absorption process. The saturation of $\delta \mathbf{H}^a$ at high pump intensities may be attributed to the Pb impurities. Divalent Pb^{2+} ions substitute trivalent Lu^{3+} ions on dodecahedral sites in the crystal. This is a p -type doping which creates holes that are usually assumed to be located on iron ions in tetrahedral sites [8, 20]. To maintain overall charge neutrality in the crystal, some tetrahedrally coordinated trivalent iron ions change their valency to $4+$. Photoexcitation can induce a charge transfer between these Fe^{4+} ions and Fe^{3+} magnetic ions in different sites, thus effectively "moving" the Fe^{4+} ions to sites with different symmetry, and thereby causing a change in the magnetic anisotropy. The low concentration of Pb impurities creates a limited number of photoactive ions and the photomagnetic effect can therefore be expected to saturate under intense illumination. An estimate for our sample shows that the illuminated volume of garnet film contains about 10^{12} Pb ions. An optical pulse of $20 \mu\text{J}$ delivers 10^{14} photons from which about 1% is expected to be absorbed. This allows, in principle, for all of the photoactive ions to be excited and it is thus not surprising that saturation can occur at these pump intensities. The pump-induced change in transmittivity is also believed to be related to the photoexcitation of impurities [21].

6.3.2 Optical control of magnetization

Experimental observations

Left- and right-handed circularly polarized laser pulses were used to excite the garnet film exposed to an in-plane applied magnetic field \mathbf{H}_{ext} . Precession of \mathbf{M} with an opposite phase and different amplitude was triggered by pulses of helicity σ^+ and σ^- , see Fig. 6.8. Note also that the precession amplitude for σ^+ is larger than the precession amplitude triggered by the linearly polarized pump pulses in the same geometry. As for linearly polarized pulses, the initial phase of the signal reveals that \mathbf{M} initially moves along the $\pm z$ direction and therefore both \mathbf{M} and \mathbf{H}_{eff} are parallel to the film plane immediately after the photoexcitation.

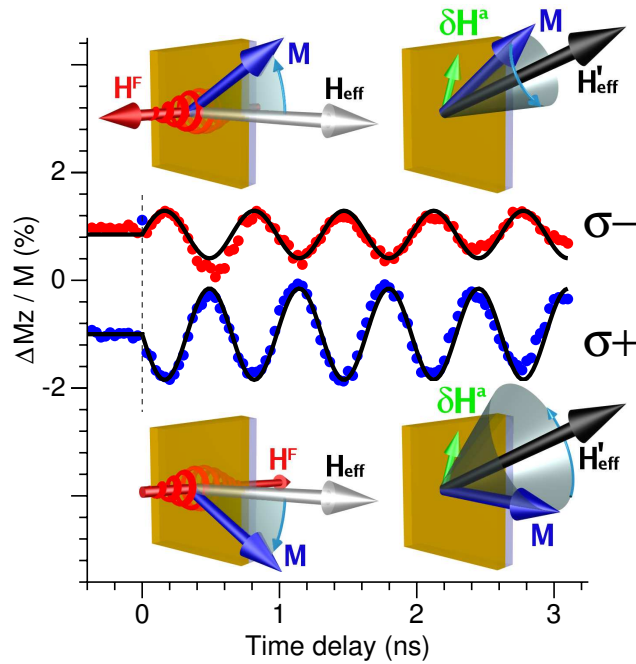


Figure 6.8: Precession following excitation with circularly polarized light. The two helicities σ^+ and σ^- give rise to precession with an opposite phase and a different amplitude. During the 100 fs presence of the laser pulse the magnetization precesses in the dominating axial magnetic field \mathbf{H}_F created by the circularly polarized pump pulse. Subsequent precession takes place in the effective magnetic field $\mathbf{H}'_{\text{eff}} = \mathbf{H}_{\text{eff}} + \delta\mathbf{H}^a$.

In order to understand this result and the mechanism of excitation we analyze our model of the photoinduced anisotropy [Eq. (6.5)] for circularly polarized light $\mathbf{E} = \frac{E_0}{\sqrt{2}}(\hat{x} + i\hat{y})$.

$$\delta H_x^a \propto AE_0^2 M_s \sin \zeta \cos \phi \quad (6.14)$$

$$\delta H_y^a \propto -AE_0^2 M_s \sin \zeta \sin \phi \quad (6.15)$$

$$\delta H_z^a \propto DE_0^2 M_s \cos \zeta \quad (6.16)$$

We find that a photoinduced $\delta \mathbf{H}^a$ may still exist which only depends on the direction ϕ of \mathbf{M} with respect to the crystal axes. This is reasonable as θ has no meaning for circularly polarized light. For in-plane magnetization the photoinduced $\delta \mathbf{H}^a$ is parallel to the film plane. However, it does not depend on the helicity of light and can therefore not account for the opposite phase of precession induced by the light of opposite helicities. Hence, a different effect is needed in order to explain the experimental observations, and the effect that we are seeking should be odd with respect to the helicity of light.

Our experimental observations can be understood if during the presence of the laser pulse a strong magnetic field along the \mathbf{k} -vector of light is created. Such an axial magnetic field \mathbf{H}^F can be generated by intense circularly polarized light through what is known as the inverse Faraday effect [22, 23, 24, 25] (see below). In our experiment these optically generated field pulses are much stronger than both anisotropy \mathbf{H}_a and the applied field \mathbf{H}_{ext} and therefore completely dominate during the $\Delta t = 100$ fs presence of the laser pulse. The magnetization responds by precessing in the plane of the film (normal to \mathbf{H}^F) to a new in-plane orientation. After the pulse is gone, the magnetization will precess in the effective in-plane field $\mathbf{H}'_{\text{eff}} = \mathbf{H}_{\text{ext}} + \mathbf{H}_a + \delta \mathbf{H}^a$, as illustrated in Fig. 6.8.

The strength of the photoinduced field \mathbf{H}^F can be estimated from the precession amplitude Λ :

$$H^F \approx \frac{\omega}{\gamma} \approx \frac{\Lambda}{\gamma \Delta t_{\text{pulse}}} \quad (6.17)$$

where ω is the precession frequency, γ is the gyromagnetic ratio and Δt_{pulse} is the duration of the optical pulse. We find that laser pulses of energy $20 \mu\text{J}$ create transient magnetic field pulses of about 0.6 T in the garnet films.

An important conclusion can be drawn from the experimental results presented in Fig. 6.8. It can be seen that during the action of the laser pulse the magnetization remains in the plane of the sample. Therefore, this laser excitation of the magnetization is not accompanied by a change of the polarization of the laser pulse. This means that during this opto-magnetic interaction process the angular momentum of the photon is conserved.

The asymmetry seen in the signal amplitude between the σ^+ and σ^- helicities stems from the simultaneously created photoinduced anisotropy $\delta \mathbf{H}^a$ which is inde-

pendent of the pump helicity (see Fig. 6.8). For the σ^- helicity, \mathbf{M} precesses in the direction of the optically modified effective field \mathbf{H}'_{eff} during the presence of \mathbf{H}^{F} . This gives rise to a precession with a small amplitude around \mathbf{H}'_{eff} after the pulse is gone. For the σ^+ helicity \mathbf{M} precesses in the opposite direction during the presence of \mathbf{H}^{F} , moving further away from \mathbf{H}'_{eff} . After the pulse is gone a large amplitude precession takes place.

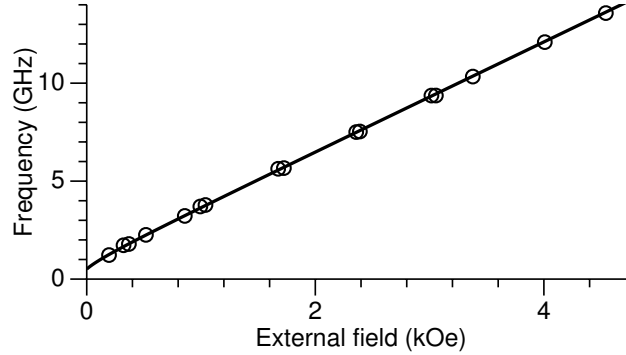


Figure 6.9: Precession frequency as function of the externally applied magnetic field. Circles represent measurements and the solid line is a best fit using $4\pi M_s = 550$ G and $H^a = 50$ Oe.

The consistently large amplitude precession triggered by σ^+ polarized pump pulses, irrespective of the applied field strength \mathbf{H}_{ext} , allows the external field dependence of the precession frequency $\omega(H_{\text{ext}})$ to be accurately determined from the experimental data. As will be discussed in Sect. 6.3.3, this is not the case for σ^- polarized excitation, which under certain conditions does not trigger any precession (see Fig. 6.13). The precession frequency is given by the Kittel formula [26] and can, for our geometry, be expressed as

$$\begin{aligned} \omega &= \gamma \sqrt{BH} \\ &= \gamma \sqrt{(4\pi M_s + H'_a + H_{\text{ext}})(H'_a + H_{\text{ext}})}, \end{aligned} \quad (6.18)$$

where the small photoinduced modification δH^a of the anisotropy field has been included in $H'_a = H_a + \delta H^a$. Figure 6.9 shows the measured ω as a function of the applied magnetic field for the σ^+ polarized pump excitation. The solid line represents a best fit using Eq. (6.18) and gives an H_a of about 50 Oe, in accordance with the results of Fig. 6.2.

Double-pump coherent magnetization control

Ultrafast coherent control of the magnetization can be achieved by using multiple laser pulses in rapid succession. In a double pump experiment employing two circularly polarized pump pulses with opposite helicity and almost equal power, we achieved stopping of the precessional dynamics as well as doubling of the amplitude. As already described in the case of linearly polarized pulses, we operate at a fixed time-delay between the two pump pulses, and adjust the frequency of precession by an external magnetic field in order to vary the arrival time of the second pump pulse with respect to the phase of the already present precession.

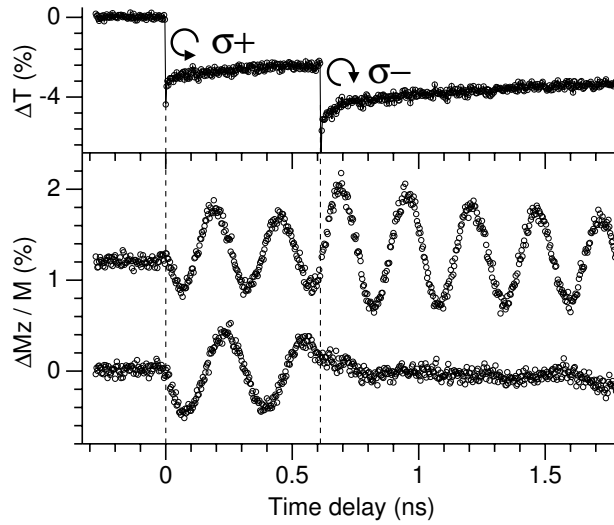


Figure 6.10: Double pump experiment with circularly polarized laser pulses of opposite helicity and $15 \mu\text{J}$ pulse power. The upper panel shows the pump-induced change of the sample transmittivity due to the photoexcitation of impurities. The lower panel shows how amplification and complete stopping of the magnetization precession can be achieved depending on the phase of the precession when the second laser pulse arrives. The time delay between the two pump pulses is fixed at approximately 0.6 ns, and the precession frequency is controlled by varying the external field.

In Fig. 6.10 it is shown how a pump pulse of helicity σ^+ arriving at $t = 0$ triggers precession of the magnetization, as explained in the previous section. A second pump pulse of helicity σ^- arriving after an odd number of half precessional periods rotates the magnetization further away from \mathbf{H}_{eff} causing the subsequent precession to have almost twice the amplitude. If, however, this second pump pulse arrives after an

integer number of full periods, the magnetization is rotated back into its original equilibrium orientation along \mathbf{H}_{eff} and no further precession takes place. Figure 6.11 gives a pictorial illustration of these two situations.

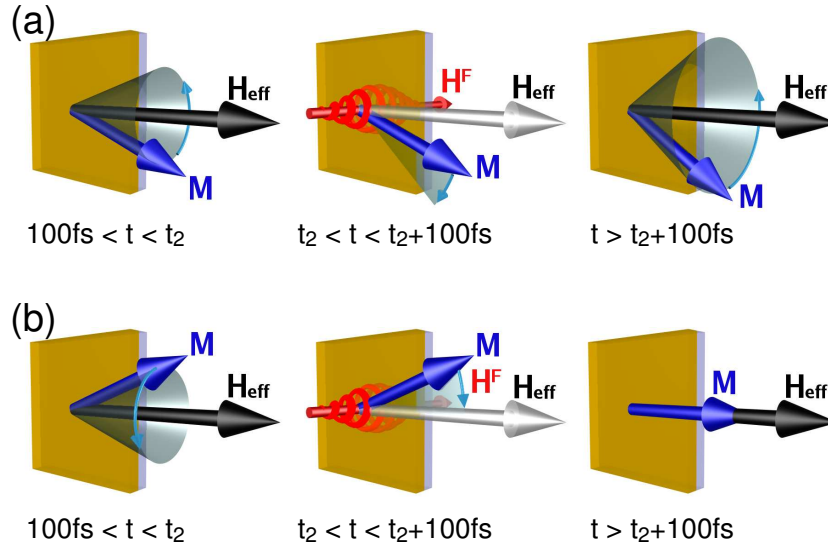


Figure 6.11: Illustration of the double pump experiment for circularly polarized pump pulses of opposite helicity arriving at an (a) odd number of half precessional periods and (b) an integer number of full precessional periods. The magnetization is either rotated further away from the effective field direction causing subsequent precession to take place with almost twice the original amplitude, or the magnetization is rotated back into the effective field direction and no further precession takes place.

This experiment clearly demonstrates that femtosecond optical pulses can be used to directly and coherently control spin dynamics. Depending on the phase of the precession when the second pulse arrives, energy is either transferred from the laser pulse to the magnetic system (amplification of the precession) or from the magnetic excitation to the optical pulse (stopping of the precession). A stimulated Raman process of scattering on magnons is believed to be responsible for the inverse Faraday effect [27] (see below), and we expect that further support for this mechanism can be found in the frequency spectrum of the second pump pulse. Stokes or anti-Stokes peaks should be observable in the spectrum, depending on whether the precession is amplified or stopped, respectively. In view of the low intrinsic damping in these garnet films, and therefore the long lifetime of magnetic excitations, it is remarkable

how ultrashort laser pulses can completely stop the long period coherent precession of spins instantaneously by transfer of the energy into the optical pulse.

It should be pointed out that the present double pump experiment, which demonstrates control of the magnetization in ferrimagnetic garnets, is considerably different from those previously reported in diamagnetic and paramagnetic materials. During the past two decades a great number of publications have been devoted to the photoexcitation of a nonequilibrium spin polarization in direct band gap semiconductors through the phenomena of optical orientation [28, 29, 30]. In these materials, absorption of circularly polarized photons may lead to a nonequilibrium population of spin polarized electrons and holes in the conduction band and valence band, respectively. In paramagnetic semiconductors these spin polarized carriers can cause partial alignment of the moments of magnetic ions due to a *sp-d* exchange interaction, and thereby also affect their precession in a magnetic field [31]. Using this phenomena of optical orientation Akimoto *et al.* [32] have demonstrated control of the precession of Mn^{2+} -moments in $\text{CdTe}/\text{Cd}_{1-x}\text{Mn}_x\text{Te}$ quantum wells. Note that this approach, in contrast to our experiment, is based on the absorption of photons. A nonabsorptive mechanism for manipulation of spins in $\text{Zn}_{1-x}\text{Cd}_x\text{Se}$ quantum well structures was reported by Gupta *et al.* [33], who used below band gap optical pulses to control the spin precession of photoexcited electrons in the conduction band via the optical Stark effect. However, these experiments were performed on paramagnetic materials, while in the present case we have succeeded to control the collective motion of the strongly coupled spins in a magnetically ordered compound. Additionally, the experimental conditions differ strongly in the two cases: control of the spin precession in paramagnetic semiconductors requires very low temperatures, typically below 10 K, and strong magnetic fields of several Teslas. In strong contrast, the optical control of magnetization that we report here was done at room temperature and in magnetic fields well below 1 kOe.

Phenomenological model of the inverse Faraday effect

The normal magneto-optical Faraday effect can be viewed as due to a difference in the refractive indices for the two circularly polarized eigenmodes of light propagating in a magnetized medium. The inverse process, where circularly polarized light creates a magnetization or an effective magnetic field is also possible [23, 24, 25] and known as the inverse Faraday effect. Strictly speaking this effect is classified as a *optomagnetic* effect as it does not rely on absorption [34]. Phenomenologically the creation of an axial magnetic field by circularly polarized light can be described as

$$\delta H_i^{\text{F}}(0) = \chi_{ijk}[E_j(\omega)E_k^*(\omega) - E_k(\omega)E_j^*(\omega)], \quad (6.19)$$

where χ_{ijk} is a third rank axial tensor with nonzero components for crystals of any symmetry [12]. The magnetic field is created by elliptically or circularly polarized

light along its \mathbf{k} -vector. The field changes sign when the circular polarization is changed from left-handed to right-handed. The effect does not rely on absorption but becomes possible due to strong spin-orbit coupling in a material. The optically induced magnetic field pulse appears to act only during the presence of the laser pulse in the material [25]. Its strength depends on the value of the relevant χ_{ijk} components and is directly related to the Verdet constant. For our garnet films we can estimate the optically induced effective field strength from the resulting precession dynamics. At the wavelength of 805 nm used in our experiments we find $H^F \approx 0.6$ T for a pump irradiance of about 10^{11} W/cm².

Microscopic model of the inverse Faraday effect

In this section we discuss a possible microscopic mechanism for the creation of an axial magnetic field by light and argue that it can be both efficient and ultrafast.

In the electric dipole approximation an optical transition cannot change the spin state of an electron. After electric dipole transitions the next most likely type of transition is a magnetic dipole transition, which is due to the interaction between the electron spin and the oscillating magnetic field of the incident electromagnetic radiation. Magnetic dipole transitions allow spin flip but typically are about 10^5 times less probable than similar electric dipole transitions. The strong effect that we see indicates a mechanism that allows change of the electron spin with higher efficiency than expected from a magnetic dipole transition. Moreover, the mechanism should not rely on material properties specific to garnets, as the reported effect has also been shown to exist in other magnetic materials such as rare earth orthoferrites [25] and metallic alloys [35].

A stimulated Raman-like coherent optical scattering process has been suggested to account for both the speed and the efficiency of the excitation [23, 25, 27, 36]. Two frequency components of electromagnetic radiation, both present in the 100-fs-wide laser pulse take part in the process (see Fig. 6.12). The frequency ω_1 stimulates an optical transition from the ground state $|1\rangle$ to a virtual state with a strong spin-orbit interaction. Due to this strong spin-orbit coupling there is a large probability of flipping the electron spin. Radiation at the frequency ω_2 also present in the optical pulse, stimulates the relaxation back into the spin split ground state with the electron spin reversed. The relaxation is accompanied by the coherent emission of a photon of energy $\hbar(\omega_1 - \Omega_m)$ and the creation of a magnon of energy Ω_m . This process can be much more efficient than a simple magnetic dipole transition as it is coherently stimulated by radiation at a frequency of ω_2 present in the laser pulse. Moreover, as the energy of the virtual state is of the order of the photon energy $E = \hbar\omega = 1.54$ eV the transition can be fast, of the order of $\tau \sim \hbar/E \sim 3$ fs. Because the effect does not depend on optical absorption, it is classified as a *optomagnetic* effect [34].

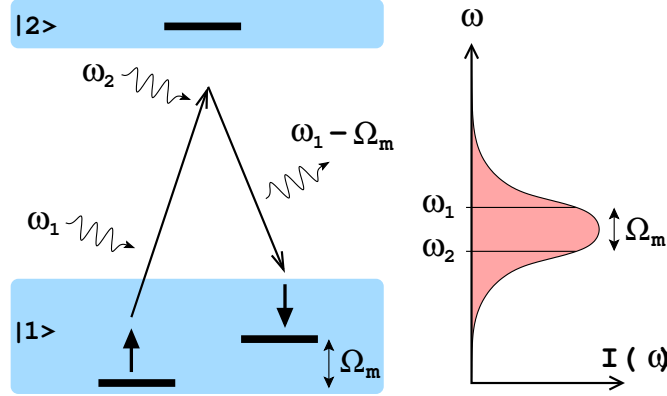


Figure 6.12: Illustration of the stimulated Raman-like coherent scattering mechanism believed to be responsible for the ultrafast optically generated magnetic field. Two frequency components of electromagnetic radiation from the spectrally broad laser pulse take part in the process. The frequency ω_1 causes a transition into a virtual state with strong spin-orbit coupling. Radiation at the frequency ω_2 stimulates the relaxation back to the ground state with the creation of a magnon.

6.3.3 Single-pump ultrafast photomagnetic switching

A proper combination of the inverse Faraday effect and the photoinduced anisotropy allows for an interesting demonstration of photomagnetic switching on the femtosecond time scale [37]. Because the direction of $\delta\mathbf{H}^a$ depends only on the initial angle ϕ of the magnetization with respect to the crystal axes, it can be tuned by rotating the sample with respect to the applied field. We have verified experimentally that this is the case. Alternatively, since the initial equilibrium of \mathbf{M} is along \mathbf{H}_{eff} , which is determined by the balance between the magnetocrystalline anisotropy field \mathbf{H}_a and the externally applied field \mathbf{H}_{ext} , it can also be tuned simply by varying the strength of the applied field.

In Fig. 6.13 the coherent precession of the magnetization following excitation with pulses of helicity σ^- and σ^+ is shown for different values of \mathbf{H}_{ext} . The amplitude of precession is consistently larger in the case of σ^+ , as during $0 < t < 100$ fs, \mathbf{M} precesses away from the new equilibrium created by $\delta\mathbf{H}^a$, as explained above in Sect. 6.3.2. For pulses of helicity σ^- , this precession is towards the new equilibrium, leading to smaller precessional amplitude in the time after the pulse. With an applied field of $|\mathbf{H}_{\text{ext}}| \approx 150$ Oe, no precession is triggered due to a perfect balance of two effects: The in-plane precession of the magnetization during the 100 fs magnetic field pulse $\delta\mathbf{H}^F$ brings the magnetization exactly to its new equilibrium orientation created by

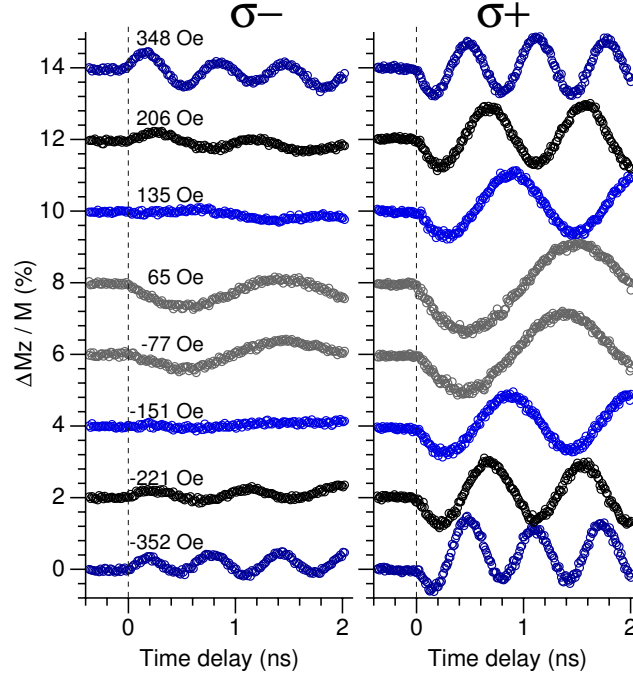


Figure 6.13: Precession of the magnetization triggered by left- and right-handed circularly polarized laser pulses at different values of the in-plane applied magnetic field. For the σ^- helicity, at an applied field of $\sim \pm 150$ Oe, no precession is observed due to a perfect balance of the two photomagnetic effects $\delta\mathbf{H}^a$ and \mathbf{H}^F .

the optically modified anisotropy field. It remains stable in this orientation until the anisotropy field relaxes back to its original state, i.e. for several nanoseconds. An illustration of this switching process is shown in Fig. 6.14.

Note also that for the σ^- helicity at weak applied fields the precession has an opposite phase compared to the precession in stronger applied fields, and that this phase is the same as for the precession triggered by the σ^+ pulses. At weak fields the direction of the photoinduced $\delta\mathbf{H}^a$ is such that the precession of \mathbf{M} in \mathbf{H}^F during the optical pulse is not sufficient to bring it into the direction of \mathbf{H}'_{eff} . At stronger fields, however, $\delta\mathbf{H}^a$ is in a different direction producing a \mathbf{H}'_{eff} that is less inclined with respect to the original effective field. During the presence of \mathbf{H}^F the magnetization now precesses past the direction of \mathbf{H}'_{eff} , and therefore with the opposite phase in the time after the laser pulse.

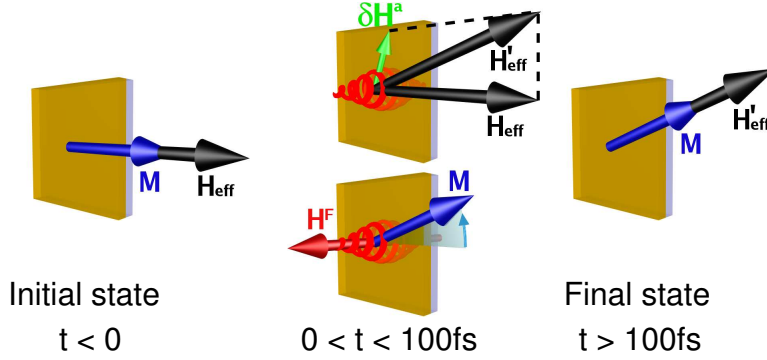


Figure 6.14: Illustration of the switching process. Initially at $t < 0$ the magnetization is along \mathbf{H}_{eff} . During the presence of the laser pulse $0 < t < 100$ fs photo induced modification of the anisotropy fields leads to a new long-lived equilibrium along \mathbf{H}'_{eff} . Simultaneously, the strong optically generated field \mathbf{H}^F causes the magnetization to precess into the new state. After $t > 100$ fs, the optical pulse is gone and the approximately 0.6° switching of \mathbf{M} is complete.

6.3.4 Temperature dependence

The experiments described so far were all done at room temperature and mostly in the in-plane applied field geometry, where thermal effects of the laser excitation would not be clearly visible even if it were present. In a tilted field geometry ($\zeta < 90^\circ$) the measured signal is more sensitive to thermal effects of the laser pumping, as the equilibrium orientation of \mathbf{M} is determined by both the anisotropy field and the magnitude of \mathbf{M} . A thermal influence on any of these would cause a new equilibrium orientation for \mathbf{M} and thus trigger precessional dynamics or spin reorientation.

The phonon-magnon interaction time in dielectric materials is typically of the order of a nanosecond [38]. Heating can therefore not account for the ultrafast (< 1 ps) excitation of coherent spin waves that we have shown. However, thermal effects induced by the laser pulses may still be present but on a longer time scale.

In our experiment, the Faraday rotation of the probe pulses is proportional to M_z . For magnetization in the film plane ($\zeta = 90^\circ$) this means that the measured signal is proportional to the magnetization $M(T)$ at any given temperature. In a tilted field geometry ($\zeta < 90^\circ$) the signal is not simply proportional to $M(T)$ but to $M_z(T)$ which is given by the balance $\mathbf{M} \times \mathbf{H}_{\text{eff}} = 0$ in the effective magnetic field, $\mathbf{H}_{\text{eff}} = -4\pi M_z \hat{\mathbf{z}} + \mathbf{H}_a + \mathbf{H}_{\text{ext}}$.

In order to investigate the thermal effects the sample was mounted on a temperature controlled sample holder and laser-induced magnetization dynamics was studied

at temperatures from $T=300$ K to $T=410$ K. In Fig. 6.15 it is shown how the precession frequency depends on the sample temperature with an applied field \mathbf{H}_{ext} of about 250 Oe in the sample plane. The solid line represents a fit using Eq. (6.18) with $|\mathbf{H}_a| \propto M^2(T)$ assumed to be the temperature dependence of the magnetocrystalline anisotropy. This is in good agreement with the measured precession frequencies.

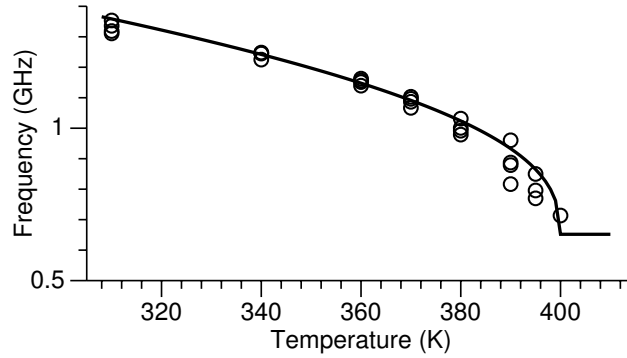


Figure 6.15: Precession frequency as a function of the temperature for an in-plane applied magnetic field of about 250 Oe and σ^- polarized excitation. The symbols represent measurements and the solid line the theoretical prediction with anisotropy $H_a = 50$ Oe and an assumed temperature dependence for H_a like $M(T)^2$.

The precession amplitude was measured as a function of temperature for both the linear and circular polarization of the pump laser. The results are shown in Fig. 6.16. When excited with linearly polarized light, the precession amplitude drops quickly with temperature and is no longer visible at 380 K, implying that the efficiency of the photoinduced anisotropy $\delta\mathbf{H}^a$ is strongly temperature dependent. This observation is in qualitative agreement with the temperature dependence of the density of photo-produced charges in garnets [39], a process necessary for the light-induced change of magnetic anisotropy.

In contrast, the amplitude of the precession excited with circularly polarized light has a very different dependence on T . It also appears to behave differently for the two helicities σ^+ and σ^- . As described in the previous section, the difference in amplitude between σ^+ and σ^- stems from the contribution by $\delta\mathbf{H}^a$, whose temperature dependence is shown in panel (a). The effect of photoinduced anisotropy $\delta\mathbf{H}^a$ can be eliminated by averaging the curves for σ^+ and σ^- . The resulting average values fit well to a scaled $M(T)$ curve [see panel (c)]. Note that the measured signal amplitude in this geometry is expected to be proportional to $M(T)$ and that this result therefore implies that the inverse Faraday effect \mathbf{H}^F is independent of \mathbf{M} , in accordance with

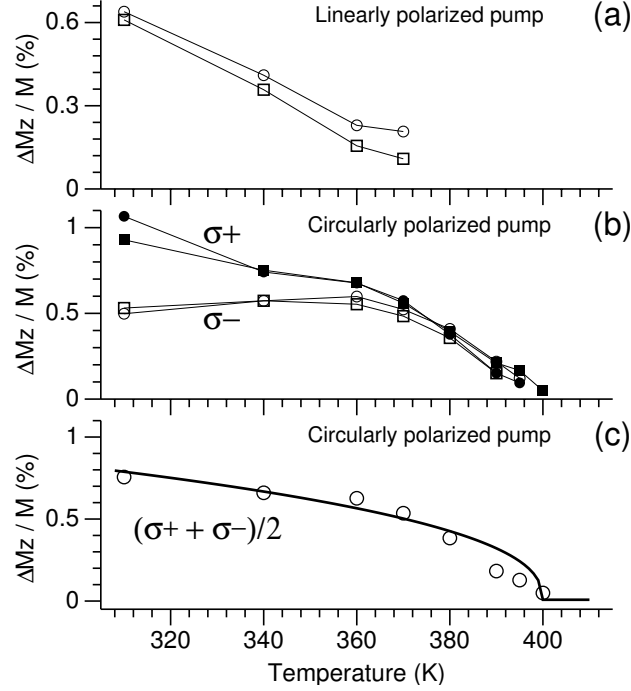


Figure 6.16: Amplitude of the precession triggered by (a) linearly polarized pump pulses and (b) circularly polarized pulses of helicity σ^+ and σ^- . (c) The average of the σ^+ and σ^- amplitudes from (b) which eliminates the contribution from δH^a . This averaged amplitude follows an $M(T)$ temperature dependence, implying that \mathbf{H}^F is independent of \mathbf{M} .

the phenomenological description given in Eq. (6.19).

In order to determine the amount of heating caused by a single pump pulse and to estimate the phonon-magnon interaction time, the laser-induced magnetization dynamics was studied in a tilted field geometry ($\zeta < 90^\circ$) at different temperatures. The results are shown in Fig. 6.17. In panel (a) the time traces of the precession are shown for sample temperatures from 310 up to 410 K. As the temperature approaches the Curie point T_C , the amplitude of precession decreases and an exponential background appears. This is the thermal destruction of the magnetic order induced by the laser heating. The time constant is of the order of a nanosecond and determined by the phonon-magnon interaction time [38].

From the time traces in Fig. 6.17(a) the slope of the exponential background

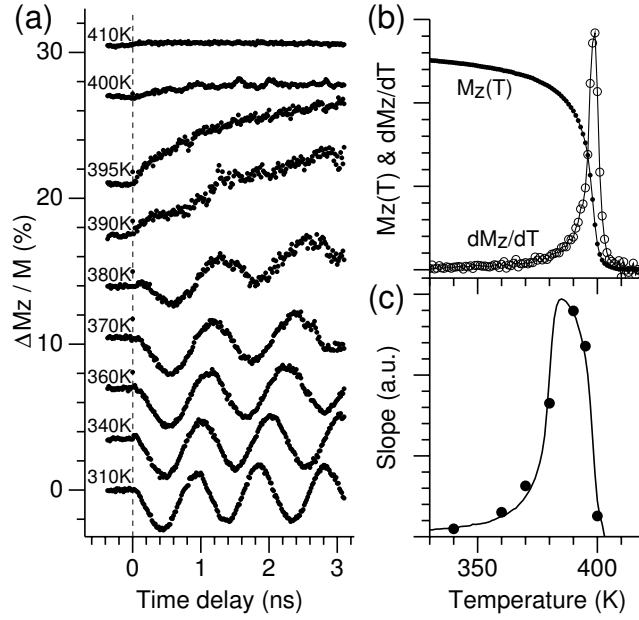


Figure 6.17: (a) Precessional dynamics at different temperatures for an applied field $H_{\text{ext}} = 300$ Oe at an angle of about 45° . (b) The z component of the magnetization (proportional to the Faraday rotation) and its temperature derivative as function of the sample temperature. (c) The measured slope of the exponential relaxation of \mathbf{M} as a function of temperature. The solid line represents a best fit.

was extracted. This is shown in panel 6.17(c) as a function of the temperature. The solid line is the function $M_z(T + \Delta T) - M_z(T)$ with $M_z(T)$ taken from the measurements shown in panel 6.17(b). A best fit is obtained for a pump-induced temperature increase $\Delta T = 18$ K caused by a laser irradiance of about 10^{11} W/cm². When measuring at a repetition rate of 500 Hz there is no static overheating of the sample. This has been verified by measuring magnetization curves $M(T)$ with and without the presence of pump pulses.

Another point that deserves to be addressed is the significant increase of signal noise seen in the time traces at temperatures from 370 K to $T_C = 400$ K. Already at 370 K and 380 K near the end of the time traces the noise level starts to increase as heating induced by the laser pulse reaches the magnetic system. Even more pronounced levels of noise can be seen at temperatures closer to the Curie point. This noise is due to the thermal fluctuations in the magnetic system. When studied with

our stroboscopic measurement technique that averages every data point over several excitation events, the fluctuations show up as random noise in the signal [40]. As we approach the critical temperature the fluctuations strongly increase and then drop markedly above T_C , where the magnetic order is completely destroyed. The observed behavior of the noise confirms that we are indeed probing the magnetic system.

6.4 Conclusion

In conclusion, we have shown that the magnetization in garnet films can be directly and coherently controlled on the femtosecond time scale using ultrashort laser pulses. Two distinct nonthermal photomagnetic effects that facilitate such control have been identified. A long-lived photoinduced magnetic anisotropy field can be created by both linearly and circularly polarized laser pulses, and strong transient magnetic field pulses can be generated by circularly polarized light. Applying a small external field allows for the careful timing and balancing of these two effects, thus making complete nonthermal and coherent control of the magnetization possible. Thermal effects were only seen near T_C . They are slow due to a phonon-magnon interaction time of the order of a nanosecond, and can easily be distinguished from the ultrafast nonthermal processes. The reported effects open new and exciting possibilities for ultrafast manipulation of magnetization by light.

References

- [1] L. Landau and E. Lifshitz, *Phys. Z. Union.* **8**, 153 (1935).
- [2] E. Beaurepaire, J.-C. Merle, A. Daunois, and J.-Y. Bigot, *Phys. Rev. Lett.* **76**, 4250 (1996).
- [3] M. van Kampen, C. Jozsa, J. T. Kohlhepp, P. LeClair, L. Lagae, W. J. M. de Jonge, and B. Koopmans, *Phys. Rev. Lett.* **88**, 227201 (2002).
- [4] B. B. Krichevtskov, V. V. Pavlov, and R. V. Pisarev, *Zh. Eksp. Teor. Fiz.* **49**, 466 (1989), [*JETP Lett.* **49**, 535 (1989)].
- [5] R. V. Pisarev, B. B. Krichevtskov, V. N. Gridnev, V. P. Klin, D. Fröhlich, and C. Pahlke-Lerch, *J. Phys.: Condens. Matter* **5**, 8621 (1993).
- [6] F. Hansteen, O. Hunderi, T. H. Johansen, A. Kirilyuk, and Th. Rasing, *Phys. Rev. B* **70**, 094408 (2004).
- [7] A. Tsukamoto, K. Nakagawa, A. Itoh, A. Kimel, A. Tsvetkov, H. A. N. Ohta, A. Kirilyuk, and Th. Rasing, *IEEE Trans. Magn.* **40**, 2543 (2004).

-
- [8] A. Paoletti, ed., *Physics of Magnetic Garnets*, Enrico Fermi International School of Physics, Italian Physical Society (North-Holland Publishing Co., 1978).
 - [9] G. Winkler, *Magnetic Garnets* (Friedr. Vieweg & Sohn, Braunschweig, Germany, 1981).
 - [10] Y. R. Shen, *The Principles of Nonlinear Optics* (Wiley, New York, 1984).
 - [11] T. H. O'Dell, *The Electrodynamics of Magneto-electric Media* (North-Holland Publishing Company, Amsterdam, 1970).
 - [12] R. R. Birss, *Symmetry and Magnetism*, Series of monographs on selected topics in solid state physics (North-Holland Publishing Company, Amsterdam, 1966), 2nd ed.
 - [13] V. V. Pavlov, R. V. Pisarev, A. Kirilyuk, and Th. Rasing, Phys. Rev. Lett. **78**, 2004 (1997).
 - [14] R. W. Teale and D. W. Temple, Phys. Rev. Lett. **19**, 904 (1967).
 - [15] J. F. Dillon, E. M. Gyorgy, and J. P. Remeika, Phys. Rev. Lett. **22**, 643 (1969).
 - [16] A. B. Chizhik, I. I. Davidenko, A. Maziewski, and A. Stupakiewicz, Phys. Rev. B **57**, 14366 (1998).
 - [17] A. Stupakiewicz, A. Maziewski, I. Davidenko, and V. Zablotskii, Phys. Rev. B **64**, 064405 (2001).
 - [18] R. Alben, E. M. Gyorgy, J. F. Dillon, and J. P. Remeika, Phys. Rev. B **5**, 2560 (1972).
 - [19] V. G. Veselago, R. A. Doroshenko, and S. G. Rudov, Zh. Eksp. Teor. Fiz. **105**, 638 (1994), [JETP **78**, 341 (1994)].
 - [20] R. Metselaar, M. A. H. Huyberts, and H. Logmans, J. Appl. Phys. **46**, 7326 (1975).
 - [21] V. V. Eremenko, S. L. Gnatchenko, I. S. Kachur, V. G. Piryatinskaya, A. M. Ratner, and V. V. Shapiro, Phys. Rev. B **61**, 10670 (2000).
 - [22] L. P. Pitaevskii, Sov. Phys. JETP **12**, 1008 (1961).
 - [23] P. S. Pershan, J. P. van der Ziel, and L. D. Malmstrom, Phys. Rev. **143**, 574 (1966).
 - [24] J. P. van der Ziel, P. S. Pershan, and L. D. Malmstrom, Phys. Rev. Lett. **15**, 190 (1965).

- [25] A. V. Kimel, A. Kirilyuk, P. A. Usachev, R. V. Pisarev, A. M. Balbashov, and Th. Rasing, *Nature* **435**, 655 (2005).
- [26] C. Kittel, *Phys. Rev.* **73**, 155 (1948).
- [27] Y. R. Shen and N. Bloembergen, *Phys. Rev.* **143**, 372 (1966).
- [28] F. Meier and B. P. Zakharchenya, eds., *Optical Orientation*, vol. 8 of *Modern Problems in Condensed Matter Sciences* (North-Holland, Amsterdam, 1984), ISBN 0-444-86741-4.
- [29] D. D. Awschalom, J. Warnock, and S. von Molnár, *Phys. Rev. Lett.* **58**, 812 (1987).
- [30] I. Zutic, J. Fabian, and S. Das Sarma, *Rev. Mod. Phys.* **76**, 323 (2004).
- [31] J. K. Furdyna and J. Kossut, eds., *Diluted Magnetic Semiconductors*, vol. 25 of *Semiconductors and Semimetals* (Academic Press, New York, 1988), ISBN 0-12-752125-9.
- [32] R. Akimoto, K. Ando, F. Sasaki, S. Kobayashi, and T. Tani, *J. Appl. Phys.* **84**, 6318 (1998).
- [33] J. A. Gupta, R. Knobel, N. Samarth, and D. D. Awschalom, *Science* **292**, 2458 (2001).
- [34] A. F. Kabychenkov, *Zh. Eksp. Teor. Fiz.* **100**, 1219 (1991), [*JETP* **73**, 672 (1991)].
- [35] Recently we have managed to suppress this dominating thermal effect in GdFeCo and to observe true non-thermal effects. (in preparation).
- [36] R. Gómez-Abal, O. Ney, K. Satitkovitchai, and W. Hübner, *Phys. Rev. Lett.* **92**, 227402 (2004).
- [37] F. Hansteen, A. V. Kimel, A. Kirilyuk, and Th. Rasing, *Phys. Rev. Lett.* **95**, 047402 (2005).
- [38] A. V. Kimel, R. V. Pisarev, J. Hohlfeld, and Th. Rasing, *Phys. Rev. Lett.* **89**, 287401 (2002).
- [39] V. V. Eremenko, S. L. Gnatchenko, I. S. Kachur, V. G. Piryatinskaya, A. M. Ratner, M. B. Kosmyna, B. P. Nazarenko, and V. M. Puzikov, *J. Phys.: Condens. Matter* **15**, 4025 (2003).
- [40] M. R. Freeman, G. M. Steeves, G. E. Ballentine, and A. Krichevsky, *J. Appl. Phys.* **91**, 7326 (2002).

Summary

In magnetic storage devices, such as hard disks, bits of information are encoded in the local magnetization direction of small areas on a disk of magnetic material. High speed data writing requires the ability to switch the magnetization of a bit from one direction to the opposite in an extremely short time. With present-day technology this can be done in about one nanosecond (10^{-9} s), however, computer CPUs are getting faster and increasing amounts of digital information is being produced. Therefore, in order for magnetic data storage technology to keep up, new and faster methods for controlling magnetization must be found.

Modern laser sources can produce extremely intense and *ultrashort* pulses of light, shorter than 100 femtoseconds (10^{-13} s). If these could be used for the manipulation of the magnetization, it could potentially lead to a ten-thousand-fold improvement of the switching speed in magnetic storage devices. The challenge, however, is to find physical mechanisms that enable such control of magnetization by light.

Recent research has shown that the heating caused by the absorption of an ultrashort laser pulse in a metallic magnetic material can destroy its magnetization surprisingly fast. However, this demagnetization is essentially caused by a rapid temperature increase, and therefore it provides only limited freedom for manipulation of magnetization by light alone. In this thesis, novel mechanisms for optical control of magnetization have been explored in magnetic garnet crystals. It has been found that in these materials ultrashort laser pulses can do much more than simply destroy the magnetic ordering through heating effects: Linearly polarized laser pulses can modify the internal anisotropy fields of this dielectric crystal by inducing an effective charge transfer between iron ions in different crystallographic sites. This can be used to create a new long-lived equilibrium direction for the magnetization. Circularly polarized

laser pulses additionally are demonstrated to act as strong magnetic field pulses due to the inverse Faraday effect, and can thus be used to directly control the magnetization. These two new *ultrafast* and *nonthermal* mechanisms open new and exciting possibilities for ultrafast control of magnetization by light. Examples of such control shown in this thesis include all-optical switching on the femtosecond timescale, and coherent optical control of the precessional dynamics with circularly polarized laser pulses.

Samenvatting

Bij magnetische informatie opslag, zoals in harde schijven, worden informatie bits gecodeerd door kleine gebieden op de schijf in hun locale voorkeursrichting (noord of zuid) te magnetiseren. Het schrijven van informatie met hoge snelheid vereist dus de mogelijkheid om de magnetisatie-richting van een bit te veranderen in extreem korte tijd. Met de huidige technologie kan dit gerealiseerd worden in ongeveer een nanoseconde (een miljardste deel van een seconde). Echter, computer processoren worden steeds sneller en de hoeveelheid geproduceerde informatie wordt ook alsmaar groter. Daarom moeten er nieuwe en snellere methodes voor de controle van de magnetisatie gevonden worden, zodat de magnetische dataopslag technologie bij kan blijven met deze ontwikkelingen.

Moderne laserbronnen kunnen extreem intense en *ultrakorte* lichtpulsen produceren, korter dan 100 femtoseconde (10^{-13} s). Wanneer deze lichtpulsen gebruikt kunnen worden voor de manipulatie van de magnetisatie, dan zou dit in potentie kunnen leiden tot een tienduizendvoudige verbetering in de schakelsnelheid van magnetische opslag apparatuur. De uitdaging is echter een fysische mechanisme te vinden, dat een dergelijke optische controle van de magnetisatie toestaat.

Recent onderzoek heeft laten zien dat de verwarming, veroorzaakt door de absorptie van een ultrakorte laserpuls in een magnetisch materiaal, verrassend snel de magnetisatie kan vernietigen. Deze demagnetisatie wordt echter veroorzaakt door een snelle temperatuursverhoging van het materiaal, welke altijd gevolgd wordt door een relatief langzame afkoeling, en biedt daarom slechts gelimiteerde vrijheid voor de manipulatie van de magnetisatie door licht alleen. In dit proefschrift zijn nieuwe mechanismen onderzocht voor de optische controle van de magnetisatie in magnetische granaat kristallen. Een van de bevindingen is, dat in dit materiaal ultrakorte

laserpulsen veel meer kunnen doen dan de simpele vernietiging van de magnetische ordening door verwarmingseffecten: Lineair gepolariseerde laserpulsen veranderen de interne magnetische anisotropievelden van dit dielektrische kristal doordat ze een effectieve verplaatsing van elektronen tussen ijzerionen op verschillende kristalografische plaatsen teweeg brengen. Dit kan gebruikt worden om een nieuwe langdurige evenwichtstoestand van de magnetisatie richting te creëren. Bovendien is aangetoond dat circulair gepolariseerde laserpulsen als sterke magnetische pulsen werken ten gevolge van het inverse Faraday effect. Zulke pulsen kunnen op die manier gebruikt worden om de magnetisatie direct te controleren. Deze beide nieuwe *ultrasnelle* en *niet-thermische* mechanismen openen nieuwe en opwindende mogelijkheden voor de controle van de magnetisatie door licht op een zeer korte tijdschaal. Voorbeelden van deze controle, welke worden beschreven in dit proefschrift, zijn de volledig optische schakeling van de magnetisatie tussen twee evenwichtstoestanden op femtoseconde tijdschaal, en de coherente optische controle van de precessie dynamica met circulair gepolariseerde laserpulsen.

List of Publications

- [1] A. V. Kimel, A. Kirilyuk, F. Hansteen, R. V. Pisarev, and Th. Rasing, “Non-thermal optical control of magnetism and ultrafast laser-induced spin dynamics in solids (review).” (Submitted to *J. Phys.: Condens. Matter*).
- [2] A. Kirilyuk, A. V. Kimel, F. Hansteen, R. V. Pisarev, and Th. Rasing, “Ultrafast all-optical control of the magnetization in magnetic dielectrics (review).” (Submitted to *Low Temp. Phys.*).
- [3] C. D. Stanciu, F. Hansteen, A. V. Kimel, A. Kirilyuk, and Th. Rasing, “Observation of an ultrafast nonthermal effect of light on the magnetization in the metallic ferrimagnet GdFeCo.” (Submitted).
- [4] C. D. Stanciu, A. V. Kimel, F. Hansteen, A. Kirilyuk, and Th. Rasing, “Ultrafast spin dynamics across compensation points in ferrimagnetic GdFeCo: The role of angular momentum compensation.” (Submitted).
- [5] F. Hansteen, A. Kimel, A. Kirilyuk, and Th. Rasing, “Nonthermal ultrafast optical control of the magnetization in garnet films,” *Phys. Rev. B*, vol. 73, p. 014421, January 2006.
- [6] D. W. Breiby, F. Hansteen, W. Pisula, O. Bunk, U. Kolb, J. W. Anreassen, K. Müllen, and M. M. Nielsen, “In situ studies of phase transitions in thin discotic films,” *J. Chem. B.*, vol. 109, pp. 22319–22325, October 2005.
- [7] F. Hansteen, A. Kimel, A. Kirilyuk, and Th. Rasing, “Femtosecond photomagnetic switching of spins in ferrimagnetic garnet films,” *Phys. Rev. Lett.*, vol. 95, p. 047402, July 2005.

- [8] F. Hansteen, O. Hunderi, T. H. Johansen, A. Kirilyuk, and Th. Rasing, "Purely magnetization-induced second-harmonic generation in thin garnet films," *Trans. Magn. Soc. Jpn.*, vol. 4, pp. 318–321, 2004.
- [9] F. Hansteen, O. Hunderi, T. H. Johansen, A. Kirilyuk, and Th. Rasing, "Selective surface/interface characterization of thin garnet films by magnetization-induced second-harmonic generation," *Phys. Rev. B*, vol. 70, p. 094408, September 2004.
- [10] F. Hansteen, L. E. Helseth, T. H. Johansen, O. Hunderi, A. Kirilyuk, and T. Rasing, "Optical and magnetooptical properties of bismuth and gallium substituted iron garnet films," *Thin Solid Films*, vol. 455-456C, pp. 429–432, 2004.
- [11] T. Ramsvik, A. Borg, H. J. Venvik, F. Hansteen, M. Kildemo, and T. Worren, "Acetylene chemisorption and decomposition on the Co(11 $\bar{2}$ 0) single crystal surface," *Surf. Sci.*, vol. 499, pp. 183–192, 2002.
- [12] M. Kildemo, F. Hansteen, and O. Hunderi, "Details of below band-gap uniaxial dielectric function of SiC polytypes studied by spectroscopic ellipsometry and polarized light transmission spectroscopy," *J. Appl. Phys.*, vol. 91, pp. 5677–5685, May 2002.
- [13] J. Bremer, L. Seime, O. Hunderi, and F. Hansteen, "Plasmon-mediated scattering of light by ion eroded Ag(110) surfaces," *Phys. Stat. Sol. A.*, vol. 188, no. 4, pp. 1477–1487, 2001.
- [14] J. Bremer, V. Vaicikauskas, O. Hunderi, and F. Hansteen, "Influence of surface plasmons on the faraday effect in bismuth-substituted yttrium iron garnet films," *J. Appl. Phys.*, vol. 89, pp. 6177–6182, June 2001.

Curriculum Vitae

Name:

Fredrik Hansteen

Date of birth:

24 July 1975

Place of birth:

Bergen, Norway

1991–1994	Highschool, Bodin Videregående skole, Bodø, Norway
1994–1999	M.Sc. studies at The Norwegian University of Science and Technology, Trondheim, Norway.
1998	M.Sc. studies as exchange student at the University of Newcastle, Australia.
1999–2000	Laser scientist during compulsory army service at the Norwegian Defence Research Establishment, Kjeller, Norway
2000–2003	Ph.D. studies at The Norwegian University of Science and Technology, Trondheim, Norway.
2003–2005	Ph.D. studies at Radboud University Nijmegen, The Netherlands, in the group of Prof. Th. Rasing.
2005–2006	Postdoctoral researcher at Radboud University Nijmegen, The Netherlands, in the group of Prof. Th. Rasing.